Subcontractor Report

April 2002 • NREL/SR-520-31723

Efficiency and Throughput Advances in Continuous Roll-to-Roll a-Si Alloy PV Manufacturing Technology

Final Subcontract Report
22 June 1998—5 October 2001

T. Ellison
Energy Conversion Devices, Inc.
Troy, Michigan

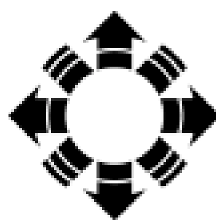

National Renewable Energy Laboratory

1617 Cole Boulevard
Golden, Colorado 80401-3393

NREL is a U.S. Department of Energy Laboratory
Operated by Midwest Research Institute • Battelle • Bechtel

Contract No. DE-AC36-99-GO10337

April 2002 • NREL/ SR-520-31723

Efficiency and Throughput Advances in Continuous Roll-to-Roll a-Si Alloy PV Manufacturing Technology

Final Subcontract Report
22 June 1998—5 October 2001

T. Ellison
Energy Conversion Devices, Inc.
Troy, Michigan

NREL Technical Monitor: R. Mitchell

Prepared under Subcontract No. ZAX-8-17647-09

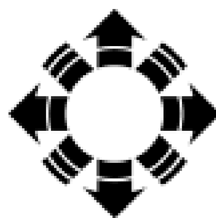

National Renewable Energy Laboratory

1617 Cole Boulevard
Golden, Colorado 80401-3393

NREL is a U.S. Department of Energy Laboratory
Operated by Midwest Research Institute • Battelle • Bechtel

Contract No. DE-AC36-99-GO10337

NOTICE

This report was prepared as an account of work sponsored by an agency of the United States government. Neither the United States government nor any agency thereof, nor any of their employees, makes any warranty, express or implied, or assumes any legal liability or responsibility for the accuracy, completeness, or usefulness of any information, apparatus, product, or process disclosed, or represents that its use would not infringe privately owned rights. Reference herein to any specific commercial product, process, or service by trade name, trademark, manufacturer, or otherwise does not necessarily constitute or imply its endorsement, recommendation, or favoring by the United States government or any agency thereof. The views and opinions of authors expressed herein do not necessarily state or reflect those of the United States government or any agency thereof.

Available electronically at http://www.osti.gov/bridge

Available for a processing fee to U.S. Department of Energy
and its contractors, in paper, from:
U.S. Department of Energy
Office of Scientific and Technical Information
P.O. Box 62
Oak Ridge, TN 37831-0062
phone: 865.576.8401
fax: 865.576.5728
email: reports@adonis.osti.gov

Available for sale to the public, in paper, from:
U.S. Department of Commerce
National Technical Information Service
5285 Port Royal Road
Springfield, VA 22161
phone: 800.553.6847
fax: 703.605.6900
email: orders@ntis.fedworld.gov
online ordering: http://www.ntis.gov/ordering.htm

Printed on paper containing at least 50% wastepaper, including 20% postconsumer waste

TABLE OF CONTENTS

	PAGE
EXECUTIVE SUMMARY	8
Introduction	8
OVERVIEW OF THE FIVE DEVELOPMENT AREAS	9
Area I: Process Control Improvements: Substrate Heating and Temperature Monitoring Systems	9
Area II: In-Line Sensors	10
II.A The PV Capacitive Diagnostic (PVCD)	10
II.B Back Reflector (BR) Scatterometer	11
II.C Thickness Monitors (Reflection Spectrometers)	12
Area III. ZnO Reactive Sputtering	12
Area IV: New Deposition Hardware	13
Area V. New Pinch Valve Technology	14
AREA I: PROCESS CONTROL IMPROVEMENTS: SUBSTRATE HEATING AND TEMPERATURE MONITORING SYSTEMS	16
Summary	16
Introduction – Description of Problem	16
Proposal Outline	17
Installation in the Production Equipment	19
Long Term Operational Experience In The Production Equipment	20
Heater Failure	20
Temperature Uniformity	21
AREA II: DEVELOPMENT OF ONLINE IN-SITU DIAGNOSTIC SYSTEMS	22
Introduction	22
Summary	22
A. PV Capacitive Diagnostic (PVCD).	22
B. Backreflector Scatterometer.	23
C. Reflectometers.	23
AREA II.A. THE PV CAPACITIVE DIAGNOSTIC (PVCD) SYSTEM	24
Introduction	24
PVCD Principles of Operation	25
Introduction	25
PVCD Concept	25
Phase I Work	27
Bench Testing and Proof of Principle	27
Other Bench Measurements	28
Phase II Work	30
Phase III Work	32
3rd Generation PVCD	32
Correlation of Online PVCD Data with Offline QA/QC Measurements	34
Use of the 3rd Generation PVCD for Online QA/QC	36
Present Status and Future Plans	36

TABLE OF CONTENTS (CONT.)

PAGE

AREA II.B. THE BACKREFLECTOR SCATTEROMETER SYSTEM 37
Overview And Summary 37
Motivation and Background 37
Summary of Accomplishments 37
PDA Scatterometer Results 39
Detection of Vacuum Chamber Leak 39
Sensitivity to Process Variations and Correlation with QA/QC Cell Data 40
Use of the Scatterometer for Process Optimization 43
Sensitivity to Changes in Process Parameters 44
Sensitivity to Aluminum Sputtering Targets 44
Sensitivity to Alternative Stainless Steel Substrates 44
Sensitivity to New Aluminum Target Installation 45

AREA II.C. REFLECTOMETER SPECTROMETERS FOR ONLINE THICKNESS MEASURMENT 47
BACKREFLECTOR SPECTROMETER 47
Overview And Summary 47
Motivation and Background 47
Summary of Accomplishments 48
BR Reflectometer Results 48
Design and Installation on the BR Production Machine 48
Initial On-Line Observations 49
Correlation to Process Variations and QA/QC Cell Data 51
Effective Use as a Process Optimization Tool 53
THE AMORPHOUS SILICON SPECTROMETER SYSTEM 55
Overview and Summary 55
Motivation and Background 55
Summary of Accomplishments 55
Developmental Test Stand 56
Hardware and Software 56
Spectrometer Stability and Precision Measurements 56
Positional Sensitivity Measurements 58
5 MW a-Si Machine Spectrometer 59
Hardware and Software 59
Data Analysis 60
Conclusions And Future Plans 62

AREA III. TASKS 3 AND 7 – DEVELOPMENT OF REACTIVE SPUTTERING PROCESS USING INEXPENSIVE ZN METAL TARGETS FOR BACK REFLECTOR PREPARATION 63
Summary 63
Background 64
Objective of Backreflector Studies 65
Phase I of Program 65
Experimental 65
Results of Work Completed During Phase I of the Program 67
Reactive Sputtering Optimization 68

TABLE OF CONTENTS (CONT.)

	PAGE
Phase II of the Program	71
Experimental	71
Hardware Changes to the 5MW line for implementation of the new process	72
Results from Phase II 5MW experiments	73
AREA IV. TASKS 4,8,11 - CATHODE HARDWARE STUDIES FOR A-SI(GE): H I-LAYER DEPOSITIONS	75
Summary	75
Background	76
Objective of Cathode Hardware Studies	78
Experimental	79
Results	82
Static tests in the Single R&D Chamber	82
Testing Similarity to Cathodes Used in Production (5MW Style Cathode)	82
Attempts to Improve Uniformity Using 5 MW Style Cathode	84
Static Testing of 1st Generation New Cathode Design in the Single Chamber	85
Static Testing of 2nd Generation New Cathode Design in the Single Chamber	88
Tests in Pilot Roll-To Roll Machine	89
Static Tests in the Pilot Roll-to-Roll Machine	89
Dynamic Tests in the Pilot Roll-to-Roll Machine	91
Dynamic Tests of 3rd Generation Hardware in the 5MW Line	96
Testing of 3rd Generation Cathode for 25MW Line	97
Modeling for Amorphous Silicon Deposition	97
Introduction	97
Simulation Strategy	98
One-Point Simulations	99
RF-Global Simulation	99
The Boltzmann Code	101
AREA V. PINCH VALVE DEVELOPMENT	115
Summary	115
Overview	115
Commissioning the Pinch Valves	116
Conclusion	118

LIST OF FIGURES

Fig. 1 A comparison of online data from the PVCD with offline QA/QC data over a period of 5 production runs in 2001. [2.4% per division].

Fig. 2 Observed correlation between increased back-reflector scattering and decreased V_{OC}.

Fig. 3 Thickness measurement in the a-Si machine [0.5%/vertical div.; 2 hr/horizontal div.]. Experiments during this run resulted in thickness changes.

Fig. 4 Deposition profiles of the new cathode taken 3 months apart, compared with previous cathode design [blue curve] (Note: offset vertical scale).

Fig. 5 Data from United Solar illustrating the effect of the new Pinch Valve technology on operations. The pinch valve was put into routine operation at about run #1315, and was tested intermittently for about the previous 50 runs.

Fig. I.1 Photograph showing the IR lamps coated with deposition material.

Fig. I.2 Photograph of the proposed NiChrome heating element**.**

Fig. I.3 Sketch of experimental housing.

Fig. I.4 Ribbon-type heaters installed in the production machine.

Fig. I.5 Ribbon heater assembly detail.

Fig. I.6 Photograph of failed heater assembly.

Fig. I.7 Web temperature profiles for the various heater configurations. The top thick line shows the temperature uniformity after implementation of the new technique.

Fig. II.A-1 Functional schematic of the PVCD.

Fig. II.A-2 Schematic PVCD waveforms.

Fig. II.A-3 Photograph of the PVCD bench-test system. The oscilloscope is displaying the waveforms of the laser pulse (the step function) and the output of the PVCD. Notice the similarity between the stored traces on the oscilloscope and the waveforms in Fig II.A-2.

Fig. II.A-4 Photograph of oscilloscope traces showing the response of a PV cell (measured with a contacting probe), and the response of the PVCD to a pulsed light. The light source was pulsed on for 5 ms, between the 2nd and 3rd vertical graticule.

Fig. II.A-5 PVCD waveforms and fitted curves resulting for a $(nip)_1n_2$, $(nip)_1n_2i_2$ and $(nip)_1n_2i_2p_2$ cells.

Fig. II.A-6 Data displayed linear-linear and log-log showing the proportionality of the initial PVCD derivative and the light pulse amplitude.

Fig. II.A-7 PVCD data showing that PVCD signal amplitude is proportional to the logarithm of the light intensity.

Fig. II.A-8 Recorded amplitude of the PVCD system during a two week period in November 99. The time periods when the amplitude is low correspond to when the machine is being turned around.

Fig. II.A-9 Graph showing the stability the 2nd generation PVCD V_{OC} measurement (1% full scale/div). Whereas the noise level is on the level of 0.2% peak-peak, there is a 3% drift caused by temperature changes in the web and electronics.

Fig. II.A-12 Raw data from PVCD and V_{OC} measurements from the United Solar offline QA/QC system. The vertical scale corresponds to 0.5% per major division.

Fig. II.A-10 Rendering of the 3rd Generation PVCD installed in the 5 MW production a-Si production machine.

Fig. II.A-11 Photograph of the 3rd Generation PVCD being modified for bench-testing.

Fig. II.A-13 Online PVCD data compared with offline QA/QC measurements of PV characteristics for runs 5 MW 1287 – 1291.

Fig. II.A-14 Voltage vs. time on triple junction a-Si solar cells with, and without, ITO.

LIST OF FIGURES (CONT.)

Fig. II.A-15 Measured voltage "decay time" vs. PV cell temperature.
Fig. II.A-16 Raw online PVCD data and offline P_{MAX} data for 5 MW runs 1207 – 1212.
Fig. II.B-1 Drawing of the PDA scatterometer presently installed on United Solar's BR production machine.
Fig. II.B-2 Plot showing the effect of a vacuum chamber leak on the scatter signal.
Fig. II.B-3 Plot of integrated scatter during BR deposition experiments.
Fig. II.B-4 Plot of cell Voc and series resistance vs. integrated scatter.
Fig. II.B-5 Plot of integrated scatter during a BR deposition experiment.
Fig. II.B-6 Plots of integrated scatter versus off-line cell I-V parameters.
Fig. II.B-7 Plot of three BR runs showing the effect of flow controller.
Fig. II.B-8 Plot showing the effect of alternative aluminum BR on the scatter signal.
Fig. II.B-9 Plot showing the effect of alternative stainless steel substrate on integrated scatter signal.
Fig. II.B-10 Plot showing the effect of new Al target installation on integrated scatter signal.
Fig. II.C-1 Schematic of the on-line BR and ITO reflectometers
Fig. II.C-2 Plot of typical standard ZnO layer reflectance
Fig. III-C-3 Trend plot of standard ZnO reflectance minimum and maximum during a production run.
Fig. II.C-4 Plot of ZnO reflectance value at the maximum during a production run. (Note the start of the run occurs near 45 meters.)
Fig. II.C-5 Plot showing the change in the reflection minimum where ZnO thickness was reduced.
Fig. II.C-6 Plot showing dependence of ZnO reflectance on cathode power.
Fig. II.C-7 Plot of 5 reflection curves recorded over a 25-minute period during BR process transition.
Fig. II.C-8 Plot comparing standard ZnO and reactive-ZnO reflection curves.
Fig. II.C-9 ***LabView*** control panel for selecting extrema to track.
Fig. II.C-10 Reflectance spectrum from triple layered a-Si sample.
Fig. II.C-11 Spectrum extrema tracking precision over time.
Fig. II.C-12 Extrema wavelengths versus sample position.
Fig. II.C-13 Spectrometer fibers mounted in a-Si Take-Up chamber.
Fig. II.C-14 Change in interference pattern from loss of plasma rf.
Fig. II.C-15 Resulting wavelength (i.e. thickness) change.
Fig. II.C-16 Resulting wavelength (i.e. thickness) change.
Fig. III-1 United Solar's roll-to-roll backreflector machine. This machine is also part of United Solar's decommissioned 2 MW plant and will be used for the bulk of Task 3, and for part of Task 7.
Fig. III-2 Dependence of J_{sc} for a-SiGe:H cells on oxygen flow. (Ts=substrate temperature)
Fig. IV-1 Variation of Ge content and deposition rate across cathode.
Fig. IV-2 Double-junction roll-to-roll plasma-CVD processor, previously used as United Solar's production machine. This machine was used as an experimental machine for much of the work proposed in Tasks 8 and 11.
Fig. IV-3 Single chamber system used for cathode development.
Fig. IV-4 a-Si:H single-junction cell structure.
Fig. IV-5 Thickness profiles for films made at different applied rf powers.
Fig. IV-6 Orientation of film thickness measurements.
Fig. IV-7 Variation of deposition uniformity over length of cathode as a function of deposition rate.

LIST OF FIGURES (CONT.)

Fig. IV-8 Uniformity across width of web (cathode) from deposits made using different gas flows from outside cathode and gas manifold hardware.
Fig. IV-9 Deposition rate profiles across new cathode at different deposition rates.
Fig. IV-10 Plot of fill factor versus short circuit current for cells made using the new and 5 MW style cathodes.
Fig. IV-11 Plot of efficiency versus short circuit current for cells made using the new and 5 MW style cathodes.
Fig. IV-12 Deposition rate vs. position along the cathode in the 2nd generation system.
Fig. IV-13 Deposition rate vs. position along the cathode in the 3rd generation system.
Fig. IV-14 Light-soaked P_{max} values for a-SiGe:H cells with red light V_{oc} near 0.6V as a function of I-layer thickness.
Fig. IV-15 Deposition rate profiles across cathode length for 3rd generation hardware installed in 5MW production machine.
Fig. IV-16 Electron Impact Cross Sections (cm^2): a. H_2 momentum transfer.
Fig. IV-17 Electron Impact Cross Sections (cm^2): Lowest threshold H optical excitation.
Fig. IV-18 Electron Impact Cross Sections (cm^2): SiH_4 optical excitation.
Fig. IV-19 Electron Impact Cross Sections (cm^2): H_2 Ionization.
Fig. IV-20 Electron Impact Cross Sections (cm^2): Lowest threshold H_2 vibrational excitation.
Fig. IV-21 Electron Impact Cross Sections (cm^2): Lowest threshold SiH_4 vibrational excitation.
Fig. IV-22 Electron Impact Cross Sections (cm^2): Dissociative attachment from the v=1 and v=2 vibrational states of H_2.
Fig. IV-23 Modeled RF Reactor Subchamber Design.
Fig. IV-24 Electron Energy Distribution functions at various times after turn-on: $1.75x10^{-8}$.
Fig. IV-25 Electron energy distribution functions at various times after turn-on:$1.34x10^{-6}$.
Fig. IV-26 Electron energy distribution functions at various times after turn-on: $9.77x10^{-6}$.
Fig. IV-27 Electron energy distribution functions at various times after turn-on: $9.90x10^{-3}$s.
Fig. IV-28 Evolution of Neutral Species (cm^{-3}):H_2, SiH_4, H, SiH_3, SiH_6.
Fig. IV-29 Evolution of Neutral Species (cm^{-3}): H_2, H_2(v=1), H_2(v=2).
Fig. IV-30 Evolution of Neutral Species (cm-3): Si_2H_5, SiH_2, SiH, Si.
Fig. IV-31 Evolution of Neutral Species (cm^{-3}): Si_2H_4, Si_2H_2, Si_2H, Si_2.
Fig. IV-32 Evolution of Neutral Species (cm^{-3}): Si_2H_3, Si_3H_8, Si_3H_5, Si_3H_4.
Fig. IV-33 Evolution of Positive Ions (cm^3):SiH_3^+, SiH_2^+, SiH^+, $Si_2H_0^+$, $Si_2H_5^+$.
Fig. IV-34 Evolution of Positive Ions (cm^{-3}): Si_2H_4+, $Si_2H_3^+$, $Si_2H_2^+$, Si_2H^+, $Si_3H_7^+$.
Fig. IV-35 Evolution of Positive Ions (cm^{-3}):$Si_3H_6^+$, $Si_3H_5^+$, Si_3H_4, H_3^+, H_2^+, H^+.
Fig. IV-36 Evolution of Negative Ions (cm^{-3}): H^+, SiH_3^+, $Si_2H_5^+$, $Si_3H_7^+$.
Fig. IV-37 Evolution of Positive and Negative Ions and Electrons (cm^{-3}): total positive ions, total negative ions, electrons.
Fig. IV-38 Evolution of Average Electron Energy (ev).
Fig. IV-39 Measured thickness of amorphous silicon deposition (nm) in reactor.
Fig. V.1 Amorphous silicon machine turn around time. The Pinch Valves were put into routine operation at about Run 1315.

LIST OF TABLES

Table II.C-1 Comparison of Standard and Reactive ZnO deposition QA/QC cell I-V data.
Table III-1 Data for 44.5 cm^2 Modules Made with Different Backreflectors.
Table III-2 Comparison of Data for a-Si:H Cells Co-Deposited on Al/Zn Backreflectors. Cell Measurements Completed Using AM1.5 Light (R_s is the series resistance).
Table III-3 Data for Cells Prepared Using the Different Backreflectors After Different Exposure Environments and Exposure Times.
Table III-4 Data for a-SiGe:H Cells Prepared with Backreflectors Made Using Reactive Sputtering Technique Under a Variety of Deposition Conditions.
Table III-5 Data for a-SiGe:H Cells Whose Backreflectors were Made Using Targets with Different Al Contents.
Table III-6 Data for a-SiGe:H Cells Whose Backreflectors were Made with the Reactive Sputtering Process Using Zn Metal Targets and the Standard Process Using ZnO Targets.
Table III-7 Data for 44.5 cm^2 Modules Made with Different Backreflectors.
Table III-8 Data for 0.25cm^2 Cells with Reactive and Standard BR processes.
Table III-9 Data for 45cm^2 Modules PVMAT Deliverables for Reactive Sputtered ZnO (5-15-00).
Table III-10 Data for QA/QC Coupons Made Using Different ZnO Processes.
Table IV-1 Comparison of performance of cells produced in the 2nd and 3rd generation hardware to cells produced in the 5 MW style hardware.
Table IV-2 Data for a-Si:H cells made at different applied powers but similar i-layer deposition rates.
Table IV-3 Data for a-Si:H Cells Made Using the New and the 5 MW Style Cathodes.
Table IV-4 Comparison of performance of cells produced in the 1st and 2nd generation cathode hardware.
Table IV-5 Comparison of performance of cells produced in the 2nd and 3rd generation hardware to cells produced in the 5 MW style hardware.
Table IV-6 Data for cells made during 100m long deposition run in the pilot roll-to-roll machine using ~3 Å/s i-layer deposition rate.
Table IV-7 Data for 0.25cm^2 Cells Made Using 3rd Generation Cathode and Different Gas Mixtures.
Table IV-8 Data for Cells Made Using 3rd Generation Cathode and Different Gas Mixtures.
Table IV-9 Data for Cells Made Using 3rd Generation Cathode and Different Total Gas Flows.
Table IV-10 Data for Cells With Back Reflectors Made Using 3rd.

EXECUTIVE SUMMARY

Introduction

Energy Conversion Devices, Inc. (ECD) and its American joint venture, United Solar Systems Corp. (United Solar), have developed and commercialized a roll-to-roll triple junction amorphous silicon alloy PV manufacturing technology. This low material cost, roll-to-roll production technology has the economies of scale needed to meet the cost goals necessary for widespread use of PV.

ECD has developed and built 6 generations of a-Si production equipment, including the present 5 MW United Solar manufacturing plant in Troy, Michigan. ECD is now designing and building a new 25 MW facility, also in Michigan.

United Solar holds the world's record for amorphous silicon PV conversion efficiency, and manufactures and markets a wide range of PV products including flexible portable modules, power modules, and innovative Building Integrated PV (BIPV) shingle and metal roofing modules that take advantage of this lightweight, rugged and flexible PV technology. All of United Solar's power and BIPV products are U.L. approved and carry a 10-year warrantee.

In this PVMaT 5A subcontract, ECD and United Solar are addressing issues to reduce the cost and improve the manufacturing technology for the ECD/United Solar PV module manufacturing process. ECD and United Solar identified five technology development areas that would reduce the module manufacturing cost in the present 5 MW production facility, and also be applicable to future larger scale manufacturing facilities. These 5 development areas are:

- I. Tasks 1, 5: Improved substrate heating and monitoring systems
- II. Tasks 2, 6, 9: Development of new on-line diagnostic systems
  - II.A PV Capacitive Diagnostic (PVCD)
  - II.B Back Reflector Scatterometer
  - II.C Thickness Monitors
- III. Tasks 3, 7: Development of new backreflector deposition technology
- IV. Tasks 4, 8, 11: Development of improved rf PECVD reactor cathode
- V. Tasks 8A, 10A: Development of new pinch valve technology

The work in all these areas has been remarkably successful:

1. We have met all of our program goals and milestones.
2. All the technology developed has been either implemented or tested on the present 5 MW United Solar production equipment with tangible benefits.
3. All of these technologies are being incorporating into the design of the new United Solar 25 MW production equipment now being fabricated by ECD.

In the following section we provide a brief overview of these tasks. In subsequent sections these tasks are discussed individually in more detail. Each of these subsequent sections begins with a 1 – 2 page summary of the problem, work performed, and accomplishments.

OVERVIEW OF THE FIVE DEVELOPMENT AREAS

Area I: Process Control Improvements: Substrate Heating and Temperature Monitoring Systems

ECD has traditionally used quartz envelope infrared (IR) lamps to heat the substrate in the amorphous silicon deposition machines. These lamps, because they run hot, would get coated along with the substrate. The accumulation of deposition material on these lamps, in combination with the temperature cycling, resulted in flaking of deposition material and in physical stresses that would break the lamps' quartz envelopes. Breakage during runs was minimized by routine changing of the lamps every couple of months.

In this program we proposed replacing these infrared heaters with low-temperature, long-lasting NiChrome (Nickel Chrome alloy) resistance heaters. A system was designed, tested, optimized and proven in United Solar's 2 MW pilot production line. An improved system was then designed, fabricated, and installed in the 5 MW production equipment. The original set of heaters installed in the system, after an initial modification to improve the ceramic insulators, are still functioning after about 800 production runs. Although there have been a few isolated failures, and the heater elements have lost some of their malleability, we still have not determined their lifetime. They appear to be "self-cleaning", and are extremely robust.

The substrate heating system is no longer a significant source of machine downtime due to lamp failure. The new lamps have also eliminated a major maintenance item: the IR lamps had to be replaced about every nine weeks; the material cost was about 24 k$, and this maintenance operation took about 20 hrs. We estimate that these new lamps, which have a lifetime of at least a couple of years, reduce our manufacturing cost by about 0.06 $/W.

In the process of optimizing these new heaters, we have also developed a technique to decrease the crossweb temperature non-uniformity by more than an order of magnitude. This new substrate heating system is now serving as a model for the heating and temperature monitoring systems being designed for the new 25 MW production equipment that ECD is building for United Solar. All the program goals and milestones for this task have been met, most ahead of schedule.

Area II: In-Line Sensors

Online diagnostic systems can improve the manufacturing process in several ways: they can immediately alert operators to changes in the output of a process, increase the process optimization feedback rate by orders of magnitude compared to off-line QA/QC, and provide the potential for expert system process control and optimization. These capabilities can also reduce the time needed for commissioning new equipment.

In this program we have focussed our work on 3 diagnostic systems: a backreflector scatterometer, reflection spectrometers (thickness monitors) for the ZnO, a-Si, and ITO layers, and a PV Capacitive Diagnostic (PVCD) system for the a-Si machine.

II.A The PV Capacitive Diagnostic (PVCD)

The PV Capacitive Diagnostic (PVCD) is a is a non-contacting device that measures the electrical characteristics of the PV device in the take-up chamber of the a-Si machine before deposition of the ITO layer. In Phase I we bench tested a device and showed that, with a pulsed light source, we can accurately measure the PV voltage vs. time using a non-contacting system. In Phase II, we installed a second generation system in the take-up chamber of the 5 MW a-Si production machine and demonstrated that we can easily detect missing layers and track the device V_{oc}.

Online testing of the 2nd generation system made clear technical issues not obvious on the bench, including the effects of ionized gas, and the need for temperature and position stability. These issues were addressed in the 3rd generation system. The design stability of this 3rd generation device is 0.1%, and target stability 0.01%. The 3rd generation PVCD has been installed in the 5 MW a-Si production machine since November 2000. The measured noise is about 0.2% rms, similar to the noise in offline QA/QC data [see Fig. 1], and 0.1% using a 4-point moving average.

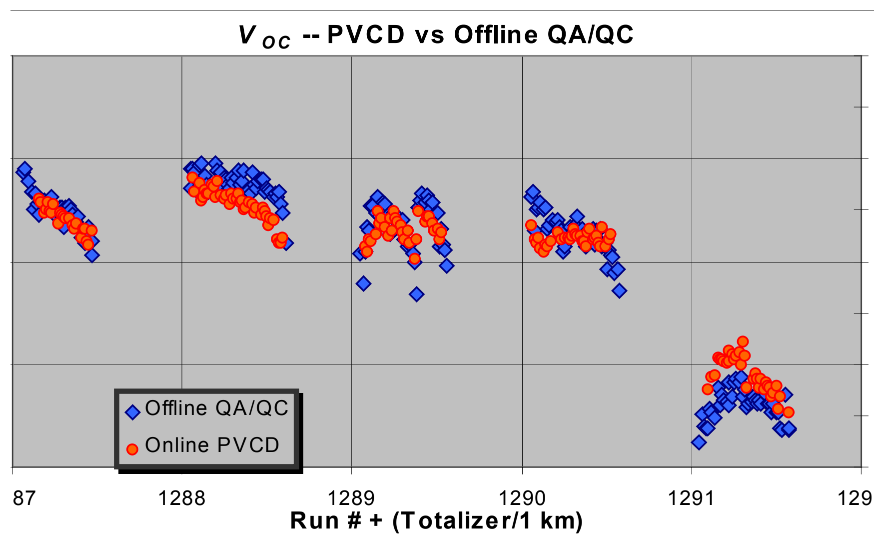

Fig. 1. A comparison of online data from the PVCD with offline QA/QC data over a period of 5 production runs in 2001. [2.4% per division].

The PVCD has demonstrated the ability to detect non-conforming material, and is able to measure most PV cell characteristics. It is in routine use as an online QA/QC instrument, and has detected several problems before the material reached offline QA/QC. We have not yet successfully used it for real-time optimization.

II.B Back Reflector (BR) Scatterometer:

The first version fabricated and bench tested in Phase I used a fixed laser and a photo-detector on a moving arm to measure both the specular and diffuse reflectance. This device allowed us to determine which angles are of interest and to begin to correlate reflectivity vs. angle measurements with device quality. In Phase II a second generation system was then built for installation in the 5 MW BR machine. This device has no moving parts, and has all the electronics mounted external to the vacuum system. It uses a fixed laser, a photo-diode for measuring the specular component and a photo-diode array to measure the diffuse reflectance. The second generation scatterometer has been installed in the 5 MW production backreflector machine since May 2001.

The scatterometer has been proven to be a useful online QA/QC device:

- changes in online measurements from the scatterometer correlate with changes in offline PV device characteristics (*e.g.* V_{OC} *and* R_S) [see Fig. 2];
- the device is sensitive to changes in process parameters (e.g. sputtering power and target changes);
- and it has demonstrated the ability to detect non-conforming material (e.g. material produced when there was a small vacuum leak).

An updated version is planned for the new 25 MW production equipment.

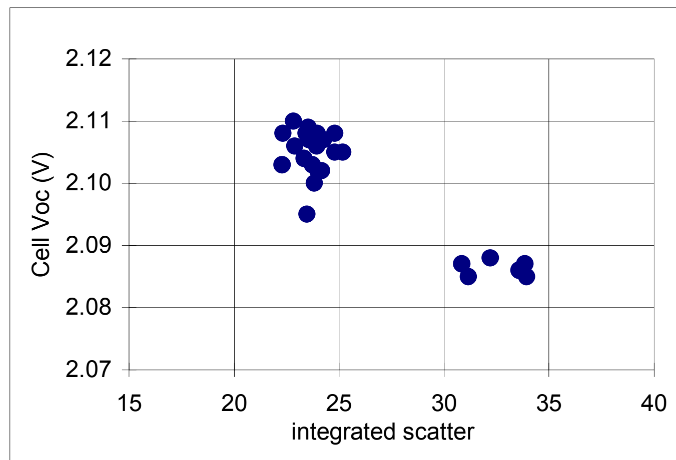

Fig. 2. Observed correlation between increased back-reflector scattering and decreased V_{OC}.

II.C Thickness Monitors (Reflection Spectrometers)

Thickness Monitoring Reflection Spectrometers are being developed to measure the thickness of the ZnO, a-Si, and ITO layers. In Phase II we installed the thickness monitor in the production BR machine. The monitor is now in use for BR development work. This new diagnostic system immediately proved its value by allowing us to quickly and precisely adjust the ZnO thickness in the production machine when first using the new reactive sputtering technique developed in Tasks 3 and 7. In the a-Si machine, without extensive operation, we observe a precision of about 0.1% [see Fig. 3].

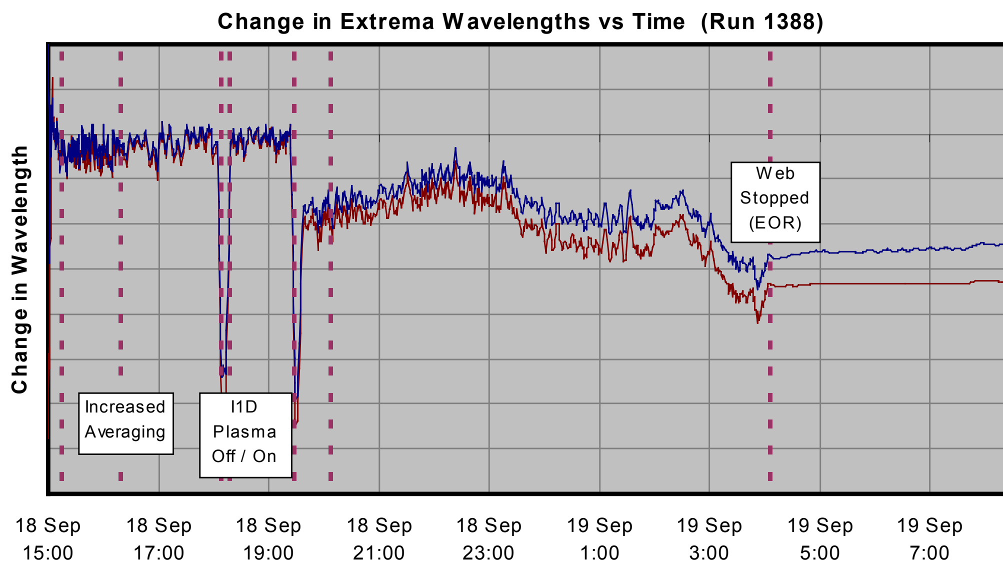

Fig. 3. Thickness measurement in the a-Si machine [0.5%/vertical div.; 2 hr/horizontal div.]. Experiments during this run resulted in thickness changes.

Devices of this type are planned for the new 25 MW production machines where we also plan to eventually include a closed loop thickness control system. This will move us away from specifying process parameters (e.g. rf power, gas flow), to instead specifying device properties (e.g. thicknesses of various layers).

Area III. ZnO Reactive Sputtering

United Solar deposits the ZnO layer in its backreflector using magnetron sputtering and ceramic ZnO targets. The manufacturing cost for this layer could be reduced by about an order of magnitude by replacing the ceramic ZnO targets and reactively sputtering the ZnO layer from Zn metal targets. In the Phase I portion of this program we optimized this reactive sputtering process in United Solar's 2 MW pilot backreflector machine. In the Phase II portion of this program we tested and performed initial optimization of this process in United Solar's 5 MW production machine. This backreflector was then processed through the a-Si and ITO roll-to-roll production machines and through QA/QC. The QA/QC analysis showed that the PV material produced with the reactive sputtering process has the same efficiency as cells produced

on the standard production backreflector. We estimate that this process will reduce the manufacturing cost by about 0.03$/W.

This sputtering process developed in this program will be used for the new 25 MW production equipment.

Area IV: New Deposition Hardware

Although the production machines use the same recipes as our research reactors, the production machines have never been able to produce PV material with the same efficiencies as can consistently be produced in the research reactors. We believe that there are some fundamental differences in between the large area PECVD reactors used for production and the smaller reactors used in research. In addition, there are problems observed with large area reactors that are not observed in small area reactors, such as changes in the uniformity of deposition thickness with deposition rate. This change in deposition thickness uniformity with deposition rate is observed to a large degree in the present large area production cathodes, and severely limits the dynamic range over with parameters can be varied in optimization studies.

In this Task we are developing and testing new cathode and gas distribution concepts for large area cathodes that will more closely reproduce the results obtained in the small area research reactors and that will provide a higher degree of deposition thickness uniformity over a wider range of deposition rates. In the Phase II portion of this program the 2nd and 3rd generations of cathode hardware were installed and tested in the pilot roll-to-roll machine. With both sets of hardware, the goal of ± 5% thickness uniformity across 80% of the cathode areas was achieved at deposition rates between 2.9 and 4.3 Å/s rates. These rates are 1.5 - 2.2 times the rates used in production. Using the 3rd generation hardware, efficiencies that are 4% greater than those obtained in the production machine have been achieved for a-Si single-junction cells demonstrating an improvement in I-layer quality.

In Phase III (December 2000), we installed a prototype version of the new cathode geometry in United Solar's 5 MW production equipment, where it has worked splendidly. Based upon these successful tests, this new geometry has become the standard cathode for the new 25 MW production equipment. With this cathode we have demonstrated substantially increased deposition uniformity [see Fig. 4], and have also developed recipes that reduce the cost of gases.

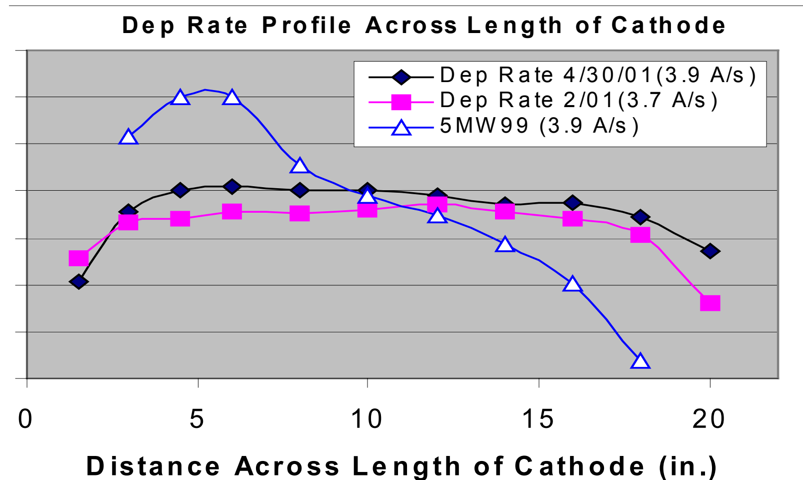

Fig. 4. Deposition profiles of the new cathode taken 3 months apart, compared with previous cathode design [blue curve] (Note: offset vertical scale).

Area V. New Pinch Valve Technology

United Solar production managers estimated that the turnaround time for the a-Si production machine could be reduced by about 1.5 hr if the cool down and heat up procedures could be eliminated. In this program we proposed designing, fabricating and testing a new "pinch valve" technology that would allow the production crews to change rolls of substrate in the take-up and pay-off chambers without needing to cool down, vent, pump down, and re-heat all the process chambers. Since the a-Si machine is presently the rate-limiting machine, the resulting increase in throughput for this machine would directly lead to a corresponding throughput increase for the entire production plant. We expected an increase of about 6%, as well as other benefits resulting from reduced thermal cycling of components and not venting the deposition portion of the machine to air.

The milestone for testing this device in United Solar's 5 MW production machine, scheduled for early in the Phase III portion of the program, was achieved in Phase II. In Phase III we identified problems with the design that were not apparent in offline testing, retrofitted the device, and carried out the additional machine modifications and changes to the interlock, pumping, and sequence of operations necessary to implement this device into machine operations.

The pinch valve system was put into routine operation in the summer of 2001. The use of this device has increased the machine throughput by about 6 to 10%, as shown in Fig. 5. These devices were used as models to develop pinch valves for the new United Solar 25 MW production equipment being fabricated by ECD.

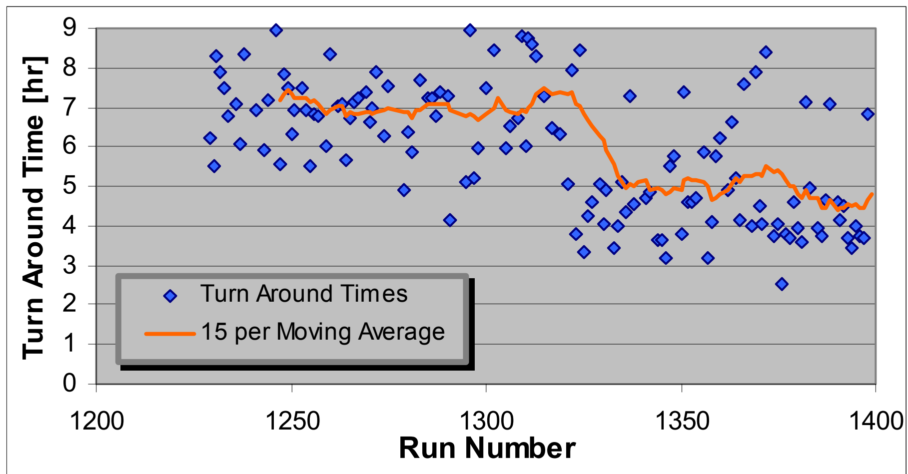

Fig. 5. Data from United Solar illustrating the effect of the new Pinch Valve technology on operations. The pinch valve was put into routine operation at about run #1315, and was tested intermittently for about the previous 50 runs.

AREA I: PROCESS CONTROL IMPROVEMENTS: SUBSTRATE HEATING AND TEMPERATURE MONITORING SYSTEMS

Summary

This portion of the PVMat program has been very success. We accomplished all goals as originally proposed, ahead of our original schedule:

- We have designed and built a new, improved substrate heater using flat-ribbon-shaped elements.
- We have completed the pilot and production machine installation of the new substrate heaters.
- We have demonstrated precise temperature control while using the new substrate heaters.
- We have demonstrated suitability of the new substrate heaters in the production machine.
- We have, in addition, demonstrated remarkable improvements in cross-web temperature uniformity.
- Finally, these new heaters, besides improving the operation of the present production equipment, are being adapted for use in the new United Solar 25 MW production equipment being designed and fabricated by ECD.

Introduction – Description of Problem

The multi-section amorphous silicon alloy deposition machine consists of a pay-off chamber section, nine process chamber sections for deposition of the triple (graded) junction, triple bandgap solar cells, and a take-up section. This machine is a continuous roll-to-roll rf plasma-enhanced CVD processing system, in which mixtures of feedstock gases are decomposed at a pressure of approximately 1 torr in a series of plasma chambers. In each chamber, the substrate is maintained at various temperatures of a few hundred °C, and exposed to various gas mixtures.

In the past, the substrate temperature was maintained by exposing the web to the radiation of infrared lamps. As shown in Fig. I.1, these lamps, because they run hot, would get coated with deposition along with the substrate.

Fig. I.1. Photograph showing the IR lamps coated with deposition material.

The accumulation of deposition material on the IR lamps, in combination with the unavoidable temperature cycles, eventually resulted in severe flaking and in physical stresses large enough to break the lamp quartz envelopes. Even though the deposition takes place on the underside of the substrate, the growing film is not protected from physical damage from the flakes and from the glass debris. Breakage of the quartz IR lamps leads to downtime, and expense.

Proposal Outline

We proposed to replace the quartz heaters in the roll-to-roll deposition machine with low-temperature, long-lasting NiChrome (a Nickel Chrome alloy) resistance heaters. These heaters operate at lower, more stable, temperatures. More importantly, they were thought to require little, if any, maintenance. They further offer considerable freedom in their design. We proposed to design, prototype, test, and retrofit the deposition machines with a new substrate heating system using flat ribbon-shaped elements held in place over the web with ceramic insulators, in a basic “flat sheet” configuration shown in Fig. I.2.

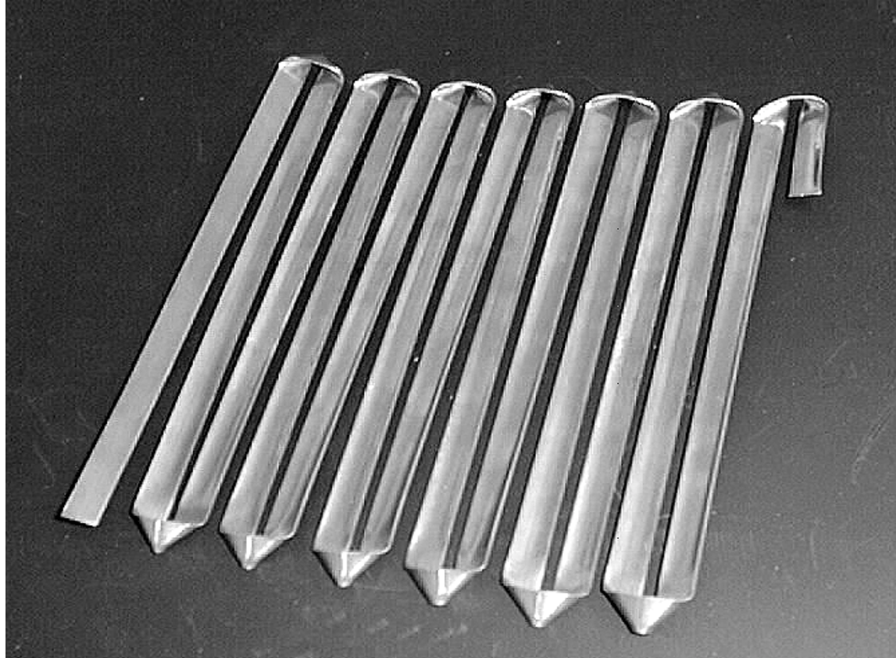

Fig. I.2. Photograph of the proposed NiChrome heating element.

These ribbon heaters were initially installed in the pilot machine, using a housing that allowed the shape of the "flat sheet" to be adjusted to a large degree, as shown in Fig. I.3. The idea behind the adjustment was to be able to compensate for the generally higher temperatures at the centerline of the web.

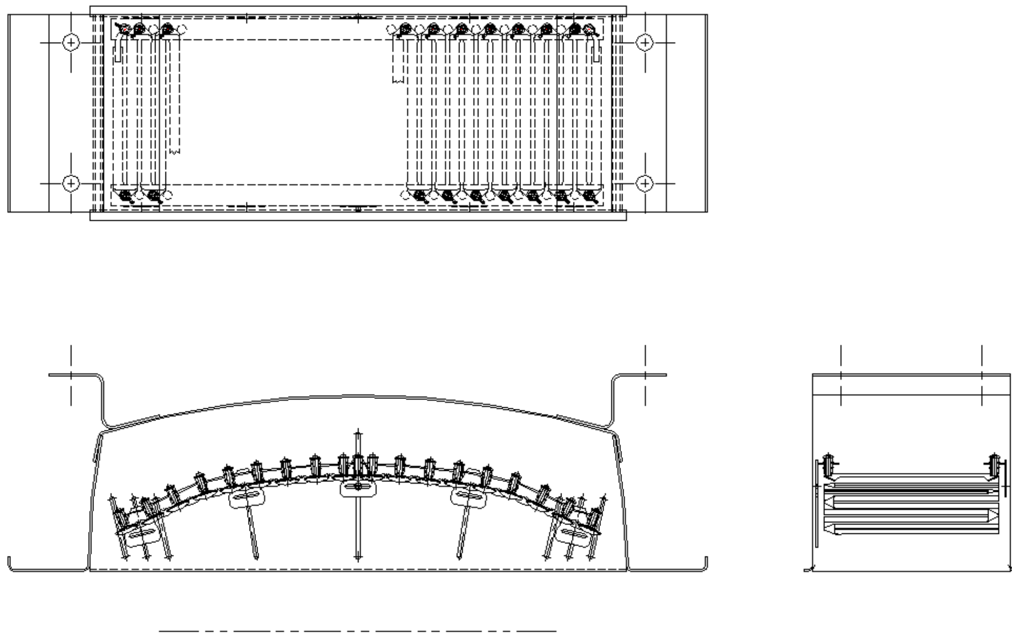

Fig. I.3. Sketch of experimental housing

Installation in the Production Equipment

Testing in the pilot machine quickly demonstrated that the reliability of these new ribbon heaters was vastly superior to that of the infrared lamps. Consequently, well ahead of schedule, we decided to fabricate and install ribbon-type heaters in the production machine. Figs. I.4 and I.5 show their installation.

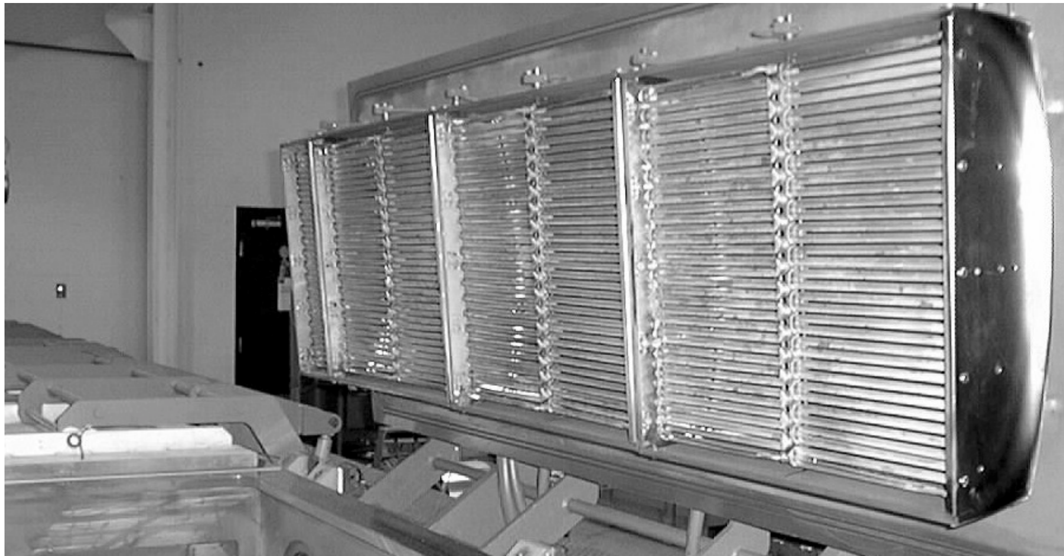

Fig. I.4. Ribbon-type heaters installed in the production machine.

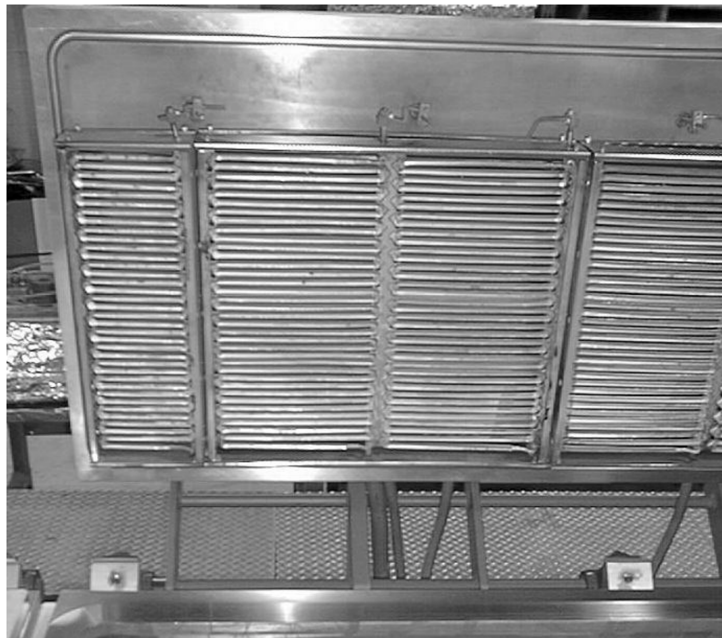

Fig. I.5. Ribbon heater assembly detail.

Long Term Operational Experience In The Production Equipment

As of September 2001, the ribbon heaters had contributed to about 900 production runs and continue their splendid operations. In contrast, about 120 of the old style IR lamps would have had to be replaced about 12 times, with a total material cost of 120 k$. The cost savings resulting from runs not terminated due to lamp breakage, and scheduled downtime for lamp maintenance are at least that great. We have not yet observed any sign of degradation, though there have been a few isolated failures, the first occurring after several hundred runs.

Fig. I.6. Photograph of failed heater assembly.

Heater Failure

One of the new ribbon heater assemblies failed in late 1999. A photograph of the failed heater is shown in Fig. I.6. A post-mortem analysis has shown that a ceramic isolation post has broken, and that the ribbon had shorted to the grounded chassis. It is not clear, however, whether the failing post caused the ribbon to short, or whether excessive local heat from a defective ribbon element overheated the post. Further analysis has revealed that the heater elements have become brittle, probably due to chemical reactions with the feedstock gases used in the deposition reactor. The ribbon heaters show no other sign of visual, electrical or operational degradation. No process contamination has been observed with these heaters.

Temperature Uniformity

We have recently developed a technique that dramatically increases the cross-web temperature uniformity. Fig. I.7 shows the measured cross-web temperature before and after implementation of this new technique.

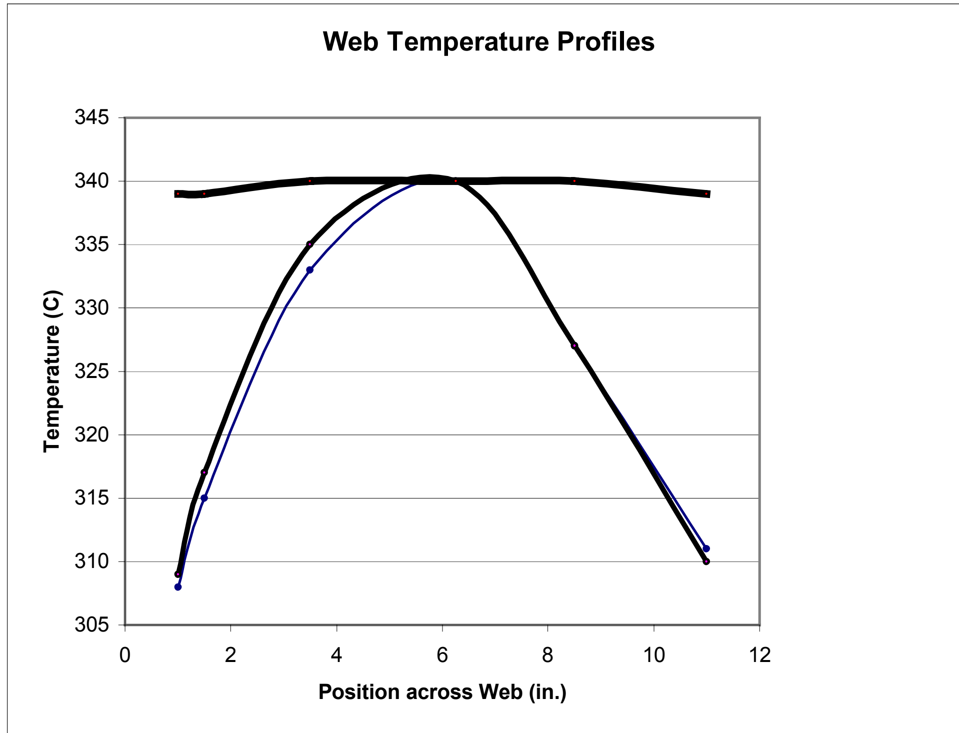

Fig. I.7. Web temperature profiles for the various heater configurations. The top thick line shows the temperature uniformity after implementation of the new technique.

AREA II: DEVELOPMENT OF ONLINE IN-SITU DIAGNOSTIC SYSTEMS

Introduction

United Solar manufactures its PV material using ≈ ½ mile long substrates that are processed sequentially through a series of roll-to-roll deposition machines: the backreflector (BR), amorphous silicon (a-Si), and top conductive oxide (ITO) machines. The QA/QC process takes place after the long substrate has been slabbed, etched, and passivated following deposition in final roll-to-roll machine. This is a highly efficient manufacturing process, but can be improved with online diagnostic systems:

1. Online diagnostics will immediately notify operators of any significant problems, consequently reducing the probability that equipment malfunctions or operator errors go unrecognized until the later QA/QC process.
2. The feedback rate for continually optimizing the machines using incremental variations in the standard processing conditions could potentially be increased by several orders of magnitude to less than 1/hr from the present 1/few days.
3. The operators would be able to identify and track fluctuations in process parameters that lead to variations in the quality of cells produced, consequently increasing the average conversion efficiency of the PV material.

We already have highly-instrumented and automated production machines with hardware and software feedback systems. These machines are operated open-loop, however, in the sense that sensors principally monitor process parameters (e.g. temperature, rf power, pressure, etc.) rather than characteristics of the deposited coatings (e.g. V_{OC}, efficiency, J_{SC}, diffusivity of the backreflector, conductance and thickness of the ZnO, etc.). In this PVMaT program ECD and United Solar have begun the development and implementation of online, real-time diagnostic systems to measure the characteristics of material produced in the 3 roll-to-roll deposition machines. At a minimum these devices have the potential of alerting operators to production problems in a timely fashion; the potential also exists for employing these system for online optimization of material during the production process.

Summary

Three diagnostic systems were developed under development in this *program:*

A. *PV Capacitive Diagnostic (PVCD)*. The first generation system, developed in Phase I, was used for bench testing. Using a pulsed laser light source, this system demonstrated that non-contacting measurements of a PV cell voltage as a function time accurately reproduced the cell voltage measurements derived from a contacting measurement system. In Phase II we fabricated a second-generation device and mounted it in the take-up chamber of the 5 MW a-Si deposition production machine where it demonstrated the ability to detect changes in the device quality on-line. Experience with this system enabled us to identify a number of system improvements that were incorporated into the third generation system. This third generation system was specified, designed, and assembled for bench testing in August 2000. It was installed in the production machine in November 2000, and has since proved its value as an online QA/QC device. This system has demonstrated a

single-point rms noise level of 0.2%, which can be improved with averaging – a signal to noise level on the same order as offline QA/QC measurements.

Additional areas of improvement have been identified during the last 10 months of operation. A major retrofit was undertaken in September 2001, and is scheduled for completion in early October 2001. We expect that this retrofitted device will serve as a model that can be replicated and installed in the new 25 MW equipment. With this device we shall be able to gather several months of data to create a good baseline for use in expediting the commissioning of the 25 MW equipment.

B. *Backreflector Scatterometer*. This device characterizes the texture of the BR material. This device has evolved considerably in sophistication: the first generation device used for bench testing consisted of a single photo-diode mounted on a moving mechanical arm to measure reflectance as a function of angle. The second generation device contains no moving parts and was designed to be installed in the production BR machine with all electrical components mounted outside the vacuum system. This second-generation system uses a fixed laser, a single photo-diode to measure the specular reflectance, and a photodiode array to measure the diffuse reflectance over a wide range of angles, and was installed in the 5 MW production backreflector machine in May 2001.

   The scatterometer has proven to be a useful online QA/QC device: changes in online measurements from the scatterometer correlate with changes in offline PV device characteristics (e.g. V_{OC} and R_S); the device is sensitive to changes in process parameters (e.g. sputtering power and target changes), and it has demonstrated the ability to detect non-conforming material (e.g. material produced when there was a small vacuum leak). An updated version is planned for the new 25 MW production equipment. This instrument has recently been used to provide feedback in optimizing the BR machine for a new working point. The offline QA/QC data is not yet available to confirm the success of this set of studies.

C. *Reflectometers.* This device measures the thickness of the films deposited in the roll-to-roll machines. We first began working on a reflectometer for the Backreflector Machine. This device was installed in the production BR machine ahead of schedule in November 1999 and is now in operation. The reflectometer immediately proved its value by enabling the rapid optimization of reactively sputtered ZnO films in the production machine – Task 7 in this PVMat Program.

   In the Phase III portion of this program we also installed a system in the a-Si production roll-to-roll machine. Initial testing has shown that this device has the potential for being a valuable instrument for both online QA/QC, and for expediting the commissioning of new production equipment.

In the following three sections we briefly review the work we have accomplished for each of these 3 diagnostic systems.

AREA II.A. THE PV CAPACITIVE DIAGNOSTIC (PVCD) SYSTEM

Introduction

The PV Capacitive Diagnostic (PVCD) is a non-contacting device used to measure the PV characteristics (e.g. V_{OC}, J_{SC}/C) in-situ during production. Since it is non-contacting, it can be used to measure cells even before a top transparent conductive oxide has been deposited, and can measure component cells in the triple-junction device as they are being fabricated.

In Phase I, a prototype system was built and bench tested. Measurements using ITO coated cells (which allowed simultaneous measurements with contacting probes) proved that the non-contacting PVCD measurement faithfully reproduced measurements using more conventional contacting measurements. This early experiment was a “proof of concept” for the PVCD. As discussed below, there are effects that can take place in the presence of plasmas, or with cells without a top ITO coating, the can give rise to erroneous measurements. In addition, considerable instrumentation development was required for this concept to become a reliable online QA/QC instrument. (This development is continuing today, with the PVCD having undergone a reconfiguration in Sept 01, with re-installation on 05 Oct 01). Further bench testing demonstrated that besides being able to measure open circuit voltage, the PVCD could measure parameters proportional to the short circuit current as well as other cell properties.

In the Phase II portion of the program, a second generation system was designed, fabricated, bench tested, and installed in the Take-Up chamber of the United Solar 5 MW a-Si production machine. A first generation Data Acquisition System (DAQ) and operator interface was also developed. Online data from this system demonstrated that the PVCD could measure changes in the material quality online. This testing pointed out effects not apparent from bench testing, such as an “enhancement” effect due to ionized residual gas and the importance of stabilizing the temperature of the electronics and the PV material.

A third generation device was then developed, bench tested and installed in the 5 MW production equipment in November 2000, and has been in routine use as an online QA/QC device. The system has operated extremely reliably, with a single point rms noise of 0.2% which can be improved with averaging, and has correctly identified production problems. If offline, the operators complain about “flying blind”. It has not yet proven reliable for optimization, however, due to an effect related to the residual charge on the web. Consequently, the system was removed from operation in September 2001 and re-worked to alleviate this effect. It is scheduled for re-installation the week of on October 8 in a configuration that will emulate what we have planned for the new 25 MW equipment.

In the following sections we review the PVCD’s principle of operation, and the improvements that have been incorporated into the device during the 3 phases of this program.

PVCD Principles of Operation

Introduction

One can envision many methods for non-contacting measurement of a PV device open circuit voltage when exposed to a certain spectral flux of light, $\Phi(\lambda)$. Most are techniques that linearly transform the constant device voltage into a time-varying electric field that can be sensed by an a.c.-coupled electrode.

The generating voltmeter (GVM) is an example of such a device. GVMs have been in use for about 100 years; they typically have a precision and stability of about 0.01%, limited by the mechanical and temperature stability of the device. GVM's are still in use today for non-contacting measurement of the multi-MV terminal potentials in Pelletron particle accelerators. The GVM uses a rotating (fan-like) grounded electrode to chop the electric field; the resulting a.c. electric field is intercepted by another stationary fan-like electrode (grid) positioned between the rotating grounded grid and a grounded surface. This technique for measuring open circuit voltage was demonstrated at ECD in 1994.

A GVM, or Kelvin probe, in conjunction with a CW light source, is an attractive possibility for *in-situ* $V_{OC}(\Phi)$ measurements. PV devices, however, offer another possibility: the a.c. electric field can be created by pulsing a light source, and consequently, the PV voltage and electric field. There are a number of technical pros and cons to each approach. The latter approach, however, offers the possibility of obtaining more information about the PV cell characteristics: one can also observe the rate that the cell capacity is charged when the light source is pulsed on, and the rate that the cell capacity discharges when the light source is turned off. We have taken this approach in developing the PVCD at ECD.

The electrostatic measurement techniques described here are similar to those used to measure the properties of particle beam in accelerators. In particle accelerators, one might be looking at beam currents as low as 10's of nA, with signal amplitudes of 100's of nV. In that regime one must use super-heterodyne detection techniques and design the electronics to keep the electronic noise to within a few dB of the kTR resistor noise at the input of the system. In this application, we have the luxury of working with volt-level signals where there are no significant fundamental signal-to-noise constraints.

PVCD Concept

The PVCD is conceptually very simple, consisting only of a pulsed light source, two transparent conductive grids, and a high input impedance amplifier (see Fig. II.A-1), or a low input impedance integrating amplifier. The light source, pulsed with a step waveform for simplicity, is directed through the two grids onto the surface of the PV material. The grid closest to the PV material is the pick-up grid and is connected to a high ($\approx$ 1 TΩ) input impedance amplifier; the other grid is grounded. The PV cell voltage then begins to increase as the PV cell current charges up the PV cell capacity (see Fig. II.A-2). When the light pulse is turned off, the PV cell then discharges.

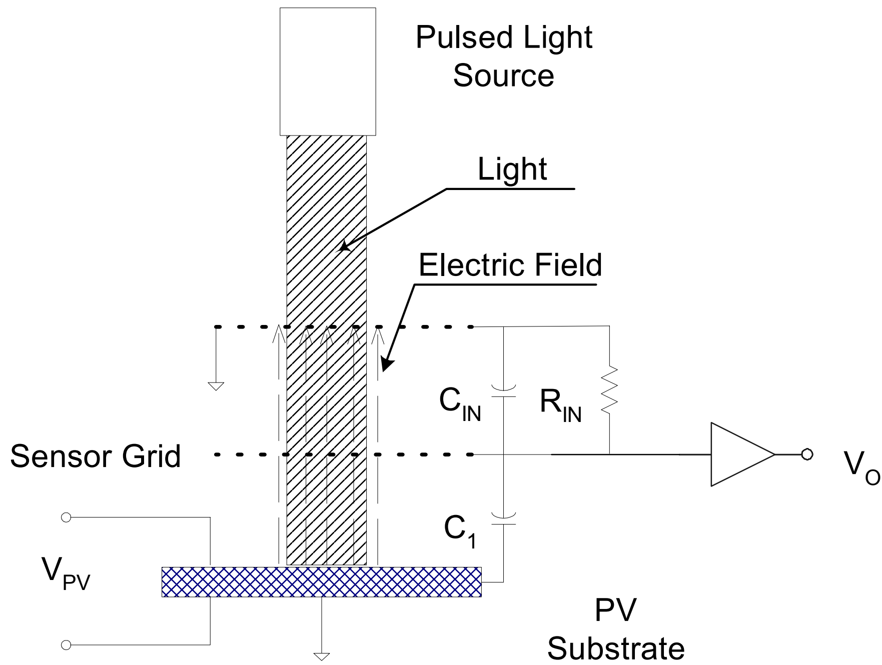

Fig. II.A-1. Functional schematic of the PVCD.

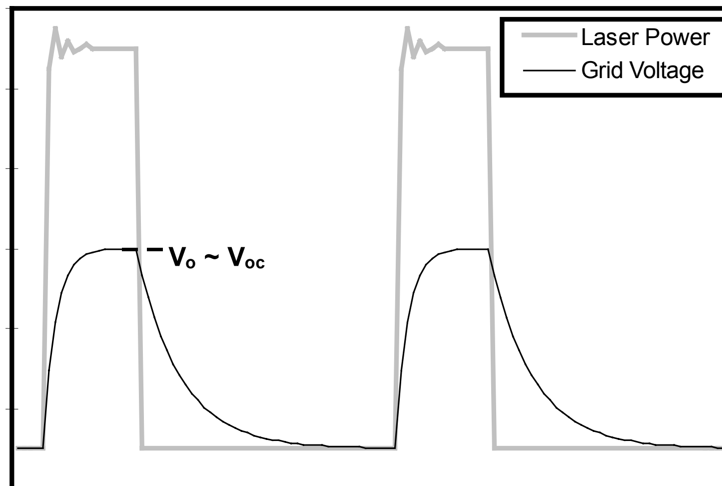

Fig. II.A-2. Schematic PVCD waveforms.

In the regime where $C_{IN}R_{IN}$ (see Fig. II.A-1) is much greater than the time width of the light pulse, the PVCD sensor grid voltage, V_O, is proportional to the PV voltage:

$$V_O(t) = V_{PV}(t) \cdot \frac{C_1}{C_1 + C_{IN}} \approx V_{PV}(t) \cdot \frac{C_1}{C_{IN}}$$

where $V_{PV}(t)$ is the PV device voltage as a function of time, t; C_1 is the capacity between the PV device and the sensor grid; and C_{IN} is the capacity of the sensor grid to ground. C_{IN} is typically much greater than C_1 due to the additional input capacity of the amplifier and the capacity of the cable connecting the amplifier to the sensor grid. By instead using a low input impedance integrating amplifier, the effect of the input capacitance can be removed, replaced by the controlled capacitance in the feedback of the amplifier.

Phase I Work

In Phase I we built and tested a prototype for bench testing, convincingly demonstrated a proof-of-principle test, and designed a second generation system for testing in the production machine.

Bench Testing and Proof of Principle

Fig. II.A-3 shows a picture of the bench-test developed in Phase I.

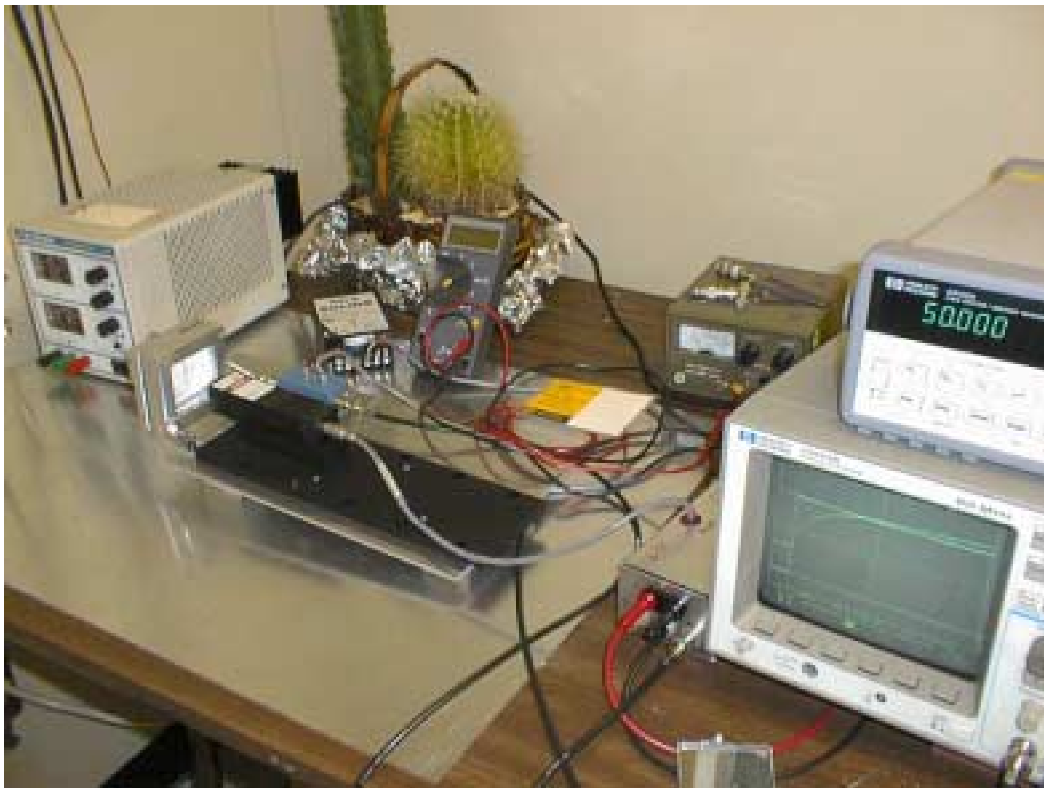

Fig. II.A-3. Photograph of the PVCD bench-test system. The oscilloscope is displaying the waveforms of the laser pulse (the step function) and the output of the PVCD. Notice the similarity between the stored traces on the oscilloscope and the waveforms in Fig. II.A-2.

As a proof-of-principle we measured an ITO-covered PV cell simultaneously with the PVCD and with a contacting system. This simultaneous measurement is shown in Fig. II.A-4. The agreement is perfect when a small correction is made for the time constant of the PVCD amplifier.

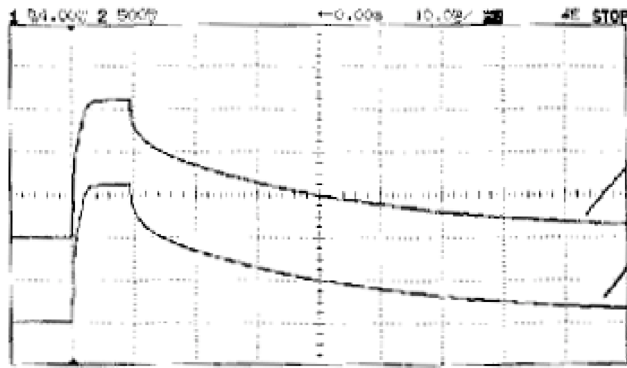

Fig. II.A-4. Photograph of oscilloscope traces showing the response of a PV cell (measured with a contacting probe), and the response of the PVCD to a pulsed light. The light source was pulsed on for 5 ms, between the 2nd and 3rd vertical graticule.

Other Bench Measurements

Other bench measurements showed that the PVCD device could clearly see the change in PV cell characteristics as each layer was deposited onto the substrate. Fig. II.A-5 shows the output of the PVCD as three successive layers were added.

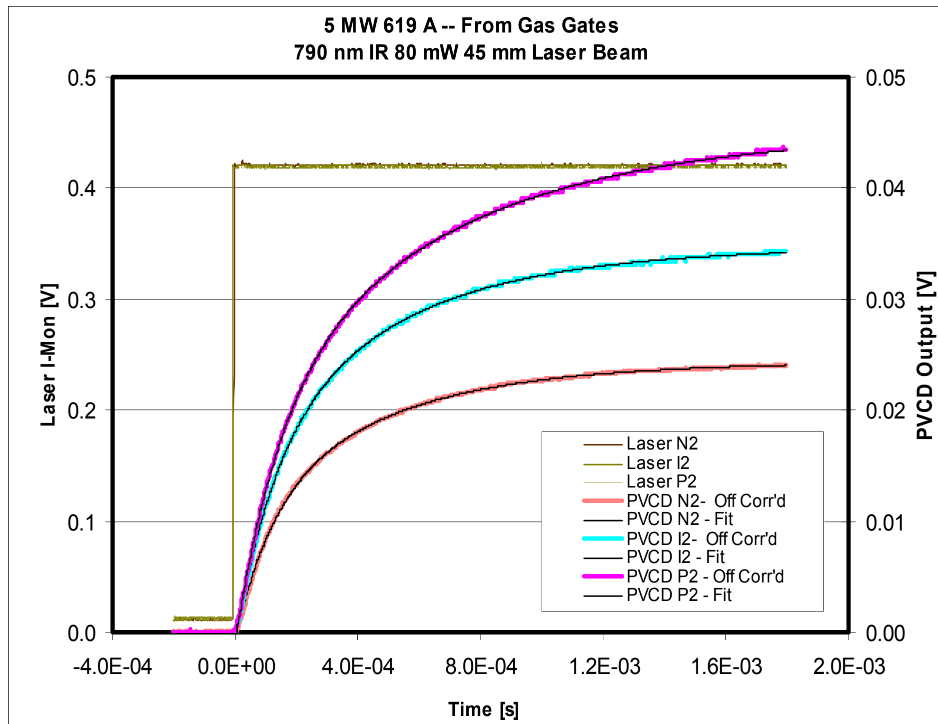

Fig. II.A-5. PVCD waveforms and fitted curves resulting for a $(nip)_1n_2$, $(nip)_1n_2i_2$ and $(nip)_1n_2i_2p_2$ cells.

Other bench measurements showed that the PVCD could provide data on the cell short circuit current properties, and could measure the cell junction I-V characteristics, as shown in Figs. II.A-6 and II.A-7.

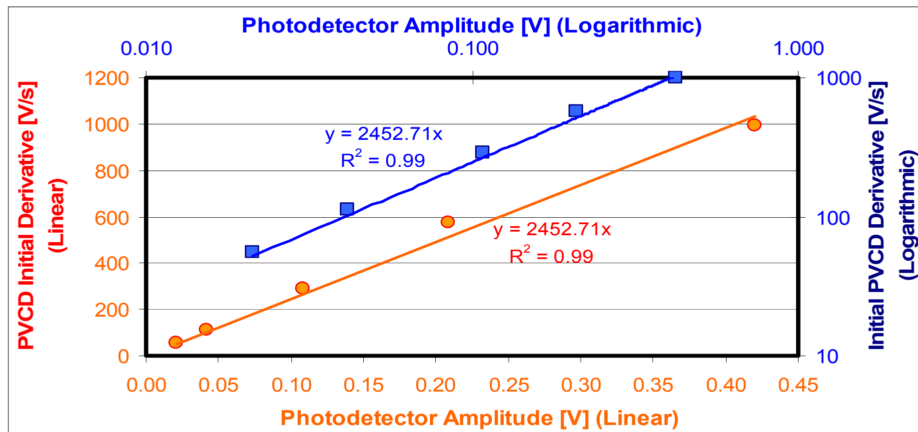

Fig. II.A-6. Data displayed linear-linear and log-log showing the proportionality of the initial PVCD waveform wavelength derivative and the light pulse amplitude.

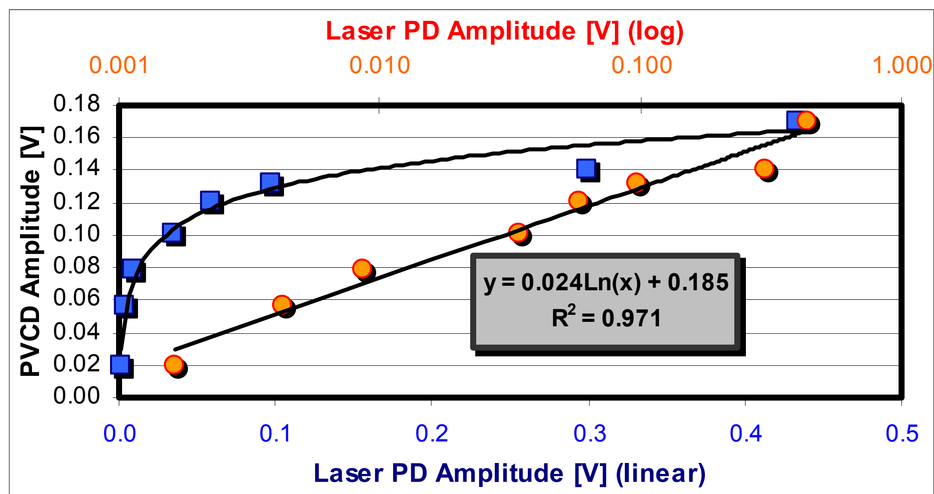

Fig. II.A-7. PVCD data showing that PVCD signal amplitude is proportional to the logarithm of the light intensity.

Phase II Work

In Phase II we developed a 2nd generation PVCD and computer data acquisition system and installed it in the Take-Up chamber of the 5 MW production machine. With this system we demonstrated that we could detect changes in the PV material characteristics online. We became aware of two important effects not observed in bench testing: the effect of ionized gas, and the temperature coefficient of the PV material and electronics.

The data acquisition system allowed us to log the amplitude of the PVCD and compare it with offline data. Figure II.A-8 displays a graph of the recorded PVCD amplitude vs. time for about a 2 week period in Nov 99. The most significant feature of these data is the decrease in signal amplitude over the period of a run – a feature that is not found in the offline QA/QC measurements. This was principally due to the temperature of the web slowly increasing during the run in the take-up chamber, and the negative voltage coefficient of the PV material.

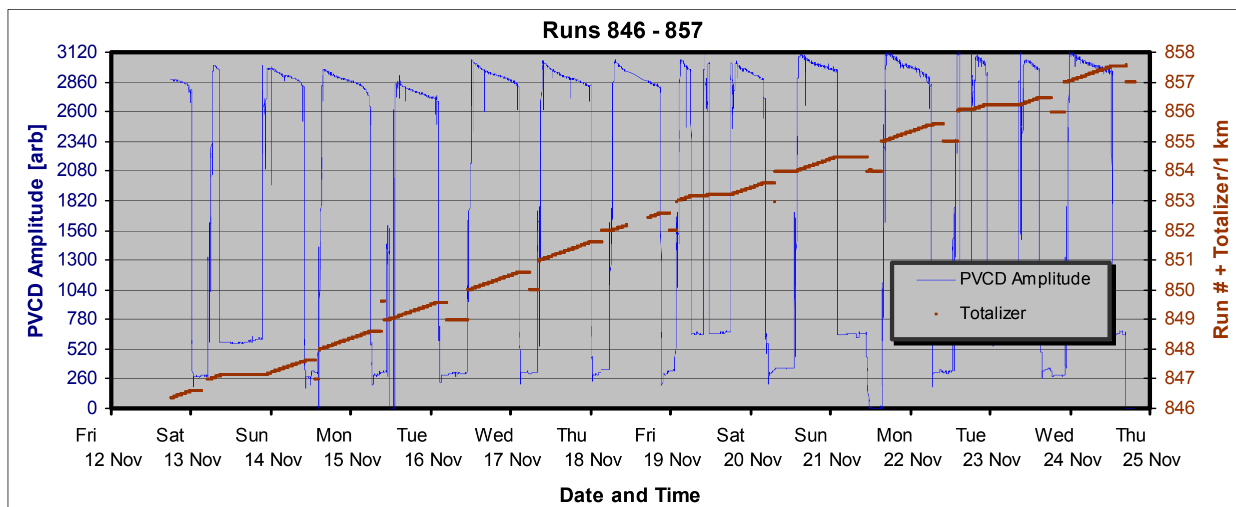

Fig II.A-8. Recorded amplitude of the PVCD system during a two week period in November 99. The time periods when the amplitude is low corresponds to times when the machine is being turned around.

As shown in Fig. II.A-9, although we observed a large change in the PVCD output due to this temperature variation, the noise from the instrument was very low, typically 0.2% rms, without averaging.

We also observed an effect due to ionized gas in the chamber. We were able to eliminate this effect by changing the position of the PVCD device.

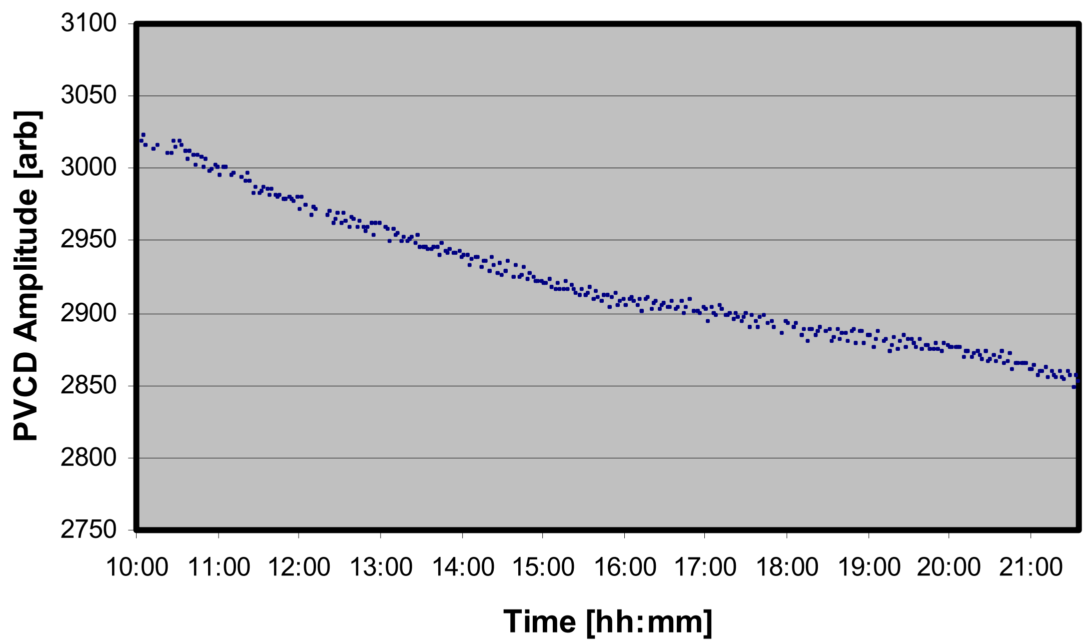

Fig. II.A-9. Graph showing the stability the 2nd generation PVCD V_{OC} measurement (1% full scale/div). Whereas the noise level is on the level of 0.2% peak-peak, there is a 3% drift caused by temperature changes in the web and electronics.

Phase III Work

3rd Generation PVCD

In Phase III we designed, fabricated, and installed a 3rd generation PVCD device in the 5 MW production machine. Some of the principle improvements in this device included:

- Integrated temperature stabilization of the PVCD, electronics, and PV material being tested.
- Improved variable-wavelength higher-intensity and higher-stability light source.
- A higher (16 bit vs. 11 bit) precision data acquisition system.

An early version of the 3rd generation device is shown in Figs. II.A-10 and 11 on the following page. The significant performance increase in this 3rd generation device is apparent by comparing its raw data with offline QA/QC data [see Fig II.A-12] and data from the 2nd generation device [see Fig II.A-8]. In Fig II.A-12 one can see the high degree of correlation between the PVCD raw data and offline V_{OC} measurements.

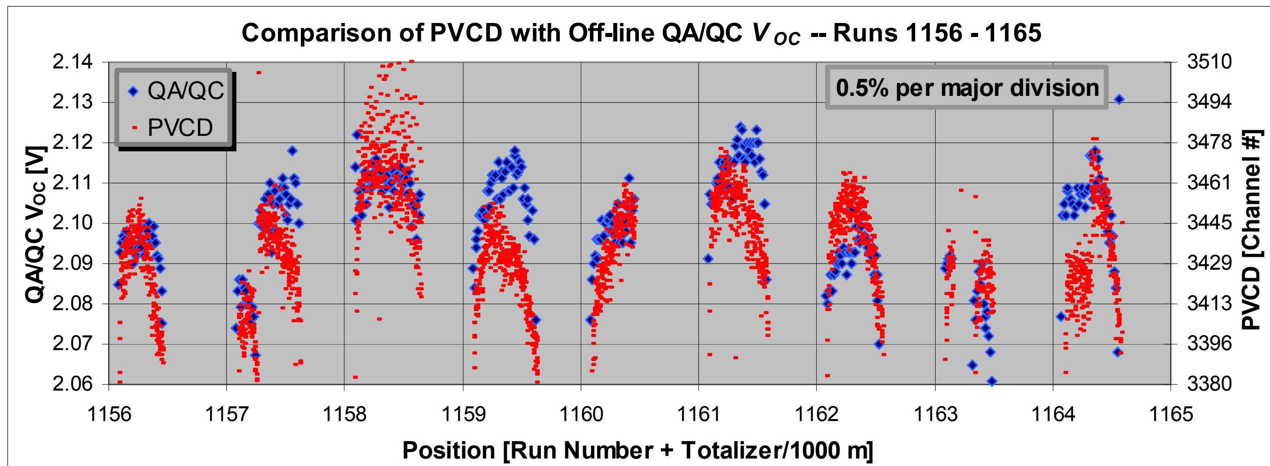

Fig. II.A-12. Raw data from PVCD and V_{OC} measurements from the United Solar offline QA/QC system. The vertical scale corresponds to 0.5% per major division.

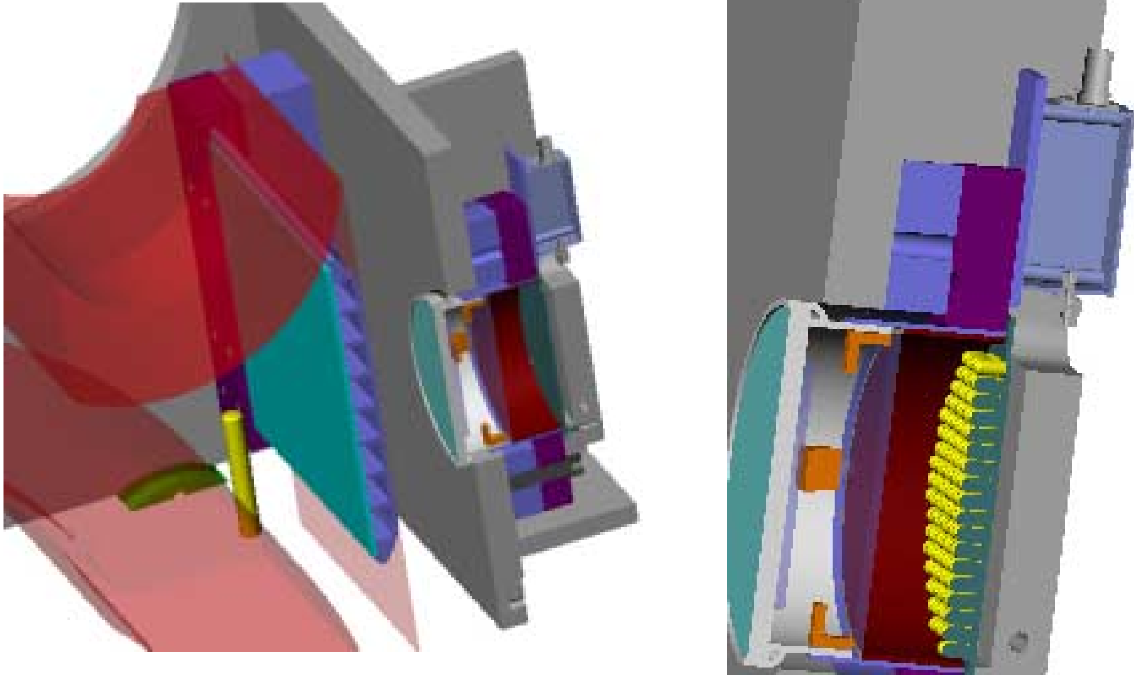

Fig. II.A-10. Rendering of the 3rd Generation PVCD installed in the 5 MW production a-Si production machine.

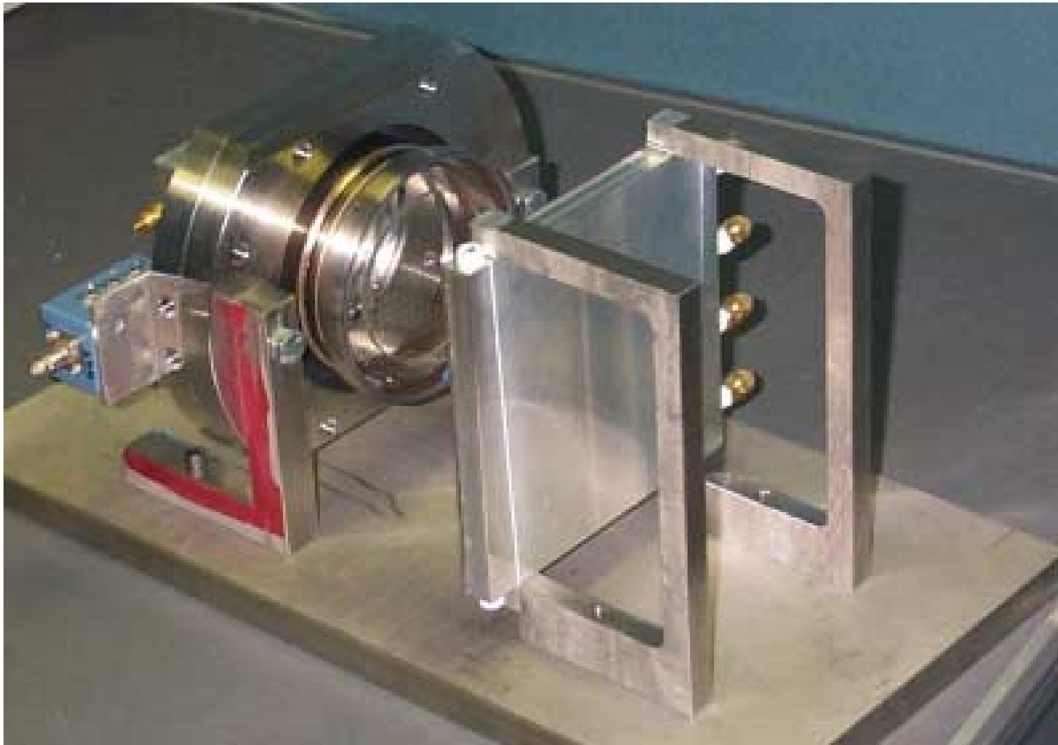

Fig. II.A-11. Photograph of the 3rd Generation PVCD being modified for bench-testing.

Correlation of Online PVCD Data with Offline QA/QC Measurements

The correlation between the raw online and offline data shown in Fig II.A-12 is very impressive. While this is generally the case, there have also been a few cases where we have found poor agreement. There are two principle reasons for this:

1. The data in above figure are for a single property of a PVCD waveform made at a single light spectrum and amplitude. As such, this measurement is related to more than a single measured offline QA/QC property (e.g. V_{OC}, P_{MAX}, J_{SC}, etc.). Consequently, a number of different online PVCD measurements must also be made in order to precisely connect online PVCD data with offline data.
2. The PVCD is a.c. coupled to the PV device being measured. Changes in process parameters can change the small initial voltage on the PV material – a property that the PVCD device was not originally capable of measuring.

In order to address the first concern and better connect the PVCD measurements with offline QA/QC we developed a new ***LabView*** data acquisition system (DAQ). This system makes a series of measurements using different light wavelengths and intensities, and measures different properties of the PVCD waveform. Once this was instituted, we found much better agreement between online and offline data, and could connect the online data with various offline QA/QC measurements as shown in Fig. II.A-13.

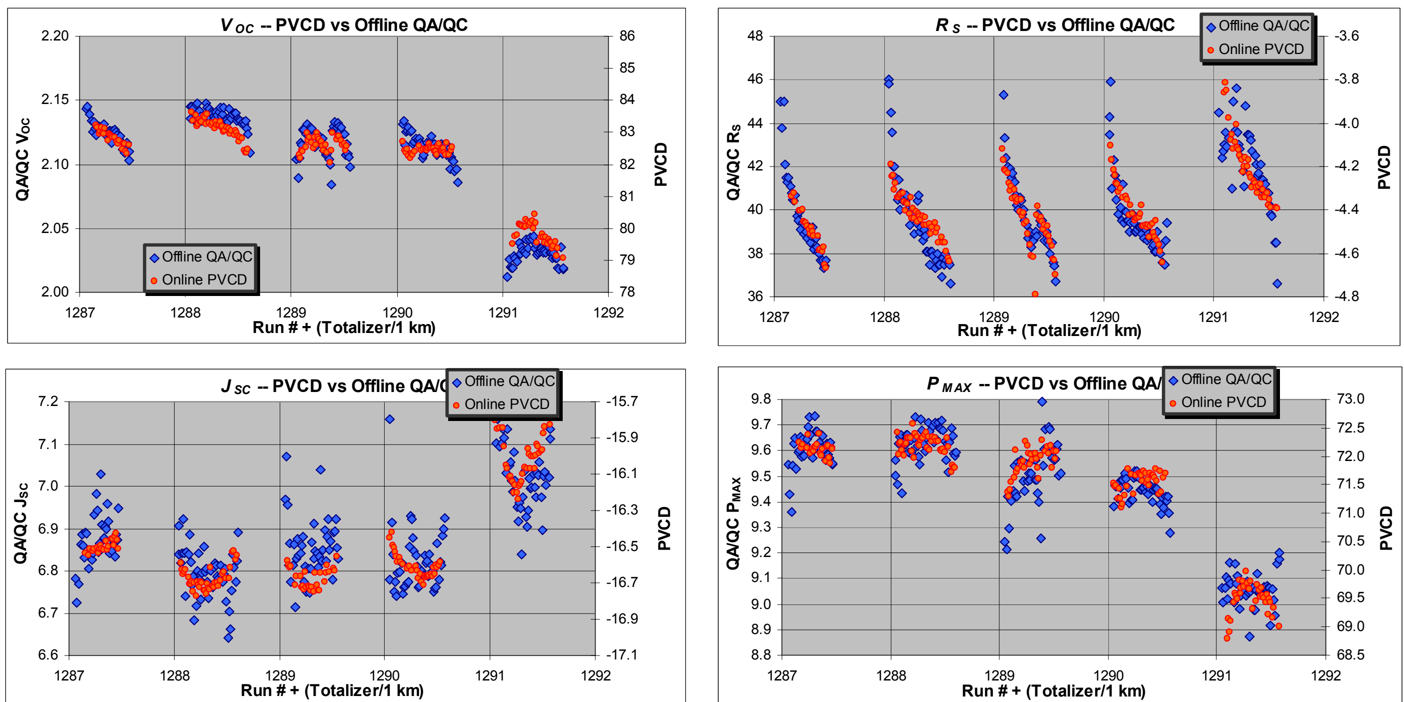

Fig. II.A-13. Online PVCD data compared with offline QA/QC measurements of PV characteristics for runs 5 MW 1287 – 1291.

We still, however, did not always have perfect agreement. The remaining discrepancy appears to be due to changes in the residual voltage on the PV material prior to measurement by the PVCD device. As shown in Fig. II.A-14, it takes on the order of 10^5 s (about 24 hours) for the PV cells to discharge if they do not have an ITO coating. This voltage "decay time", as shown in Fig. II.A-15 is also very dependent on the cell temperature, so changes in the processing parameters, or changes to the temperature of objects surrounding the web as a run progresses, can also change this "offset voltage". As this report is being written, we are re-installing the PVCD device with modifications to both eliminate and measure any offset voltage. After these changes are instituted, we expect to be able to consistently make online measurements of cell properties that will rival the consistency, precision, and accuracy of offline QA/QC measurements.

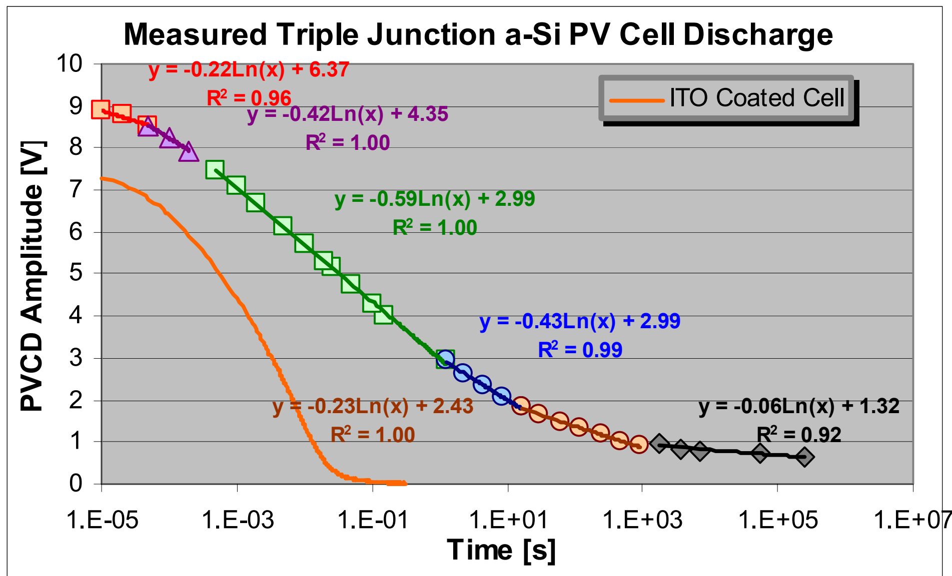

Fig. II.A-14. Voltage vs. time on triple junction a-Si solar cells with, and without, ITO.

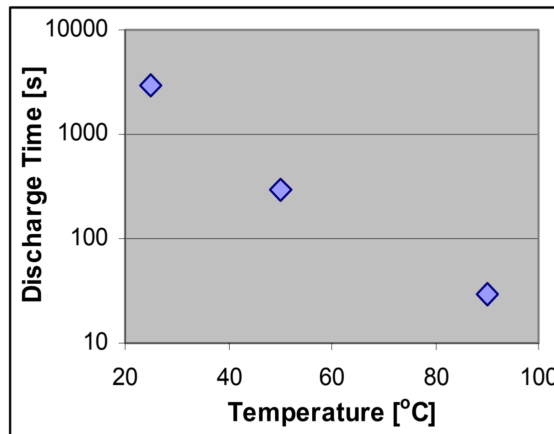

Fig. II.A-15. Measured voltage "decay time" vs. PV cell temperature.

Use of the 3rd Generation PVCD for Online QA/QC

Despite that fact that the 3rd generation PVCD device is still being developed, it has proven very valuable as on online QA/QC device. Our greatest compliment has been complaints we've received from the operation group about the device being offline, since they are "flying blind" without out it. An example of its use as an important online QA/QC device is shown in Fig. II.A-16. On 08 Mar 01, during run 1209, the PVCD alerted the United Solar QA/QC department to a reduction in material quality. A resulting search identified and corrected a problem in the backreflector machine. At this time offline QA/QC was lagging production by 8 rolls.

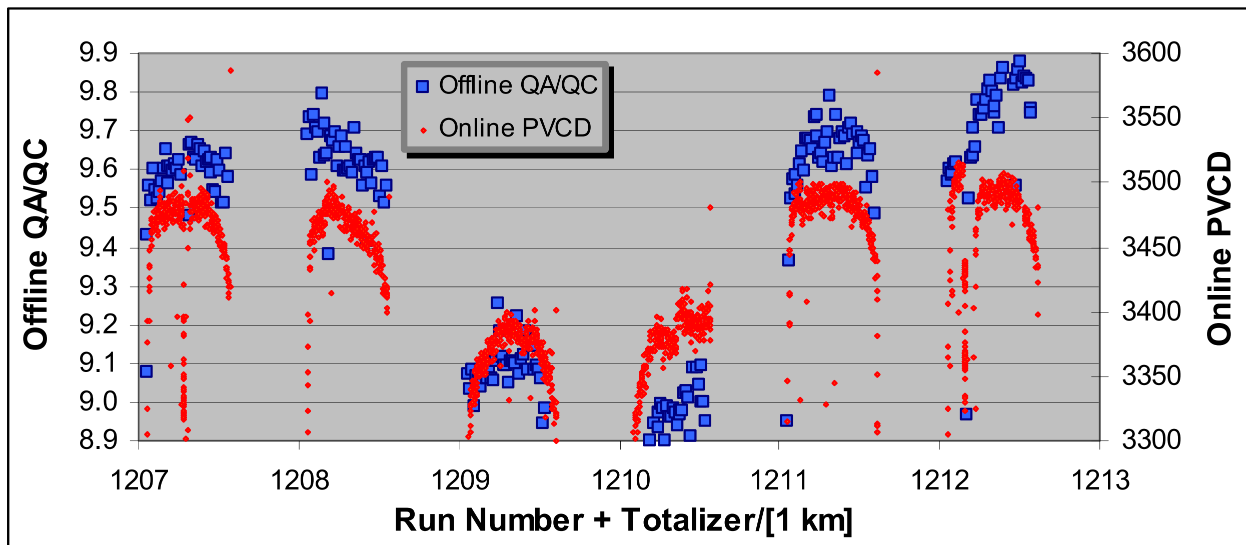

Fig. II.A-16. Raw online PVCD data and offline P_{MAX} data for 5 MW runs 1207 – 1212.

Present Status and Future Plans

The PVCD is presently offline, and will be re-installed within a few days incorporating recent improvements discussed above. We expect that this configuration will be the same as for future systems for the 25 MW equipment that will come online early next year. We shall consequently have a few month period to develop a data base that can be used to help expedite the commissioning of the new equipment. We shall also begin to integrate this system with other online systems, such as the recently-installed thickness monitor. Our long range plan is to develop the expertise and expert systems needed to be able to use this device for continuous online process optimization.

AREA II.B. THE BACKREFLECTOR SCATTEROMETER SYSTEM

Overview And Summary

Motivation and Background

United Solar's triple-junction solar cell design currently employs a backreflector (BR) layer consisting of textured aluminum and thin zinc-oxide (ZnO) to enhance photon absorption in the active solar cell layers. The objective of this portion of the project was to develop an on-line sensor capable of characterizing the surface roughness, or texture, of the aluminum layer deposition. Without such a sensor, information regarding the quality of the aluminum layer can only be gained days later through off-line QA/QC measurements. Extracting the characteristics of the aluminum layer also becomes less clear, after subsequent deposition of the a-Si and ITO layers. An on-line sensor can provide relatively immediate information regarding the texture of the aluminum layer and alert machine operators to any serious process variations. Ultimately, once the optimal texture and its dependence on deposition parameters are determined, the sensor may be used for closed-loop process control and optimization, the overall objective being increased module efficiency and yield.

During the course of the project, two scatterometers were developed. The basic technique is the same for both systems. Laser light is directed at a fixed angle onto the BR surface and a detector measures laser light scattered at various angles. During Phase I, a first generation benchtop system was designed to gain experience and understanding of the measurement technique. It was also used to investigate typical scattering characteristics of various backreflectors and their correlation to QA/QC measurements. This system employed a single arc-scanning photodiode as the receiver with a full 180° detection range.

The second-generation sensor, developed during Phases II and III, was designed for on-line use in United Solar's production BR machine (see Fig. II.B-1). Unlike the benchtop system, this sensor uses a fixed photodiode array as the scattered light receiver and a single fixed photodiode as the specular detector. It has the advantages of a much simpler design with no moving parts. Positioning the sensor at the viewport just after Al deposition results in a relatively fast response time (~5 min.). Also, since mounting is external to the vacuum chamber, no modifications to the machine port were required and future maintenance and calibration may be performed without disturbing production, both of which can be costly.

In addition, a third generation scatterometer is currently being developed for the new United Solar BR machine that will be commissioned early next year. The sensor will be similar to its predecessor. Experience gained through the PVMaT 5A project will be applied to this new sensor.

Summary of Accomplishments

The primary goal of this project was to develop a sensor for United Solar's BR production machine for on-line characterization of the aluminum layer texture. It began with the development of a benchtop system that was used for off-line study of various types of backreflectors, including production and R&D samples. Other surfaces such as

silver mirrors, stainless steels, and diffuse reflectors were also measured to obtain a feel for the relative scattering levels of various materials. Initial correlation studies between scatterometer data and QA/QC data were performed. Correlations were also used to determine which particular scattering angles are required to fully characterize the aluminum texture, and which angles are most sensitive.

The benchtop system yielded important information that was later used in the machine sensor design. In particular, the orientation of the detector with respect to the stainless steel web direction was found to be important. Also, the dynamic range required of the sensor for various backreflector scattering levels could only be determined from bench measurements. The bench system served as a valuable tool for development of the on-line machine sensor.

The second-generation scatterometer was designed for in-line use on the BR production machine. Due to geometry and space limitations imposed by the viewport where it would be installed, the arc-scanning design was not pursued, rather, a design based on a fixed 38-element photodiode array (PDA) was designed for the BR machine. Figure II.B-1 shows a cross sectional view of the scatterometer. In comparison to the arc-scanning system, the “PDA” scatterometer senses a more limited range of scattering angles, 20-50°. Prior to installation on the machine, the sensor was characterized on the bench for linearity, reproducibility, baseline noise, etc. Anti-reflection measures such as an AR coated window and anodized gas-gate port insert were also incorporated.

Since installation in May 2001, the sensor has been in a continuous acquisition and monitoring mode. More than 100 production runs have been logged and the data of many have been subsequently analyzed. From this history of data, several conclusions regarding the capabilities of the sensor can be made. These are briefly summarized here with a more detailed discussion in the following sections. First, the sensor has been shown to be sensitive to serious process malfunctions such as vacuum chamber leaks and aluminum cathode power outages. It has also demonstrated sensitivity to several process parameters. The scatterometer has also shown a greater sensitivity to aluminum texture than subsequent off-line QA/QC cell performance measurements, which is important if it is desired to control the BR-related cell performance based on scatterometer readings. The sensor also was utilized in two instances as an optimization tool, once after the installation of a new flow meter, and again during a web speed experiment. It has also shown sensitivity to different types of aluminum sputtering targets, newly installed aluminum targets, and various stainless steel substrates.

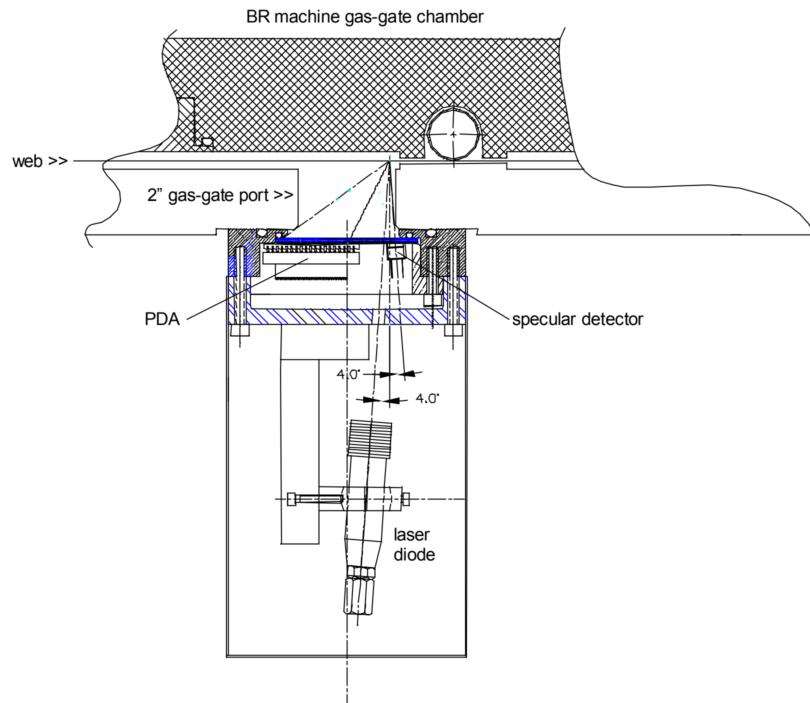

Fig. II.B-1. Drawing of the PDA scatterometer presently installed on United Solar's BR production machine.

PDA Scatterometer Results

The following sections discuss specific examples of PDA scatterometer results and observations. Some were made off-line on the bench during the sensor's development, while others were made on-line during BR production runs.

Detection of Vacuum Chamber Leak

In April 2001, several BR production runs were found to result in subsequent poor cell performance. The cause of the non-standard BR was determined to be a vacuum leak in the BR deposition chamber. Three runs were affected and samples from those runs were measured off-line using the PDA scatterometer which, at that time, was under development on the bench. The sensor produced significantly different scatter signals for the runs with and without the vacuum leak. Two of these runs are shown in Fig. II.B-2. The data are presented in terms of the photodiode pixel voltage versus the scatter angle (similar to BRDF, the bi-directional reflectance distribution function, in scatterometry theory). Run 1109 had the leak, and run 1112 is a later run after the leak was repaired. The scatter (texture) is significantly higher for run 1109. The detected specular signal also dropped by 75% for this run. Had the PDA scatterometer been

operational on the production machine at that time, the leak would have been detected earlier and corrective action would have been taken sooner.

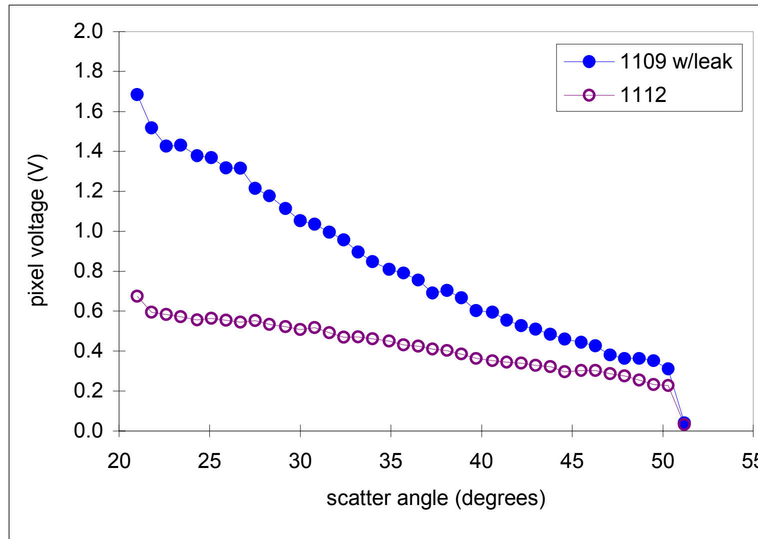

Fig. II.B-2. Plot showing the effect of a vacuum chamber leak on the scatter signal.

Sensitivity to Process Variations and Correlation with QA/QC Cell Data

Experiments were conducted during a BR production run with the objective of determining the sensitivity of the scatterometer to changes in aluminum deposition process parameters. The correlation with post deposition QA/QC cell measurements was also studied. Figure II.B-3 plots integrated scatter (sum of all pixel voltages) versus run meter mark during the course of these experiments that are identified by number on the plot.

The data show that the scatterometer is sensitive to moderate changes in the particular deposition parameters. Although the variation in integrated scatter values is significant, ±10%, variation in final cell I-V parameters was relatively much smaller, ±1% for P_{max}, J_{sc}, and V_{oc}. Also note that experiments numbered 2-5 in the figure are excluded from this correlation discussion since that portion of the run was subsequently lost due to a problem during a-Si deposition. Unfortunately, this portion of the experiment had the largest variations in scatterometer readings. Figure II.B-4 plots two of the stronger correlations between scatter and measured QA/QC cell data. Although the population is small, a correlation with cell open-circuit voltage (V_{oc}) and series resistance (R_s) is evident.

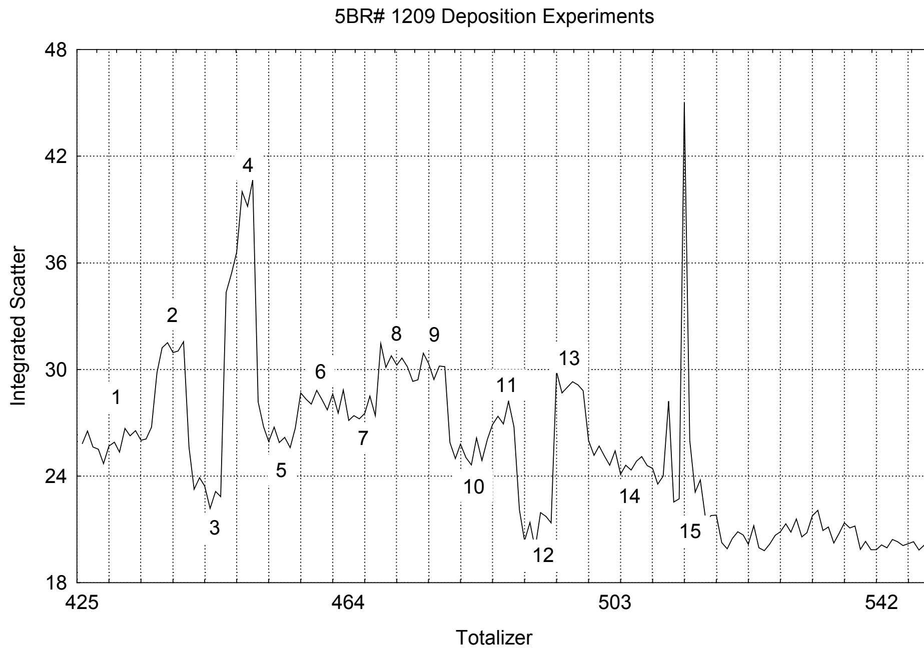

Fig. II.B-3. Plot of integrated scatter during BR deposition experiments.

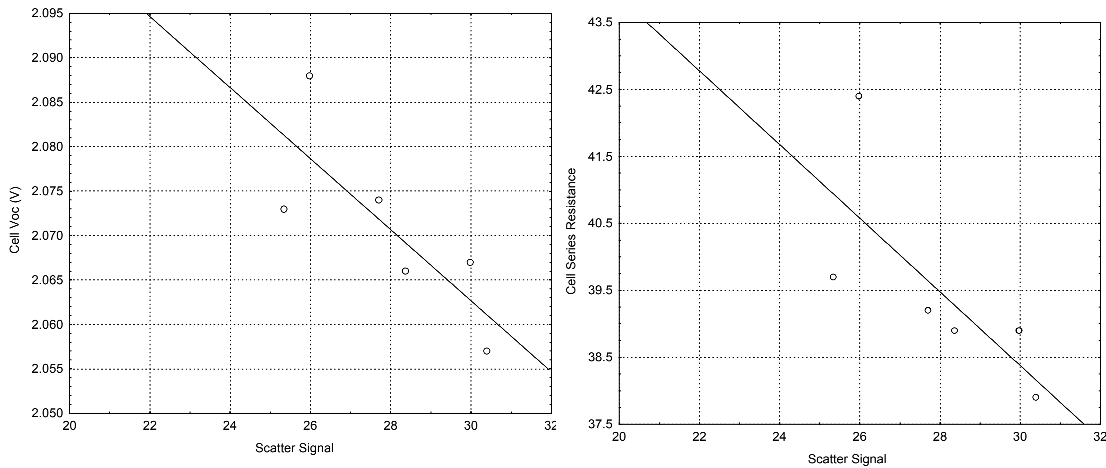

Fig. II.B-4. Plot of cell Voc and series resistance vs. integrated scatter.

Another aluminum deposition experiment was conducted during which a deposition parameter, referred to here as "x", was varied over a portion of the run. Again, the objective was to observe the sensitivity of the scatterometer to process variations and investigate the correlation with post deposition cell I-V data. Figure II.B-5 plots integrated scatter data versus meter mark during a portion of this run. The standard part of the run occurs over 255-305 meters. The experimental part occurs over 225-250 and 310-675 meters. A 100% decrease in deposition parameter "x" resulted in the corresponding 20-30% decrease in scatter signal.

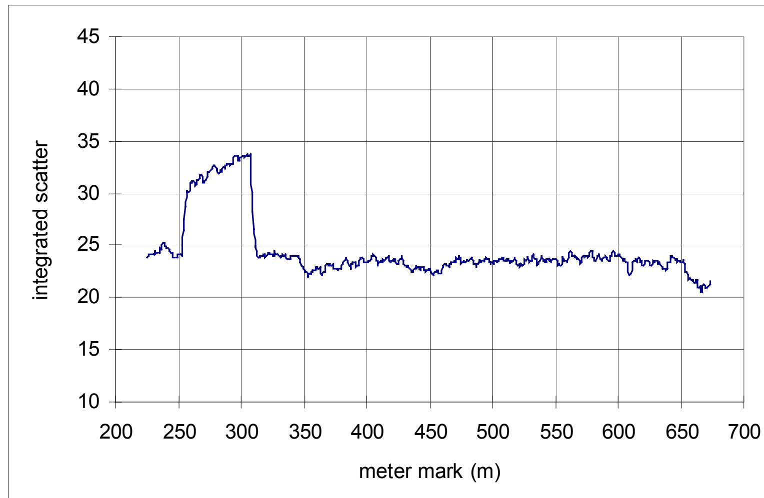

Fig. II.B-5. Plot of integrated scatter during a BR deposition experiment.

Correlation of scatter data with subsequent off-line cell I-V measurements was studied. Figure II.B-6 plots several cell I-V parameters as a function of integrated scatter. Each graph shows two distinct groupings, 1 group corresponding to the lower scatter and the other with the higher scatter. Of the I-V parameters, the cell V_{oc} and series resistance show the most significant correlation. J_{sc} also shows a slight dependence. P_{max} appears independent of scatter level that may be due to the balance between J_{sc} and V_{oc}.

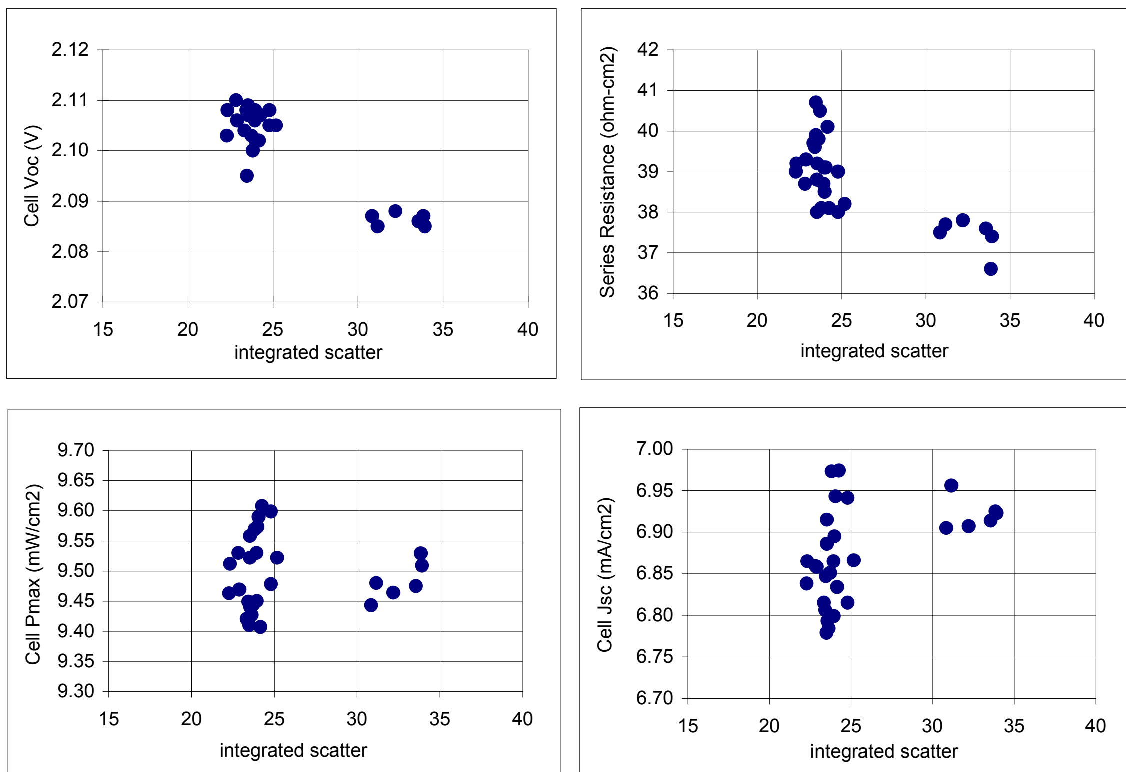

Fig. II.B-6. Plots of integrated scatter versus off-line cell I-V parameters.

Use of the Scatterometer for Process Optimization

In August 2001 a new process controller was installed at the aluminum chamber of the BR machine. The scatterometer was utilized to determine the appropriate setpoints for the new controller by tuning the controller to obtain the "typical" scatter profile. After setpoint optimization, the controller was used together with operator input to obtain a more uniform integrated scatter profile over the course of a run. This "loose" control resulted in a much smaller variation (15-25%) from the beginning to the end of a run when compared to runs prior to the use of the new controller and operator input (25-40% variation).

Figure II.B-7 compares three runs, one with and two without the use of the new controller. Since the optimization of the new controller the scattering level is 10-45% lower than those before this change. The largest differences are observed near the beginning of the run.

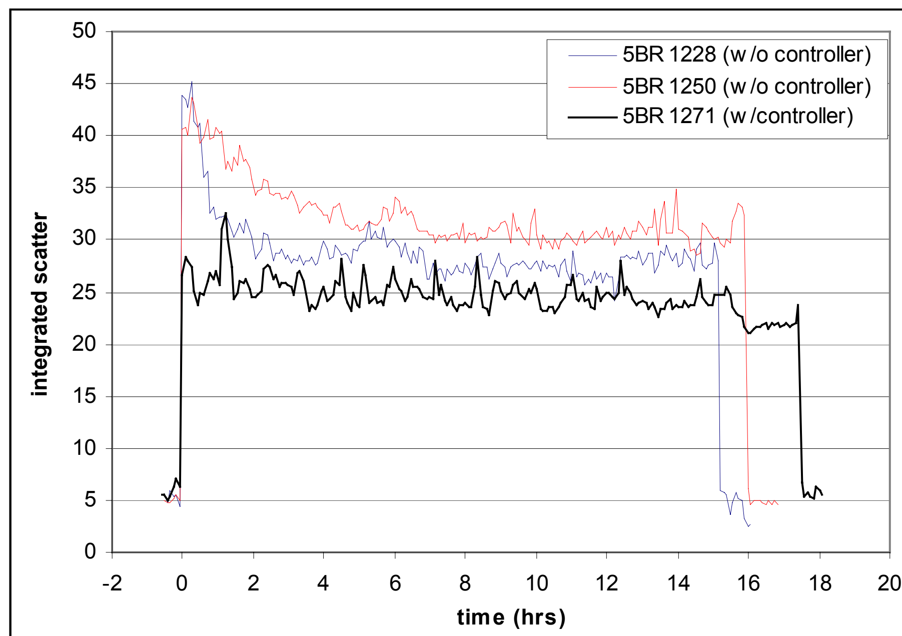

Fig. II.B-7. Plot of three BR runs showing the effect of flow controller.

Recently, web speed experiments were conducted in an effort to explore higher throughput deposition. In this case, the scatterometer was used to tune Al deposition process parameters such as temperature and cathode power, to obtain scattering levels typical of the standard web speed. This coil is presently undergoing subsequent a-Si and ITO processing, and once QA/QC cell data become available, an analysis will be performed.

Sensitivity to Changes in Process Parameters

Sensitivity to Aluminum Sputtering Targets

PDA scatterometer bench measurements were performed on finished cells with different types aluminum back-reflector. One cell used a lower purity (96-97%) aluminum 6061 target for deposition, the other used the standard 99.99% pure aluminum target. Scatter plots are shown in Fig. II.B-8. The cell made with standard BR exhibits 35-50% higher scatter than the cell made from the lower grade aluminum. This is presumably due the greater texture of the standard BR.

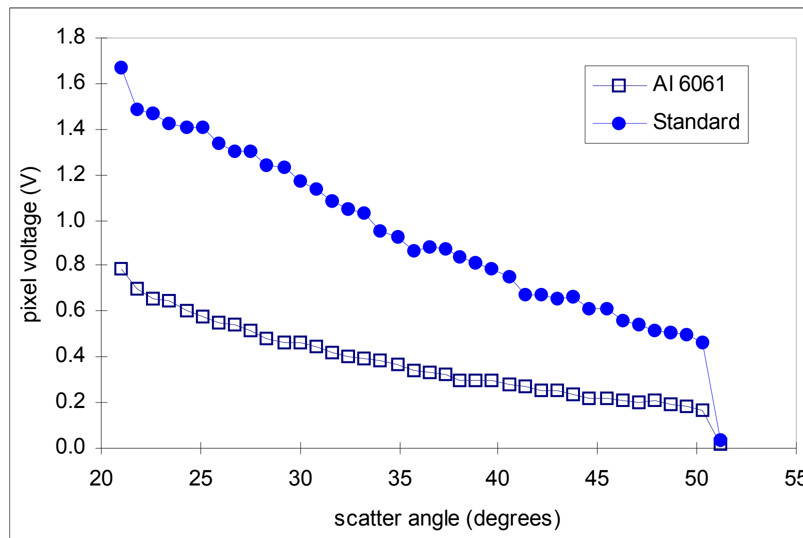

Fig. II.B-8. Plot showing the effect of alternative aluminum BR on the scatter signal.

Sensitivity to Alternative Stainless Steel Substrates

Sections of stainless steel from alternative suppliers are occasionally spliced into the middle of a standard production stainless steel coils for qualification testing. The alternative steel sections generate significantly different scatterometer readings, as compared to the standard steel. Figure II.B-9 plots integrated scatter data over the portion of the run having the alternative steel with the standard steel signal to either side of the alternative steel signal.

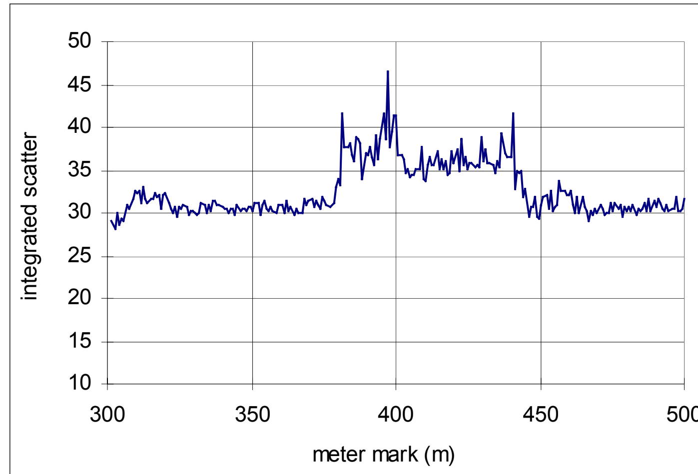

Fig. II.B-9. Plot showing the effect of alternative stainless steel substrate on integrated scatter signal.

The alternative steel shows 15-30% higher scatter signal when compared to standard. It is suspected that differences in the steel manufacturing process may be the cause. Visually, there are differences in surface roughness of the steels, but curiously, these do not correlate with scatterometer data. This result will require further investigation. In any event, the observed variation in scatterometer data due to alternative stainless steel substrates, results in relatively small variations (±1%) in QA/QC cell I-V data. This suggests that cell performance is relatively insensitive to the change in scattering resulting from the use of alternative stainless steels.

Sensitivity to New Aluminum Target Installation

Periodically, new aluminum targets are installed in the BR deposition machine. Accompanying this is a noticeable increase in scattering level (~25%). Figure II.B-10 shows the effect of installing a new Al sputtering target on the integrated scatter profile. The scattering increase is suspected to be a result of the chamber being opened to atmosphere for an extended period of time, or possibly the result of oxidation build-up on the aluminum target. This effect is repeatable and has been observed several times. Again, QA/QC cell performance data (I-V data) is relatively insensitive to the change in scattering due to new targets.

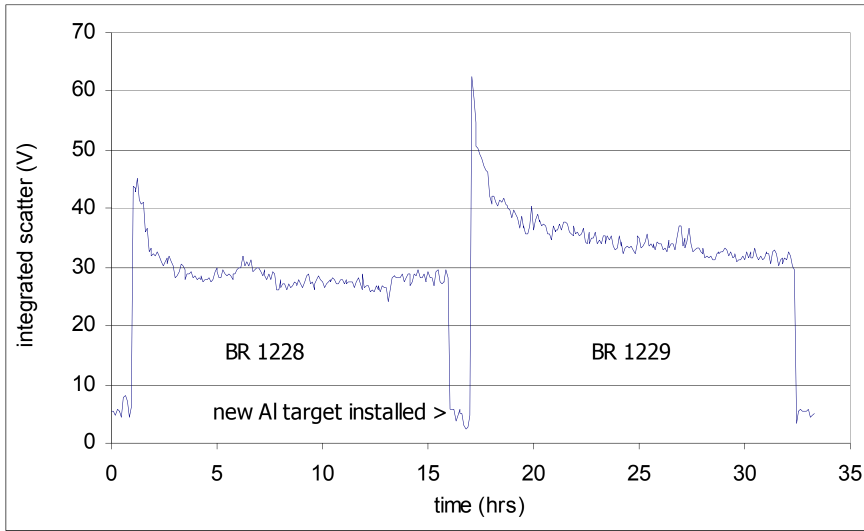

Fig. II.B-10. Plot showing the effect of new Al target installation on integrated scatter signal.

AREA II.C. REFLECTOMETER SPECTROMETERS FOR ONLINE THICKNESS MEASUREMENT

We have worked on the development of 2 online thickness monitoring systems, one for the ZnO thickness in the BR machine, and another for the a-Si machine. Both systems are now online in the 5 MW production equipment. Both systems have proven to be useful for online QA/QC and we plan to incorporate them into the 25 MW equipment, where we also plan to implement them in feedback loops to control the film thickness.

BACKREFLECTOR SPECTROMETER

Overview And Summary

Motivation and Background

United Solar's triple-junction solar cell design currently employs backreflector (BR) and top conductive oxide layers. The BR layer consists a sputter deposited textured aluminum with overlaid thin zinc-oxide (ZnO). The top conductive oxide layer consists of indium-tin-oxide (ITO). It is desired to monitor and control the thickness of the ZnO and ITO layers in order to achieve consistent cell quality. The objective of this portion of the project was to develop on-line sensors capable of accurately sensing the thickness of these two layers. Once optimal thickness and their dependence on deposition process parameters are determined, the sensors may be used for closed-loop process control and optimization, the overall objective being increased module efficiency and yield.

Two systems have been developed, one for BR ZnO layer thickness and the other for ITO layer thickness. Both are based on fiber-optic spectrometers that are computer-interfaced for instrument control and data acquisition. A basic schematic is shown in Fig. II.C-1. Operator interface and data display software has also been developed for these systems. The basic technique is the same for both systems: white light, supplied by a halogen light source, is directed via fiber optic onto the deposited layer. Detection fibers receive the reflected light from the layer and transmit it back to the spectrometer. The spectrometers are sensitive to wavelengths of 360-1000 nm. Software performs data acquisition, spectral analysis, and estimates layer thickness based on reflection interference minima and maxima. Results are displayed to the monitor at which point the operator may be alerted to non-standard layer thickness and take corrective action. This is presently done for the ITO process.

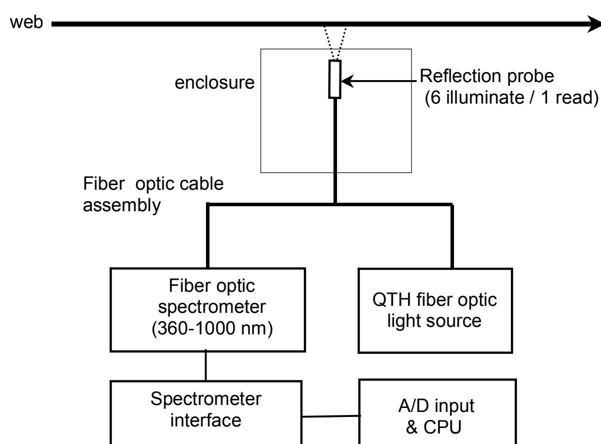

Fig. II.C-1. Schematic of the on-line BR and ITO reflectometers.

Summary of Accomplishments

The on-line BR reflectometer was installed on the production machine in November of 1999 and has been operated intermittently since then. Over that time the ZnO reflectometer has demonstrated monitoring and diagnostic capabilities. The device has demonstrated effectiveness in detecting serious process malfunctions such as outages in ZnO cathode power and vacuum chamber leaks. It has also shown sensitivity to many other BR process parameters. It also appears to show sensitivity to the specularity of the total BR layer. Based on experimental data thus far, it appears the sensor has sufficient sensitivity for characterizing the ZnO layer with respect to final cell performance. Additional experiments are required to determine the ultimate sensitivity of the sensor to very small process changes.

The ZnO reflectometer has also shown to be effective as a process optimization tool. It has been used to tune the deposition process in several cases. It has also demonstrated its potential for use in production monitoring and control. Once the optimal ZnO thickness (i.e. reflection curve) and its dependence on process parameters are determined, it should be possible adjust and control process parameters to achieve the target thickness, preferably in a closed-loop mode.

BR Reflectometer Results

Design and Installation on the BR Production Machine

The BR reflectometer was installed at an existing port located at gas-gate 3 of the machine chamber. After design and fabrication of the mounting hardware for the fiber optic reflection probe, installation was fairly straightforward. The probe is positioned just beyond the last ZnO deposition chamber, near the center of the web, allowing the fastest possible response time to process changes. The system was also designed to be mounted external to the vacuum chamber to eliminate any potential interference with the production process. Two-axis positioning (x-z) of the fiber optic probe was built in to

the mounting hardware. Calibration is periodically performed on the bench using a specular reference such as a front surface silver mirror.

Software was developed for instrument control and data acquisition. Data may be acquired and stored at user specified intervals, typically 1-5 minutes, during the course of a run. The software performs spectral analysis and logs reflection minima and maxima and measured specular reflection values at these points. Data are also displayed to the computer screen for monitoring purposes.

Initial On-Line Observations

Approximately 20 BR production runs were acquired and investigated during Phase II of this project. A "typical" normalized reflection curve is shown in Fig. II.C-2 below. The present thin ZnO layer recipe yields only one reflection minimum over 800-900 nm, and one reflection maximum near 500-600 nm.

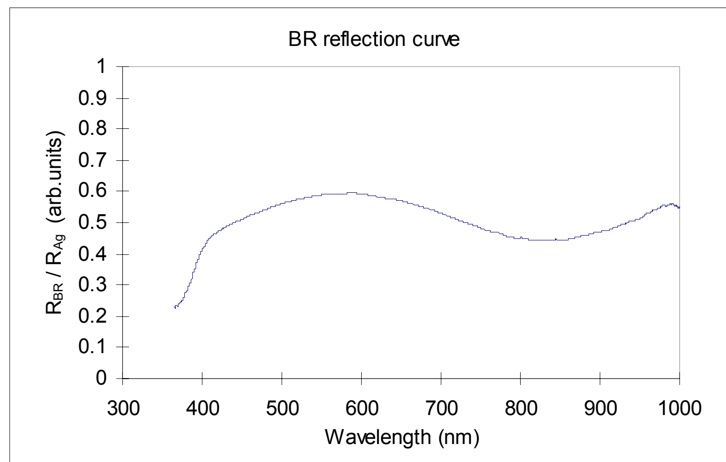

Fig. II.C-2. Plot of typical standard ZnO layer reflectance.

As shown in Fig. II.C-3, tracking the reflection minimum and maximum over the course of an entire production run (~15-18 hours) shows very small variation of ± 2% from the beginning to the end of run.

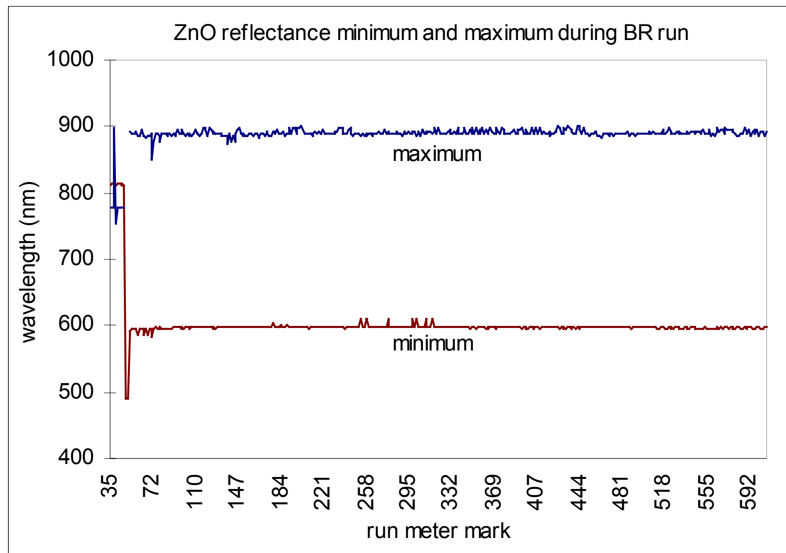

Fig. II.C-3. Trend plot of standard ZnO reflectance minimum and maximum during a production run.

Another repeatable effect that is observed from run to run is that both the maximum and minimum reflection values gradually increase by 40-50% over the first one-third of standard BR runs (shown in Fig. II.C-4). This suggests that the specularity of the BR is increasing since the fiber optic probe is primarily detecting normal reflection. Also, since the BR specularity presumably is dominated by the aluminum layer texture, the reflectometer may in effect be sensing aluminum layer texture. Correlations between ZnO reflectometer and Al scatterometer data will be investigated to determine its validity. The 5% noise observed in Fig. II.C-4 is due to displacement of the web as it travels.

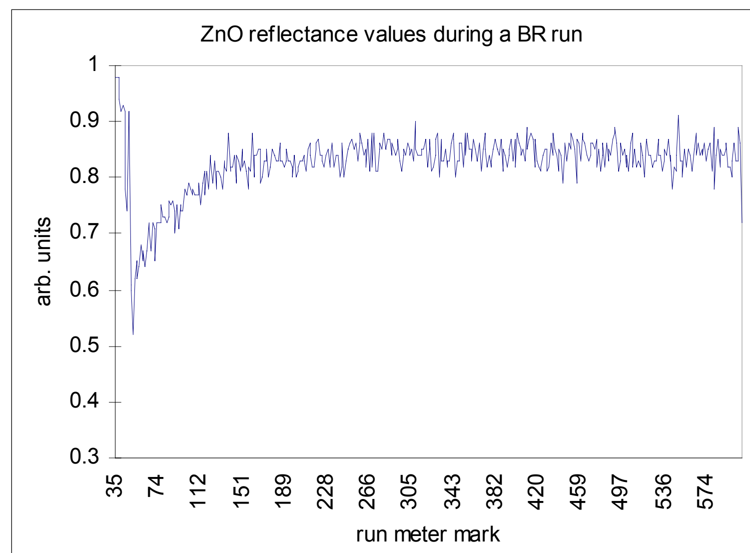

Fig. II.C-4. Plot of ZnO reflectance value at the maximum during a production run. (Note the start of the run occurs near 45 meters).

The 3-5% noise observed in Fig. II.C-4 was found to be the result of web displacement, or flexing, as it travels over the ZnO reflectometer. An experiment was performed to confirm that the noise was really web related. For consecutive spectrometer scans under static web conditions, the variation per pixel is less than 0.5%. For consecutive spectrometer scans under moving web conditions, the variation per pixel increases to 3-5%, confirming that web flexing contributes significant noise. Signal averaging or positioning the sensor directly below a magnetic roller would help to minimize this noise.

Correlation to Process Variations and QA/QC Cell Data

Several of the runs analyzed thus far have incorporated ZnO layer experiments. These experiments have involved variation of process parameters such as ZnO cathode power, web temperature, web speed, and sputtering method. Based on data acquired by the reflectometer, it appears to be fairly sensitive to many of these process parameters.

A brief experiment was conducted during a production run to determine the sensitivity of the reflectometer to ZnO thickness variation. One of six ZnO cathodes was disabled for a short period during a run. This effectively reduced the ZnO thickness by a factor of 1/6. As the sensor measured this section, a significant shift in the reflection minimum was observed and is shown in Fig. II.C-5. The data suggest that the sensor is very sensitive to cathode power changes and therefore ZnO thickness variations.

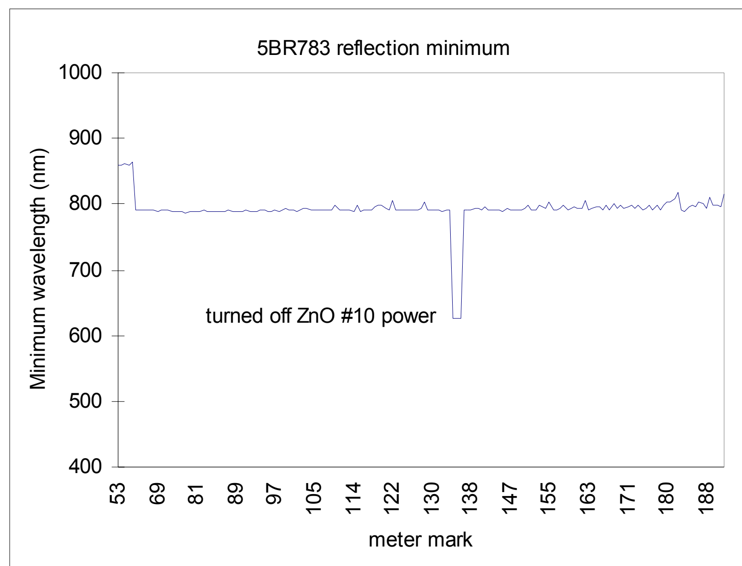

Fig. II.C-5. Plot showing the change in the reflection minimum where ZnO thickness was reduced.

Another BR run experimented with web speed, ZnO cathode power (current), and process temperature variations. The ZnO cathode power variations resulted in significant differences in measured reflectance as shown in Fig. II.C-6. Increasing the cathode power increased reflection values and shifted the maximum and minimum towards longer wavelengths. These data show that the reflectometer is fairly sensitive to

ZnO power variations. In addition, the sensor is much more sensitive than subsequent off-line QA/QC cell data that show less than 0.5% variation in P_{max}, J_{sc}, V_{oc}, and FF.

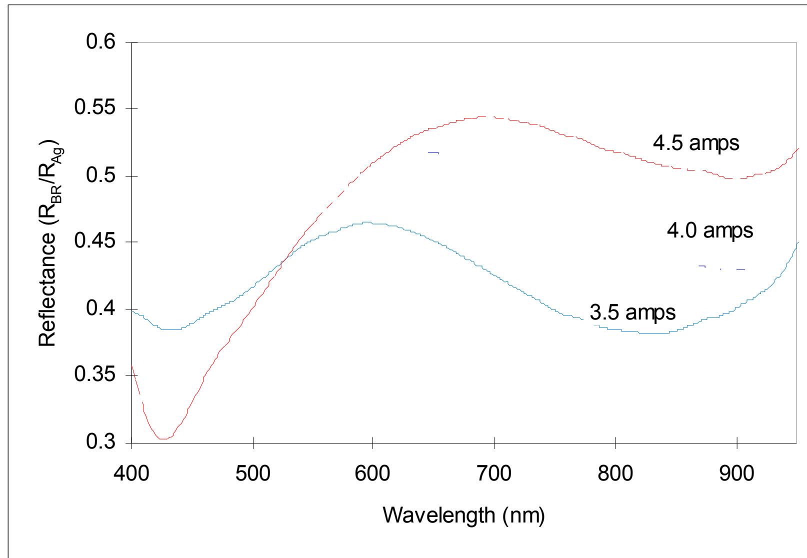

Fig. II.C-6. Plot showing dependence of ZnO reflectance on cathode power.

For another experiment, a different BR deposition parameter was varied. The recorded reflection data was analyzed to observe the sensor's response to this parameter change. Five reflection curves taken several minutes apart over a 25-minute period are shown in Fig. II.C-7. These curves were recorded while the process was in transition. As seen in this figure, the reflection signal decreases with time. The process change resulted in an overall 15% decrease in BR specular reflection as seen by the downward shifting curves in Fig. II.C-7. The shape of the curves (i.e. reflection maximum and minimum) did not change significantly. Subsequent QA/QC cell data showed changes of about 1%, again suggesting the reflectometer is sufficiently sensitive to process variations and resulting cell performance.

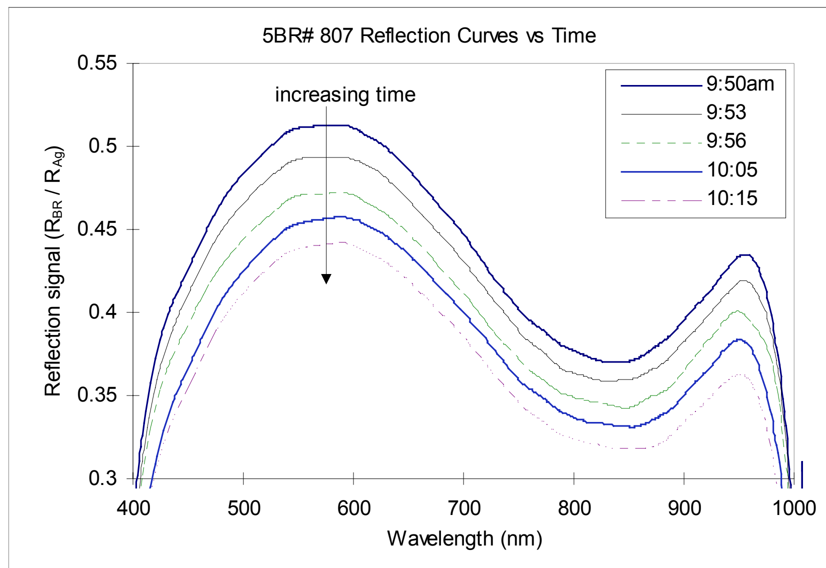

Fig. II.C-7. Plot of 5 reflection curves recorded over a 25-minute period during BR process transition.

Effective Use as a Process Optimization Tool

The ZnO reflectometer also demonstrated its potential use as a process optimization tool during an experimental run employing reactive-ZnO sputter deposition. The reactive-ZnO process utilizes a metal Zn target in a reactive oxygen atmosphere, whereas, our standard production ZnO process utilizes a ceramic ZnO target in an inert atmosphere. The sensor was used to determine the equivalent reactive-ZnO sputtering power required to produce typical standard production ZnO layer thickness (i.e. reflectance curve). The reactive-ZnO sputtering power was adjusted until the reflectance curve was similar to that of standard ZnO deposition. Fig. II.C-8 compares data of standard ZnO deposition to those of the reactive-ZnO. The minimum and maximum are similar, although a 9-12% higher reflection signal is observed for the reactive ZnO film over 450-1000 nm, possibly indicating that the reactive-ZnO film is more transparent than the ceramic sputtered film.

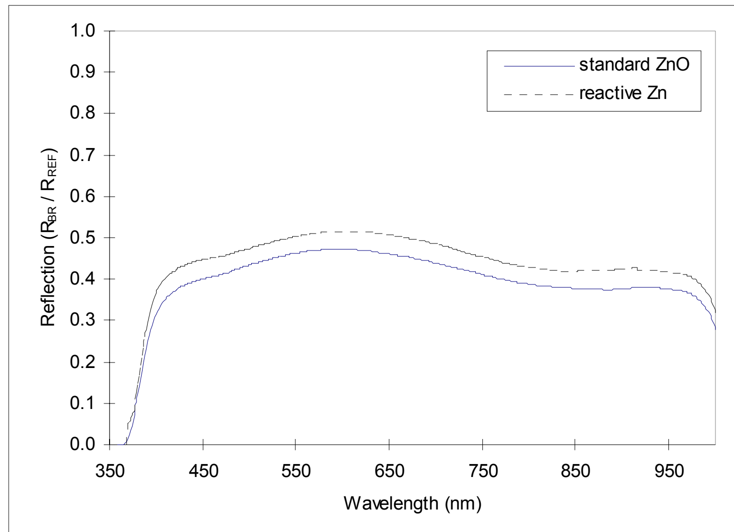

Fig. II.C-8. Plot comparing standard ZnO and reactive-ZnO reflection curves.

Subsequent off-line QA/QC cell data for standard and reactive-ZnO deposition were within 1.2% as shown in Table II.C-1 below, suggesting that the optimization was successful.

Table II.C-1: Comparison of Standard and Reactive ZnO deposition QA/QC cell I-V data.

Conditions	Pmax	Jsc	Voc	FF
standard	9.839	6.887	2.127	0.672
reactive-ZnO	9.722	6.860	2.121	0.668
% difference	1.2	0.4	0.3	0.6

In addition, the ZnO reflectometer was recently used for optimization of ZnO layer thickness during web speed experiments. The sensor was used to successfully tune ZnO process parameters for typical standard thickness.

THE AMORPHOUS SILICON SPECTROMETER SYSTEM

Overview and Summary

Motivation and Background

The United Solar 5MW a-Si Machine deposits a triple junction PV cell onto a stainless steel substrate. Performance of the resultant PV material is affected by variations in the thickness of the individual layers. Without the ability to monitor this thickness the machine operator is limited in identifying potential problems. The performance of the PV would not be qualified until the off-line QA/QC process. This is typically several days after the manufacturing process and could result in the production of significant amount of lower performance material.

The thickness of PV layers can be measured and monitored using commercial spectrometer systems. These systems are based on the interference spectrum produced when white light reflects off of a thin film. Fiber optics transport the light to the PV substrate and carry the reflected signal back to the spectrometer for processing. The reflected light is passed through a diffraction grating and the resulting spectrum digitized with a CCD array. The extrema of the interference pattern are proportional to the thickness of the PV layer.

A reflectance spectrometer has been recently installed in the web take-up chamber of the 5 MW a-Si Machine. At this location the device will be monitoring the combined thickness of the three PV layers. This spectrometer will provide the operator with a real-time diagnostic for identifying and maintaining PV thickness. As proposed in the PV Manufacturing R&D program, spectrometers could be placed at various stages in the deposition process and thus provide the thickness of individual layers. These devices could then serve as the input to a closed-loop feedback system to the manufacturing process.

Summary of Accomplishments

An Ocean Optics Spectrometer system was purchased and setup as part of an off-line Developmental Test Stand. This setup was used to:

- develop data acquisition software with a user-friendly interface
- test spectrometer effectiveness in measuring United Solar PV materials
- develop methods for spectrometer calibration and quantify measurement stability
- test/qualify components for the 5MW a-Si Machine spectrometer system

A second Ocean Optics system was purchased for the 5MW a-Si Machine. This system was installed in September 2001 and produced immediate results. Off-line data analysis has demonstrated correlations of changes in thickness to (what used to be) acceptable changes in machine control points. The measured precision and resolution of the spectrometer has opened up exciting new possibilities for future work under the PV Manufacturing R&D Program.

Developmental Test Stand

Hardware and Software

The Developmental Test Stand uses an Ocean Optics Model USB 2000 desktop spectrometer. A precision mechanical mount holds samples of United Solar PV materials in a secure and reproducible manner. Adjustments in the mount permit changing the distance between the sample and the spectrometer lens for sensitivity studies.

Data acquisition software and an Operator interface were developed using National Instruments ***LabView***. Shown in Fig. II.C-9 is the operator panel for selecting the extrema to be tracked. The software will acquire a new spectrum at a specified rate, determine the extrema wavelengths and amplitudes, and datalog these results to a file.

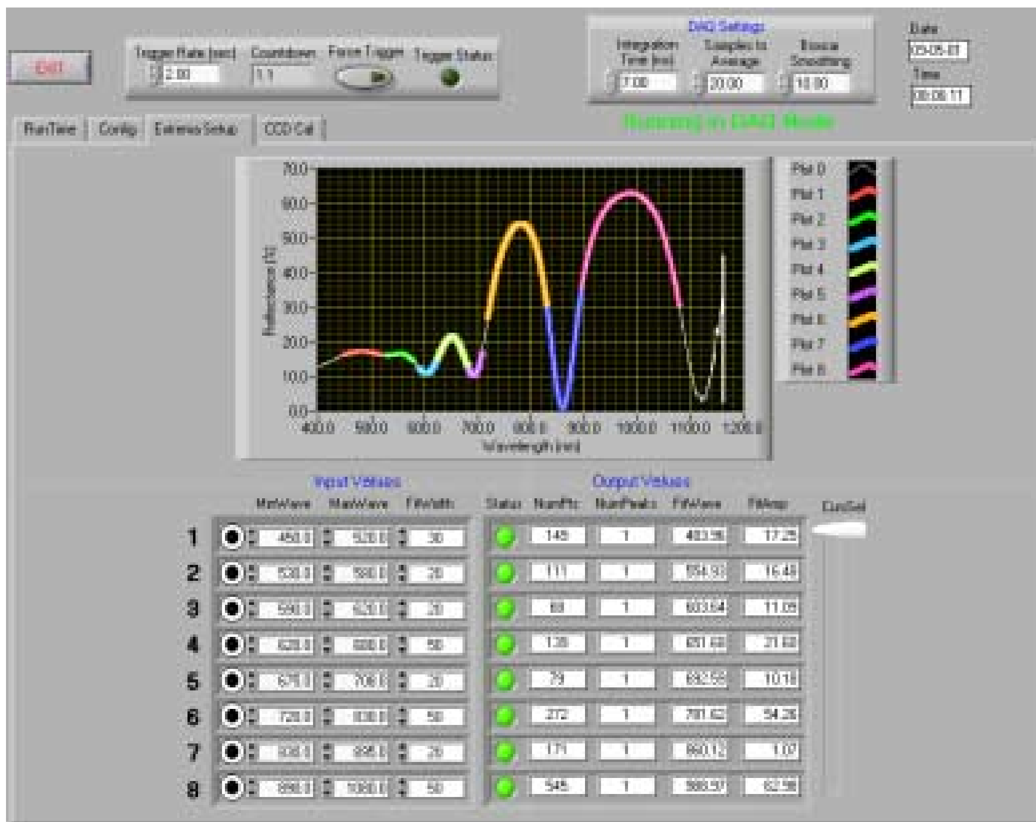

Fig. II.C-9. ***LabView*** control panel for selecting extrema to track.

Spectrometer Stability and Precision Measurements

Shown in Fig. II.C-10 is a typical spectrum acquired for a triple a-Si layer PV sample. The six extrema in Fig. IV-10 were tracked over a 60 hour period. The relative changes are plotted in Figure II.C-11 and demonstrate a typical RMS precision of ~ $2x10^{-4}$.

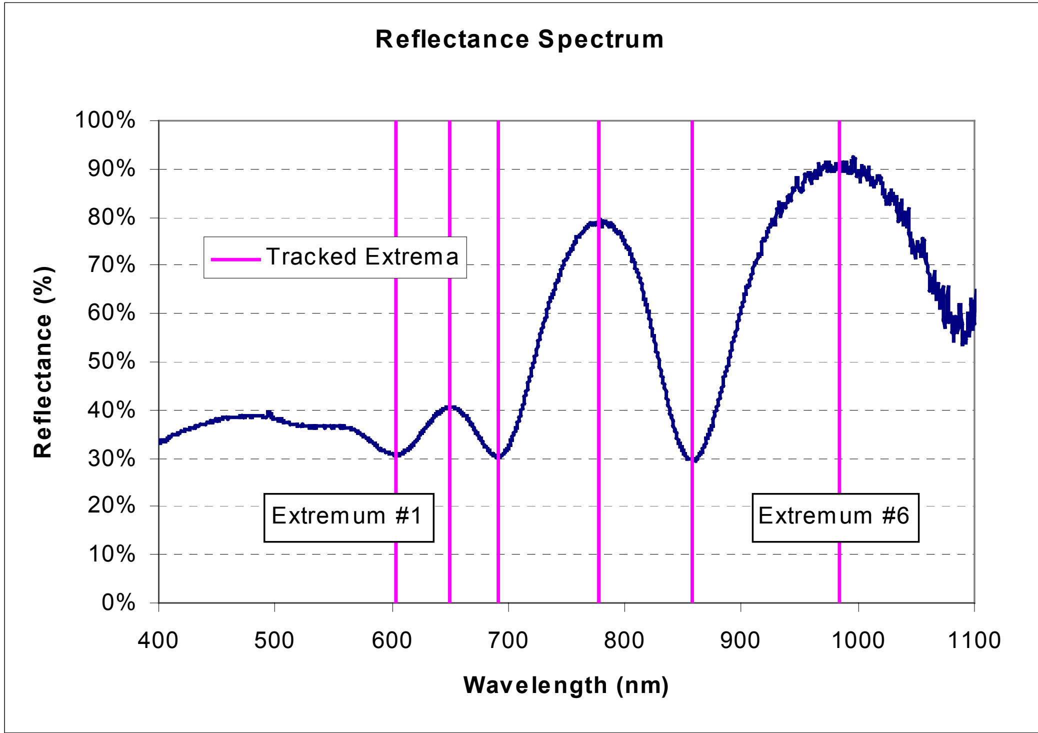

Fig. II.C-10. Reflectance spectrum from triple layered a-Si sample

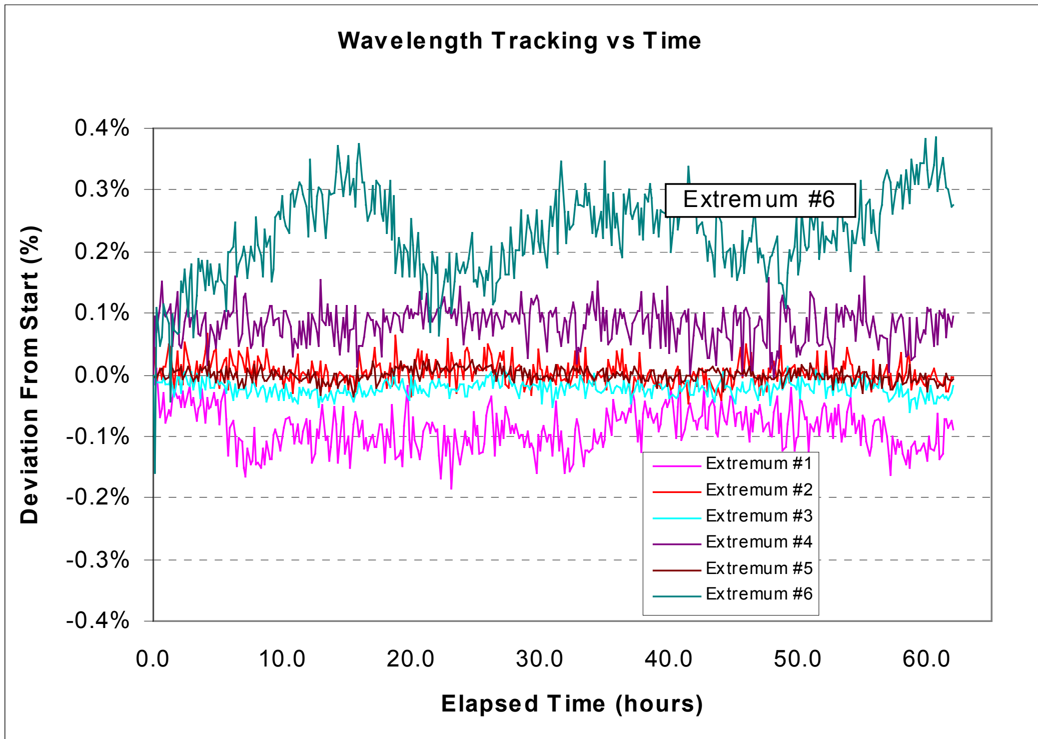

Fig. II.C-11. Spectrum extrema tracking precision over time.

Positional Sensitivity Measurements

Measurements were made to quantify the effect of positional changes between the spectrometer lens and the measured sample. This was a concern for the 5 MW system where the spectrometer views the photovoltaic web as it contacts a large roller. Small concentricity errors in the roller would show up as positional changes between the web and the spectrometer lens.

For the measurement a sample of triple layer PV material was mounted on a slide and translated in 1 mm steps over a 10 mm range. The slide was fabricated with sufficient precision to minimize angular changes (i.e. translated parallel to lens.) Figure II.C-12 plots the percent change in the wavelengths of the extrema as a function of sample position. Over the 10 mm travel the two wide extrema show changes of ~0.2% while the narrow extrema are stable at the 0.02% level. In the 5 MW Machine positional changes are expected to be well under 1 mm. Therefore, these data demonstrate that small positional changes will have no measurable effect on the final thickness determination in the 5 MW Machine.

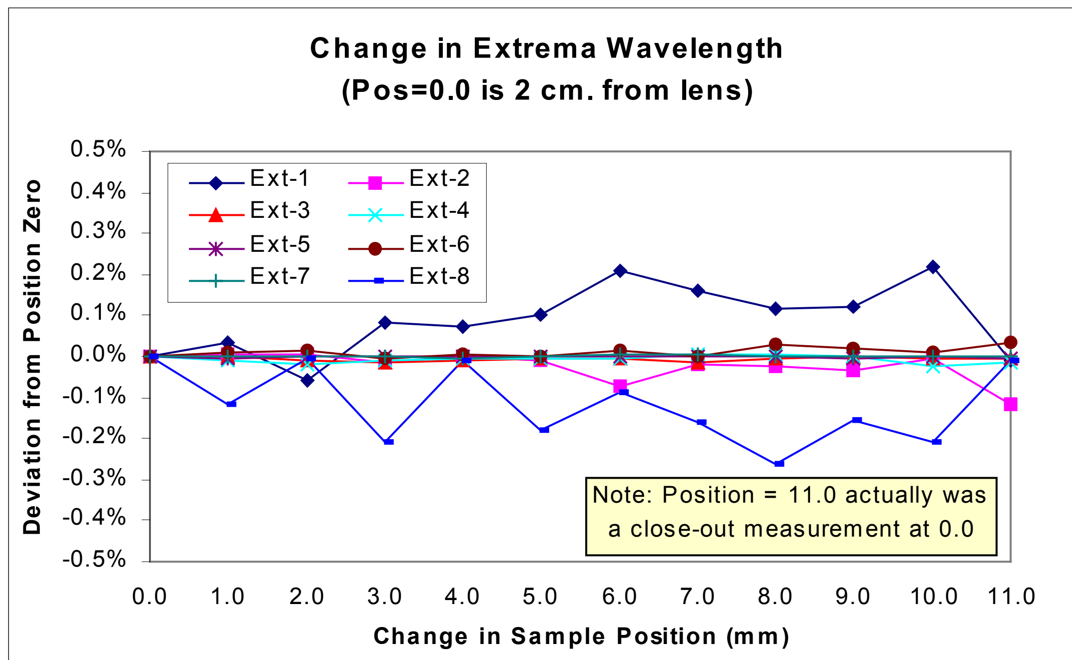

Fig. II.C-12. Extrema wavelengths versus sample position.

5 MW a-Si Machine Spectrometer

Hardware and Software

A rack-based Ocean optics spectrometer system was purchased for operation in the United Solar 5 MW a-Si Machine. The optical pickup was mounted inside the Take-Up Chamber (Fig. II.C-13) and will thus be monitoring a web with all three a-Si layers. A rack-mounted system was chosen for it durability and its applicability to a manufacturing environment. This system also contains a second spectrometer channel to monitor light source stability, temperature controllers for the CCDs, and a calibration light source. These features target the long-term stability and accuracy required in a manufacturing program.

Fig. II.C-13. Spectrometer fibers mounted in a-Si Take-Up chamber.

The spectrometer lens mounting bracket has provisions for the attachment of a calibration slide. This slide can be a precision mirror for reference measurements or a known PV sample for system calibration. Data acquisition is performed using the same software package previously described for the Developmental Test Stand spectrometer.

Data Analysis

The spectrometer system began collecting data immediately after installation. The first runs began showing interesting changes in thickness coinciding with minor changes in machine operational parameters. Shown in Fig. II.C-14 is the shift in the spectrometer interference pattern created when a RF plasma was intentionally shut down. The change in extrema wavelengths, and thus thickness, is shown in Fig. II.C-15 for this event.

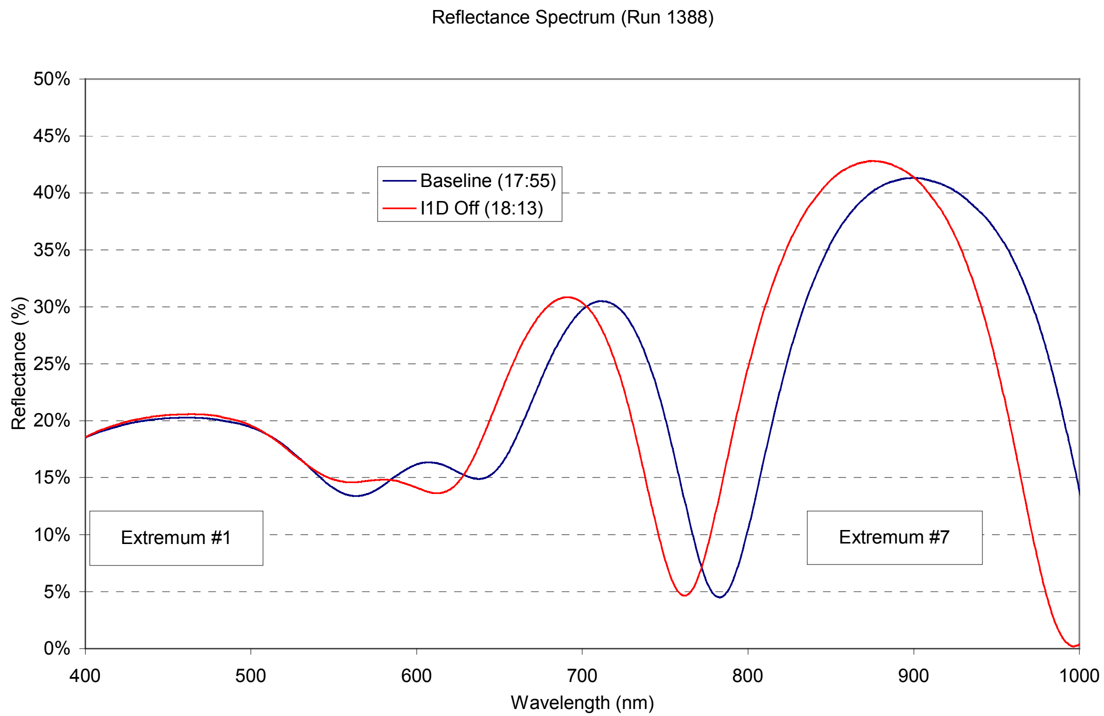

Fig. II.C-14. Change in interference pattern from loss of plasma rf.

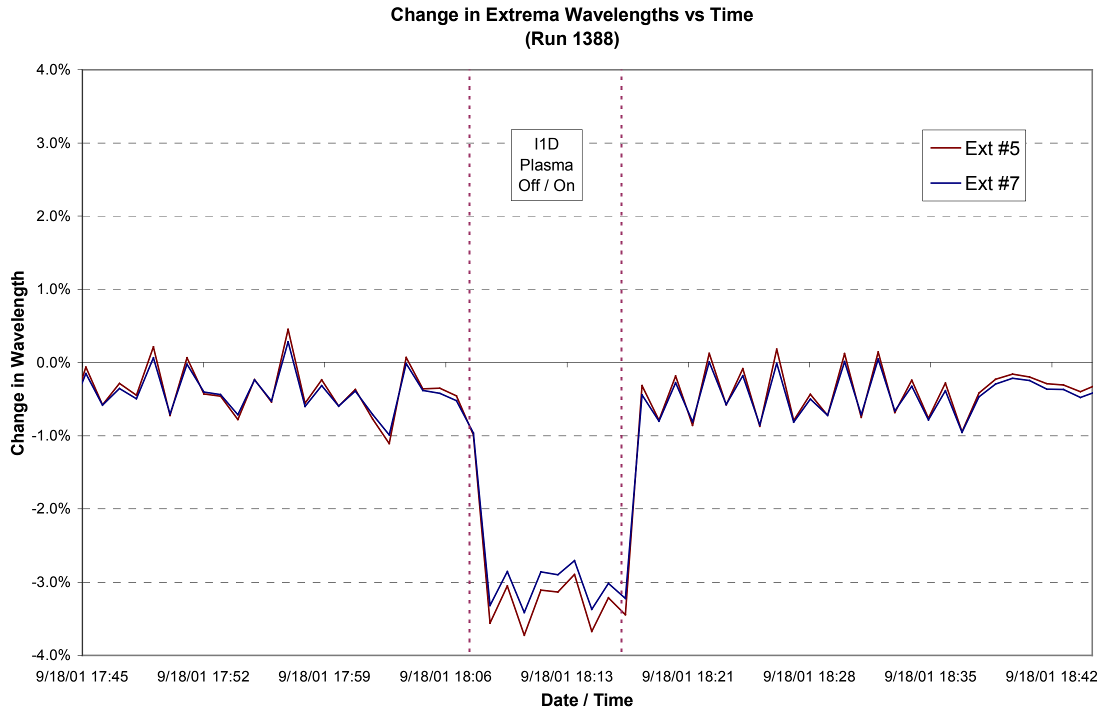

Fig. II.C-15. Resulting wavelength (i.e. thickness) change.

Shown in Fig. II.C-16 is a second event caused by the unscheduled shutdown of a RF plasma. Also plotted, is the reflected power from the machine parameter data archiver. One can see that after the plasma was reset the reflected power was higher and oscillating. The resultant change in thickness is clearly observed.

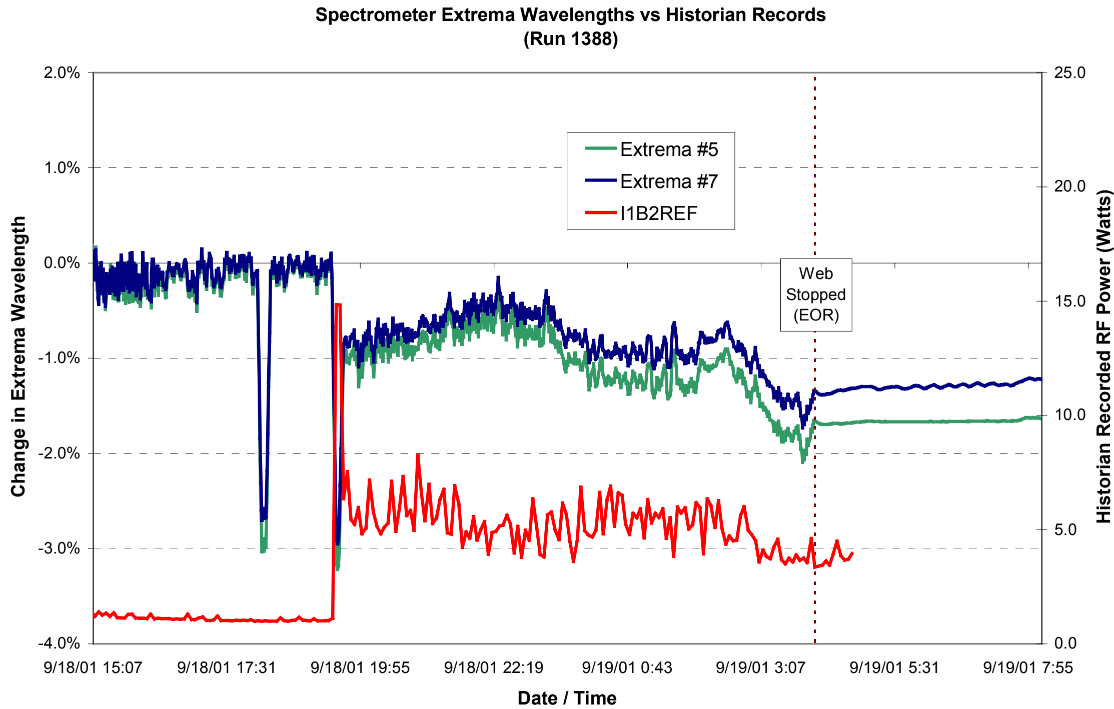

Fig. II.C-16. Resulting wavelength (i.e. thickness) change.

Conclusions And Future Plans

After only a few weeks of operation the data being collected by the 5 MW a-Si spectrometer are exciting and full of potential. Combined with the Developmental Test Stand Spectrometer these systems will provide a powerful tool in developing a thickness monitoring program at United Solar. Near-term work involves automating the off-line analysis and adding it to the run-time displays for the machine operators. Long-term efforts, as proposed in PV Manufacturing R&D program, involve instrumenting the United Solar 25 MW machines with thickness monitoring spectrometers. The experience gained from the operation of these systems will ultimately lead to using these devices for closed-loop process control.

AREA III. Tasks 3 and 7 – Development of Reactive Sputtering Process Using Inexpensive Zn Metal Targets for Back Reflector Preparation

Summary

In this part of the program, a reactive sputtering process was developed for the preparation of ZnO layers of the back reflector. With this process, inexpensive ZnAl metal targets are used rather than ZnO which are presently used in the 5MW production line. Implementation of this reactive sputtering process in the 5MW production line will lead to a 5% decrease in overall raw material cost for fabricating the solar modules.

In Phase I of the program (task 3), a pilot roll-to-roll machine was used to demonstrate the feasibility of using this new process to fabricate small modules in a roll-to-roll manner. A number of deposition parameters were varied including the oxygen flow, applied rf power and the web temperature in order to optimize the back reflector performance. It was shown that modules with similar efficiencies to those made with the standard process could be made using the less expensive reactive sputtering process. This is demonstrated by the data in Table III-1 that compares the performance of a module made using the standard 5MW production process with one made under nominally the same conditions except for the use of the reactive sputtering process. The difference in the values for the module efficiencies is within experimental error.

Table III-1. Data for 44.5 cm^2 Modules Made with Different Backreflectors.

Target Material	BR Machine	J_{sc}(QE) (mA/cm^2)	V_{oc} (V)	FF	R_s (Ω/cm^2)	Efficiency (%)
ZnAl(5%) metal	Pilot	18.9	0.77	0.631	0.20	9.18
ZnO	Standard 5MW Production	18.5	0.77	0.649	0.18	9.24

In Phase II of the program (task 7), the new reactive sputtering process was tested using the 5MW production line. To initially optimize the deposition conditions for the reactive sputtering process in the 5MW back reflector line, a web was coated with several experimental back reflectors prepared under a variety of conditions. Again it was shown that following optimization of the deposition parameters, modules made using the new reactive sputtering process have similar module performance to those made using the standard back reflector fabrication process.

After developing and demonstrating the feasibility of using this new reactive sputtering process, the process has been incorporated into the design of the 25MW plant being built by ECD for United Solar. This will lead to a significant cost savings for the fabrication of the solar modules.

Background

An integral part of ECD's triple-junction solar cell design is the textured metal/ZnO back reflector which enhances the probability for multiple light passes through the semiconductor absorbing material. The increased number of passes increases the chances for light absorption which in turn leads to higher short circuit currents and higher cell efficiencies. While the back reflectors are needed in order to achieve certain efficiency goals, the cost of making these materials on the production level is significant. In particular, the materials costs exceed those for the semiconductor layer deposition process.

A significant expense in the magnetron sputtering process used to make the back reflectors is the cost of the ZnO targets. The cost of these targets alone accounts for over 40% of the total material cost for producing all of the thin films for the solar modules. Thus, if the ZnO targets could be eliminated from the process with a less expensive target, a significant cost savings would result.

Prior to this program, the ECD research team tested a reactive sputtering process that uses a Zn metal target in an Ar/O_2 atmosphere to create ZnO films for back reflectors. Since the price of Zn metal targets are $1/5^{th}$ the price of ZnO targets, and conceivably could be made in-house at an even lower cost, reduced cost was a major incentive to test the feasibility of this process. However, there were other motivations. With the present process, high quality back reflectors are obtainable at production level web speeds. However, at slower speeds (2/3 of the production level speed) back reflectors of even a higher quality can be obtained due to thicker ZnO layers obtainable at these slower speeds. Thus if higher sputtering rates could be obtained, the thick ZnO layers and higher quality back reflectors could be obtained at production level speeds. Since higher deposition rates are likely obtainable with the Zn metal target, improved efficiencies as well as reduced costs may be had with this new process.

Table III-2 compares data from this initial feasibility study for single-junction a-Si:H cells prepared with back reflectors (Zn 29 and Zn 33) made using this new deposition process and cells made with back reflector from the 5MW production machine (5MWBR78 and 5MWBR82). The semiconductor layers for all of these cells were co-deposited in the same deposition chamber under deposition conditions which were not optimized. ITO and Ag contacts for the cells were also co-deposited in order to minimize any differences in the cells other than the back reflector materials. The data for samples Zn 29, 5MWBR78 and 5MWBR82 are all the same within experimental error. The J_{sc} for sample Zn 33 is higher than the other values, however the FF is lower with an overall slight improvement in efficiency. Thus, with little optimization it can be concluded from this data that back reflectors can be made using the new reactive sputtering process, having similar quality to those made using the present 5 MW process.

Table III-2. Comparison of Data for a-Si:H Cells Co-Deposited on Al/ZnO Backreflectors. Cell Measurements Completed Using AM1.5 Light (R_s is the series resistance).

Sample	V_{oc} (V)	J_{sc} (mA/cm^2)	FF	P_{max} (mW/cm^2)	R_s (Ωcm^2)
Zn 29	0.952	14.54	0.644	8.91	10.7
Zn 33	0.955	15.06	0.638	9.19	11.5
5MWBR78	0.953	14.45	0.647	8.92	11.9
5MWBR82	0.953	14.30	0.646	8.80	12.5

Objective of Backreflector Studies

While the data from the initial studies are encouraging, there are several issues which need to be addressed before this new process can be incorporated into the 5MW production line. Although some of these issues can be addressed using small-scale machines, the process needs to be qualified on ECD's pilot roll-to-roll machine before implementing it in the production facilities.

In this program, we tested the feasibility of using this reactive sputtering process in a roll-to-roll process to verify that it can indeed be used to make long rolls of back reflector coated stainless steel webs in production. A pilot roll-to-roll machine was used to prepare and optimize ZnO layers prepared using the Zn metal targets. During initial optimization of the deposition conditions, small area cells were fabricated using the new ZnO materials to judge the back reflector quality. Once the quality of the ZnO materials using the reactive sputtering process was judged to be similar or better than those made using the ZnO targets, 100M lengths of back reflector material were made to demonstrate that the process can be reproducibly used over a long production level length.

Phase I of Program (Task 3)

Experimental

In the first year of the program, the reactive sputtering process was optimized in the pilot machine located at United Solar (see Figure III-1). This roll-to-roll machine is part of United Solar's decommissioned 2 MW plant and is designed to deposit BR material over a 14 in. wide web. It can be equipped with two Al targets and four ZnO or Zn targets of size 4" x 20". To optimize the backreflector deposition conditions, the pilot machine was used to deposit thick ZnO layers onto a stainless steel web previously coated with a standard Al layer and a thin ZnO layer using the 5MW production equipment. Depending on the deposition conditions, Al thin films can have different degrees of texturing which strongly affect the reflection and solar cell properties. In using the Al/thin ZnO coated web made using the 5MW production line, we were assured that the degree of texturing was similar to that obtained in production and could thus optimize the thickness and quality of the ZnO layer accordingly to that amount of texturing. The thin layer of ZnO was used to prevent oxidation of the Al surface during transportation of the web from the production machine to the pilot test machine.

To optimize the properties of the ZnO layer, a number of deposition parameters were systematically varied including the substrate temperature, the oxygen and argon flows, web speed and the applied rf power. Also compared films were made using an Al doped Zn metal target to those made using an undoped target. As a reference, ZnO layers were also made using the standard ZnO targets and the pilot machine.

To test the quality of the back reflectors, a-SiGe:H nip structures were deposited on 2" x 2" experimental back reflector coated substrates using the 13.56 MHz PECVD technique and an R&D deposition system. This system has been used to prepare 1 sq. ft. modules with world record efficiencies (>10% stable efficiencies). For each PECVD deposition, nip structures could be deposited on nine different back reflectors. In many of these depositions, high quality back reflectors with the thick ZnO layers made in United Solar's small scale R&D RADLAS system were included for comparison. The back reflectors for most of their world record solar cells and modules were made using this system. The nip structures were then coated with separate 0.25 cm^2 ITO layers for collection. The top contact was completed by depositing Al grids on top of the ITO layers.

Fig. III-1. United Solar's roll-to-roll backreflector machine. This machine is also part of United Solar's decommissioned 2 MW plant and will be used for the bulk of Task 3, and for part of Task 7.

Cells were characterized using standard IV tests and quantum efficiency measurements. The IV measurements were made using AM1.5 light or AM1.5 light filtered using a 630nm low bandpass filter. The filter simulates absorption due to the top and middle cells allowing only red light which reaches the bottom cell in the triple-junction structure. It is important to compare data obtained using the filter due to the fact that in the high efficiency triple-junction structure, the bottom cell current is the

parameter most effected by the use of the back reflector. Also using the filter eliminates any fluctuations in the blue/green light collection which is affected by a number of conditions unrelated to the back reflector including the quality of the p-layer and the ITO layer.

Results of Work Completed During Phase I of the Program

Web Handling Procedures

Initial experiments were done to determine the effect that air exposure between deposition on the Al/thin ZnO structure in the 5MW machine and placement of the coated web into the pilot machine had on the cell properties. Also the thickness of the thin ZnO layer used to eliminate Al oxide formation was determined. Three types of samples were made using the 5MW back reflector (BR) machine: 1) Al coated stainless steel, 2) same as 1) except with a thin layer of ZnO, and 3) same as 2) except the ZnO layer is twice as thick. After the 5MW deposition, samples from each of the three types were stored for one month in air or a nitrogen atmosphere. The one month exposure was to simulate the maximum time between a 5MW Al/thin ZnO deposition and our experimental ZnO depositions made using the TA2 equipment. Using United Solar's Radlus machine, we deposited thick ZnO layers on each of these types of samples after the one month of storage to complete the back reflectors. Finally, a-SiGe:H nip cells were deposited on each of the samples to test the quality of the back reflectors and to see which type of sample might be used to complete the experiments with Zn metal targets.

Table III-3 compares data for the different cells prepared using the different back reflectors. From this data, it was concluded that:

1) Use of the Al coated stainless steel without any thin ZnO coating led to poor small area cell yields and, for the most part, lower efficiencies.
2) The substrates with 40 and 80 nm ZnO stored in N_2 have the best performance in terms of the Quantum Efficiency data (Q.E.) for both the 2 day and 1 month exposure experiments.
3) The 80 nm ZnO substrate stored in N_2 has the highest Q.E. current for both the 2 day and 1 month exposure experiments.
4) The Q.E. for both the 40 and 80 nm ZnO substrates stored in N_2 are similar for both the 2 day and 1 month exposures showing that the substrates are not changing as a function of time. For all of the other substrates, the Q.E. is lower for the substrates left for 1 month compared with those left for 2 days demonstrating that the substrates are deteriorating as a function of time.

Considering these results, it was concluded that we would use Al/80 nm ZnO substrates and store them in an N_2 atmosphere prior to depositing the experimental ZnO layers prepared using the Zn metal reactive sputtering process.

Table III-3. Data for Cells Prepared Using the Different Backreflectors After Different Exposure Environments and Exposure Times.

Sample	Storage Time Before Radlus ZnO	Storage Atmosphere Before Radlus ZnO	Efficiency (mW/cm^2)	V_{oc} (V)	FF	Integrated Q.E. Current (mA/cm^2)
Std 5MW Back Reflector	-	-	2.6 2.5 2.5	0.598 0.599 0.601	0.583 0.587 0.585	7.74 7.51 7.62
5MW Al only	2 days	Air	2.2	0.572	0.472	8.10
	1 month	Air	All	Devices	Shorted	
5MW Al/ 40nm ZnO	2 days	Air	2.5	0.588	0.506	8.82
	1 month	Air	2.6	0.598	0.600	7.45
5MW Al/80nm ZnO	2 days	Air	2.5	0.575	0.526	8.79
	1 month	Air	2.6	0.611	0.559	8.01
5MW Al only	2 days	N_2	All	Devices	Shorted	
	1 month	N_2	2.5	0.570	0.546	8.28
5MW Al/ 40nm ZnO	2 days	N_2	2.7	0.585	0.531	8.76
	1 month	N_2	2.9	0.577	0.572	8.89
5MW Al/80nm ZnO	2 days	N_2	2.8	0.574	0.533	9.67
	1 month	N_2	2.8	0.579	0.562	9.44

Reactive Sputtering Optimization

During optimization of the cells made using the ZnAl(5%) metal targets and the reactive sputtering process, a number of different deposition conditions were tested. Of the deposition parameters varied, the oxygen flow had the greatest effect on the cell properties, as one might expect. In particular, the oxygen flow strongly affected the short circuit current (J_{sc}) of the cells as is shown in Figure III-2. Between oxygen flows of 40 and 70 sccm, the J_{sc} value increases by around 0.5 mA/cm^2. Further increases in the oxygen flow leads to no increase in J_{sc}. Also demonstrated in the figure is the fact that the substrate temperature has little effect on the J_{sc}. As can be seen from the data in Table III, slightly lower fill factors are obtained when the oxygen flow exceeds 90 sccm.

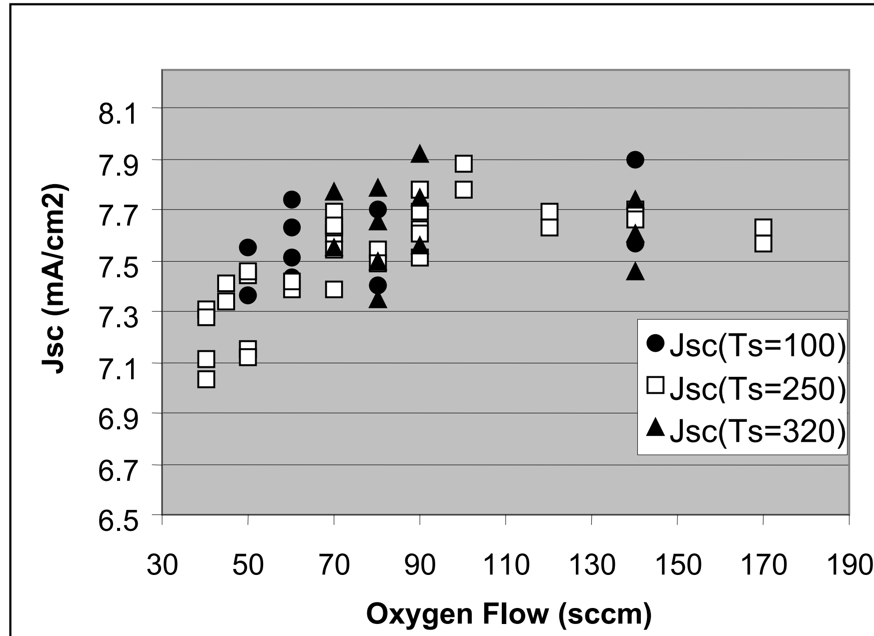

Fig. III-2. Dependence of J_{sc} for a-SiGe:H cells on oxygen flow. (Ts=substrate temperature)

Table III-4 lists cell data for a number of cells whose ZnO layers were prepared under a variety of conditions. Parameters such as the Ar flow, the target current and the substrate temperature had little effect on the cell properties as can be seen from the data listed in the table. Also in the table are data for a cell made using just the Al/thin ZnO as the back reflector adding no additional ZnO layer using the reactive sputtering process. It is clear that the properties for this cell are inferior to those for the cells made with the additional ZnO layers demonstrating that properties for the cells are affected by the added ZnO layer.

Besides using the 5% Al doped Zn target, we also fabricated cells using a 3% doped target and an undoped target in the pilot machine. Table III-5 compares cells made in the same nip deposition with back reflectors made using these three different sputtering targets. In terms of both cell properties and plasma stability, it does not matter whether the 3% or 5% Al target is used. In contrast, use of the undoped target led to poorer cell performance with the fill factors being significantly lower. In addition, optical measurements of the plasma demonstrated that the plasma with the pure metal target varied as a function of time. Specifically, the Zn plasma signal increases as does the sputtering target voltage with increased deposition time. Use of higher oxygen flows improves the plasma stability, however the plasma can not maintain the stability achieved with the doped targets. It is not yet known whether the lower FF are associated with these plasma instabilities, however it is clear that use of the doped targets does lead to a more manageable process.

Table III-4. Data for a-SiGe:H Cells Prepared with Backreflectors Made Using Reactive Sputtering Technique Under a Variety of Deposition Conditions.

Substr. Temp. (°C)	O_2 Flow (sccm)	Ar Flow (sccm)	Target Current (amps)	V_{oc} (V)	J_{sc} (mA/cm^2)	FF	R_s (Ωcm^2)	P_{max} (mW/cm^2)
250	40	30	8	0.723	7.11	0.684	11.9	3.5
250	40	30	8	0.725	7.31	0.685	11.9	3.6
250	45	30	8	0.723	7.34	0.684	11.6	3.6
250	50	30	8	0.726	7.12	0.676	11.6	3.5
250	70	30	8	0.726	7.54	0.675	12.0	3.7
250	90	30	8	0.730	7.78	0.681	12.7	3.9
250	100	30	8	0.728	7.78	0.664	12.9	3.8
250	120	30	8	0.723	7.69	0.669	11.2	3.7
100	70	30	8	0.726	7.61	0.679	11.5	3.7
250	70	30	8	0.729	7.69	0.676	10.9	3.8
320	70	30	8	0.734	7.77	0.671	12.1	3.8
320	70	30	6	0.724	7.79	0.671	13.9	3.8
320	70	30	8	0.734	7.77	0.671	12.1	3.8
320	70	30	10	0.728	7.65	0.674	14.0	3.8
250	90	10	8	0.726	7.78	0.674	12.7	3.8
250	90	30	8	0.729	7.78	0.681	12.7	3.9
250	90	50	8	0.732	7.69	0.678	11.2	3.8
No Added	ZnO layer	- Only	Al/thin ZnO	0.701	6.86	0.683	11.5	3.3

Table III-5. Data for a-SiGe:H Cells Whose Backreflectors were Made Using Targets with Different Al Contents.

Target Material	V_{oc} (V)	J_{sc} (mA/cm^2)	FF	R_s (Ωcm^2)	P_{max} (mW/cm^2)
ZnAl (5%)	0.715	7.83	0.667	11.5	3.7
ZnAl (3%)	0.718	7.76	0.676	12.1	3.8
Zn	0.712	7.81	0.643	16.2	3.6

To truly judge the quality of the back reflectors made using the new reactive sputtering process, single-junction a-SiGe:H cells were made using three different types of back reflector listed below:

1) back reflectors made in the pilot machine under the optimized conditions using the experimental reactive sputtering process and the ZnAl(5%) sputtering targets,
2) back reflectors made in the pilot machine under the optimized conditions using the standard sputtering process and ZnO targets,
3) back reflectors made in the 5MW production machine using the standard sputtering process and ZnO targets.

Again, the nip structures for all three types of back reflectors were made in the same deposition run using United Solar's 1 sq. ft. R&D deposition system. The data for the three types of cells are listed in Table III-6. Comparing data for the cells made using the back reflectors from the pilot machine, the cell properties for the cells made using the ZnAl (5%) targets are similar to those for the cells made using the ZnO targets demonstrating that the new reactive sputtering process can be used to prepare high quality back reflector material.

Table III-6. Data for a-SiGe:H Cells Whose Backreflectors were Made with the Reactive Sputtering Process Using Zn Metal Targets and the Standard Process Using ZnO Targets.

Target Material	BR Machine	V_{oc} (V)	J_{sc} (mA/cm^2)	FF	Rs	P_{max} (mW/cm^2)
ZnAl(5%)	Pilot Machine	0.731	7.57	0.668	10.7	3.7
ZnO	Pilot Machine	0.731	7.49	0.665	12.0	3.6
ZnO	5MWProduction	0.730	7.42	0.662	13.2	3.6

As a final comparison of the back reflectors made with the Zn metal and ZnO targets, we have fabricated larger area (44.5 cm^2) single-junction a-SiGe:H cells using the two types of back reflectors. The nip structures for the two cells were prepared in the same deposition run in order to minimize the differences from layers other than the ZnO materials. Table III-7 displays data for these two types of cells. The slight differences in the properties for the two cells are within experimental error again demonstrating that the inexpensive ZnAl(5%) targets can be used to prepare high quality back reflector material. These cells fulfill the required deliverable D-1.4.9.

Table III-7. Data for 44.5 cm^2 Modules Made with Different Backreflectors.

Target Material	BR Machine	J_{sc}(QE) (mA/cm^2)	V_{oc} (V)	FF	R_s (Ω/cm^2)	Efficiency (%)
ZnAl(5%)	2 MW Pilot	18.9	0.77	0.631	0.20	9.18
ZnO	5MW Production	18.5	0.77	0.649	0.18	9.24

Phase II of the Program (Task 7)

Experimental

During this phase of the program, the new reactive sputtering process was tested using the 5MW line. To initially optimize the deposition conditions for the reactive sputtering process in the 5MW back reflector line, a web was coated with several experimental back reflectors prepared under a variety of conditions. To test the quality of the back reflectors, a-SiGe:H nip structures were deposited on 2" x 2" experimental back reflector coated substrates cut from the web. The semiconductor layers were made using the

13.56 MHz PECVD technique and an R&D deposition system. This system has been used to prepare 1 sq. ft. modules with world record efficiencies (>10% stable efficiencies) and was used in Phase I to prepare the cells whose data is listed in Table III-7. For each PECVD deposition, nip structures could be deposited on nine different back reflectors. In many of these depositions, high quality back reflectors with the 5MW equipment and the standard sputtering technique (ceramic ZnO targets) were included for comparison. The nip structures were then coated with separate 0.25 cm^2 ITO layers for collection. The top contact was completed by depositing Al grids on top of the ITO layers.

After initial optimization of the reactive sputtering fabrication conditions, QA/QC coupons were made using the reactive sputtering process to prepare the ZnO layers. For these coupons, all of the layers (back reflector, semiconductor, top contact) were made using the 5MW production equipment. Triple-junction cells were deposited on each of the test back reflector layers. Each coupon contained fourteen 9.7 cm^2 cells for judging the device quality over the entire coupon area.

Cells were characterized using standard IV tests and quantum efficiency measurements. The IV measurements for the a-SiGe:H cells were made using AM1.5 light or AM1.5 light filtered using a 610nm low bandpass filter. The filter simulates absorption due to the top and middle cells allowing only red light which reaches the bottom cell in the triple-junction structure. It is important to compare data obtained using the filter due to the fact that in the high efficiency triple-junction structure, the bottom cell current is the parameter most effected by the use of the back reflector. Also using the filter eliminates any fluctuations in the blue/green light collection which is affected by a number of conditions unrelated to the back reflector including the quality of the p-layer and the ITO layer. The triple-junction cells on the QA/QC coupons were characterized using only the unfiltered light.

Hardware Changes to the 5MW line for implementation of the new process

Prior to optimization of the thin film deposition conditions in the 5MW production line, three hardware changes were required to implement the reactive sputtering process:

1) Changing of the pump seals for oxygen use,
2) Addition of oxygen gas line,
3) Alteration of cathode hardware for new target design.

The pumps were not fitted with oxygen compatible vacuum seals and thus a mechanical pump and blower had to be sent to the manufacturer for seal changes. The entire process that included sending the pumps, seal replacement and the return of the pumps took 3 months. The oxygen gas line was connected to the gas manifold in which Argon sputtering gas was supplied to the region of the sputtering target.

Use of a metal target allowed for the elimination of Cu backing plates (to which ceramic target like ZnO are typically bonded to). With a moderate change in the sputtering target, we were able to develop a more convenient target design which did not require the breaking a vacuum and water lines for each target change, two actions which were

required for changing ZnO targets. To implement this new target design, some changes to the shielding around the targets were required. A report describing the hardware changes to the production machine for the implementation of the reactive sputtering process was submitted as a deliverable for the program (D-2.4.7).

Results from Phase II 5MW experiments

In Table III-8, average data for cells made using the standard 5MW back reflector presently used in production is compared to average data for cells made using the reactive sputtering process and the 5MW back reflector deposition equipment. These 0.25 cm^2 cells were prepared using the R&D machines to prepare the semiconductor and top contact layers. The data in the table was obtained using AM1.5 light filtered with a 630nm cutoff filter which only allows red light with wavelengths greater than 630nm to reach the cells. Use of the reactive sputtering process has led to the fabrication of cells with significantly higher short circuit currents but slightly lower open circuit voltages and fill factors. This combination of properties led to cells with similar efficiencies to those prepared using the standard back reflector. These results demonstrated that the reactive sputtering process could be used in the 5MW back reflector production line to prepare high quality back reflectors and bottom cells.

Table III-8.
Date for 0.25cm^2 Cells with Reactive and Standard BR Processes.

Back Reflector Type	Pmax (mW/cm^2)	J_{sc} (QE) (mA/cm^2)	V_{oc} (V)	FF	Rs (ohm cm^2)
Zn Metal - Reactive Sputtering Process	3.5	10.0	0.58	0.60	11.5
Standard ZnO Production Process	3.5	9.3	0.59	0.63	11.0

Using the same thin film fabrication process, two 45 cm^2 cells were made, one with the new reactive sputtering process and the other with the standard process using ZnO with the cell properties shown in Table III-9. The cell efficiencies for the cells made using the two back reflectors are similar, achieving the milestone m-2.3.3. These cells were sent to NREL fulfilling the deliverable D-2.3.3.

Table III-9.
45cm^2 Modules PVMAT Deliverables for Reactive Sputtered ZnO (5-15-00)

ZnO	Serial #	Area (cm^2)	Temp. (^0C)	V_{oc} (V)	I_{sc} (A)	FF	P_{max} (W)	V_{mp} (V)	R_s (Ω)	R_{sh} (Ω)	Eff. (%)
Sputt. ZnO	7222E1	44.8	21.2	0.641	0.951	0.615	0.375	0.480	0.15	8.3	8.4
	7222F2	44.8	21.2	0.647	0.951	0.620	0.381	0.469	0.15	6.7	8.5
Average		**44.8**	**21.2**	**0.644**	**0.951**	**0.617**	**0.378**	**0.475**	**0.15**	**7.5**	**8.4**
Sputt. Zn	7226E3	44.8	21.7	0.647	0.968	0.610	0.382	0.479	0.15	6.9	8.5
	7226G2	44.8	21.2	0.641	0.968	0.614	0.381	0.476	0.14	7.9	8.5
Average		**44.8**	**21.5**	**0.644**	**0.968**	**0.612**	**0.381**	**0.477**	**0.15**	**7.4**	**8.5**

As previously mentioned, cells were also made using the new reactive sputtering process and the 5MW equipment in ALL of the fabrication steps. That is, the back

reflector, semiconductor and ITO top contact layers were all prepared using the 5MW line as is done for the modules to be sold. On the same roll of stainless steel, cells were made using the standard 5MW back reflector fabrication process and using the new reactive sputtering method for final comparison. From this roll, QA/QC coupons standardly used for qualifying the production material were fabricated. Listed in Table III-10 are the average cell properties (14 cells per coupon) for two coupons made using the standard back reflector fabrication process and those for two coupons made using the new reactive sputtering process. One can see that the cell properties are independent of the sputtering process used. The coupons whose data are listed in the table were sent to NREL as the deliverable D-2.4.6. With completion of this work, all of goals set for Task 3 and 7 of the program were met.

Table III-10.
Data for QA/QC Coupons Made Using Different ZnO Processes.

Coupon	ZnO Sputtering Process	J_{sc} (mA/cm^2)	V_{oc} (V)	FF	R_s (Ohm-cm^2)	P_{max} (mW/cm^2)
1200	Reactive	6.86	2.13	0.672	37.2	9.81
1275	Reactive	6.91	2.13	0.670	37.1	9.85
1575	Standard	6.85	2.13	0.673	36.1	9.80
1625	Standard	6.84	2.13	0.675	36.0	9.82

The proof of success of this portion of the program is the planned use of this new reactive sputtering deposition process in United Solar's 25MW line for ZnO preparation.

IV. TASKS 4,8,11 - CATHODE HARDWARE STUDIES FOR A-SI(GE):H I-LAYER DEPOSITIONS

Summary

In this part of the program, we developed new internal hardware for the i-layer deposition chambers used in United Solar's 5MW production line to improve the quality and uniformity of these materials and to increase the overall solar cell and machine efficiencies. Three newly designed cathodes were built, tested and compared with the 5MW design during this three-year program.

Using a single chamber system and the substrate in a static mode, two cathode designs (1st and 2nd generation hardware) were developed that led to significant improvements in the uniformity of the film thickness across the web as compared with films made using the standard 5MW cathode hardware. The good uniformity was observed even when high deposition rates were used, a regime where large area uniform deposition can be difficult. However for both the 1st and 2nd generation hardware, the performance of the cells made using these two different cathode hardware designs did not match the performance of those made using the standard cathode hardware used in the 5MW production machine. The poorer performance of the cells made using the 2nd generation hardware became apparent when moving web conditions were used.

A 3rd generation hardware was then developed which not only allowed for good thickness uniformity over a wide range of deposition parameters but also improved cell performance. Table IV-1 shows data for a-Si:H cells made using the 2nd and 3rd generation hardwares as well for the 5MW style hardware. With the 3rd generation hardware, we were able to achieve the goals of a 6% increase in cell performance over cells made using the 5MW hardware and a ± 5% thickness uniformity across 80% of the cathode area. This good performance was demonstrated over a 100m length of web.

Table IV-1.
Comparison of performance of cells produced in the 2nd and 3rd generation hardware to cells produced in the 5 MW style hardware.

Cathode	V_{oc} (V)	J_{sc} (mA/cm^2)	FF	R_s (ohm cm^2)	P_{max} (mW/cm^2)
2nd generation	0.947	7.2	0.727	9.7	4.96
3rd generation (8/00)	0.980	7.86	0.753	8.1	5.80
3rd generation (8/01)	0.975	8.30	0.739	8.2	5.98
5MW	0.968	7.90	0.724	8.1	5.60

The 3rd generation hardware was also used to make a-SiGe:H cells. It was found that the cell performance was not dependent on the Si source gas used and that use of either SiH_4 or Si_2H_6 led to the fabrication of cells with similar good performance. Thus with this 3rd generation design, inexpensive SiH_4 can replace Si_2H_6 as the Si source gas for making a-SiGe:H alloys in the production machine.

To test the long term use of the 3rd generation hardware, a set of this hardware was installed in the 5MW production line. As of 9/01, the hardware has been used in a chamber for a-Si:H deposits for over 9 months with no significant problems. With the success of this part of the program, a version of the 3rd generation cathode hardware will be implemented in United Solar's new 25MW line.

Background

Efficiencies for small area a-Si:H based devices are being steadily increased; the present world record is 13% stable efficiency for a small area triple-junction cell (0.25 cm^2 active area) produced in a small scale reactor (4" x 4" maximum deposition area) by United Solar. This accelerating improvement suggests that even higher efficiencies should be obtainable. However, the efficiencies obtained for large area solar modules are still significantly lower than the 13% values being near 8-9%. The lower module efficiencies are due in part to back end processes such as lamination and module designs. However, even the small area cells fabricated in the large area, continuous roll-to-roll machines (in particular the 5 MW machine) have yet to demonstrate efficiencies that match the world record values even though thorough optimization studies have been carried out. This suggests that there are inherent problems with the present large area process and/or hardware designs that limit the efficiencies to their present day values.

One problem which is more difficult to achieve in the present large area production machines as compared with the smaller R&D machines is the ability to prepare reasonably uniform film depositions across the entire cathode area during PECVD depositions. This problem was of major concern during our optimization program for the 5 MW production machine. For example, a-SiGe:H i-layer depositions, in order to obtain relatively uniform film depositions across the length of the cathodes for each vacuum chamber, we were limited to work in a small area of deposition parameter space. If parameters outside this space were used, gradients across the length of the cathode were obtained for the Ge content as well as for the deposition rate as is shown in Figure IV-1. It was found that these non-uniformities were not related to unequal power distributions across the cathode or gas depletion, as one might expect. With a moving web substrate, this affect lead to cells and modules which had significant variations in the Ge content through the depth profile of the a-SiGe:H i-layers. Variations in the bandgap of the materials obviously accompanied the Ge content fluctuations that likely formed shallow carrier traps in the i-layers limiting the carrier collection and cell efficiencies. Also, since the quality of a-Si:H based materials prepared by the PECVD method depend strongly on the film deposition rates, the

variations in the deposition rates led to the formation of high quality material in the region of the cathode where the deposition rates were low and poorer quality material in the region where the deposition rates were high. Under these conditions, the overall film and device performance was limited by the poor material produced in the high deposition rate region. If the overall deposition rate were lowered in order to improve the material produced in the high deposition rate region, the machine throughput was unacceptably low.

We should note that similar variations in the deposition rates across the lengths of the cathode were also observed for a-Si:H layers. Thus the non-uniformity problem was not related to differences in the decomposition rates of Si and Ge source gases but instead is inherent to the existing vacuum hardware design.

When limited to a small region of parameter space, the efficiencies are likely limited to low values. With a different internal hardware design that allows for uniform depositions across a large area of parameter space, the maximum efficiency would likely be outside the small area of parameter space we are presently restricted to. Thus, if such a deposition hardware design could be devised, higher cell and module efficiencies would likely be obtained.

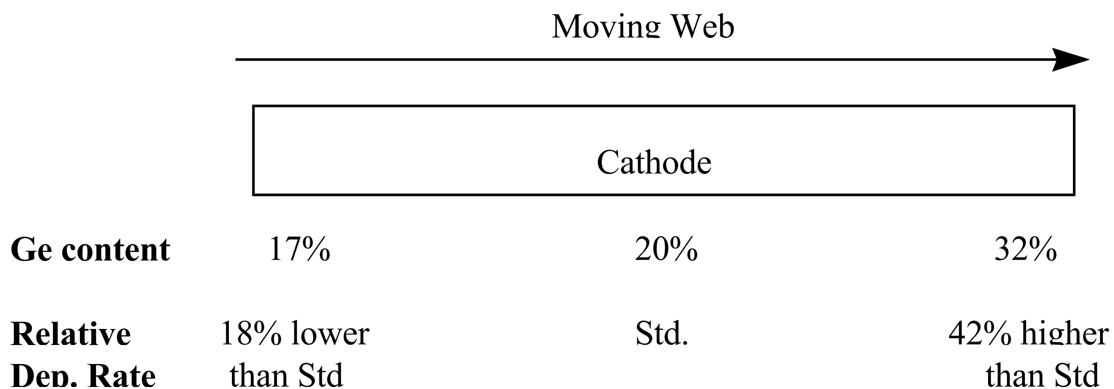

Fig. IV-1. Variation of Ge content and deposition rate across cathode.

In attempting to achieve the record high efficiencies using the large machines, one must be assured that the film growth conditions used to prepare the large modules are similar to those obtained using the small area machines. In particular, the plasma chemistry, electrical potentials and film surface growth conditions must be duplicated in order to prepare the proper film quality and film microstructure. Specifically, a deposition system which comes close to replicating the plasma densities for all of the Si based radicals and H atoms in the plasma, the substrate self bias and the plasma potential, and the electron and ion bombardment of the growth surface must be designed. Only when this is done will one have the potential of achieving the high efficiencies with the large area systems. While the present internal hardware design for the 5MW chambers is not dramatically different from the design for the small scale systems used to prepare the high efficiency cells, a design for the large area chamber internal hardware which more accurately reproduces the small scale geometry might lead to higher large area cell efficiencies.

Objective of Cathode Hardware Studies

In this program, we developed new internal hardware for the i-layer deposition chambers used in United Solar's 5MW production line to improve the quality and uniformity of these materials and to increase the overall solar cell and machine efficiencies. Three newly designed cathodes were built, tested and compared with the 5MW design during this three-year program. To judge the usefulness of each design, single-layers were made first to test the ability to obtain uniform deposits over large areas and large regions of deposition parameter space while single-junction a-Si:H cells were later fabricated to test the quality of the deposited layers. Most of the designs were first tested in a single chamber system with a static substrate.

Once final designs for the internal hardware were completed, the desired hardware was incorporated into an existing chamber on the 2 MW pilot semiconductor line at United Solar (see Figure IV-2). To test this new internal hardware, single-junction nip a-Si:H and a-SiGe:H cells were prepared using the new hardware on a moving web substrate. The i-layer conditions were optimized for the highest FF for cells with similar J_{sc} values. Improvements in the hardware were judged by increased FF for the cells and improved deposition uniformity over those obtained with the 5MW style cathodes. If necessary, alterations to the system hardware were made so that the plasma and growth conditions more closely match those for the small area R&D system. Also, temperature, gas flow and pressure distributions throughout the chamber were closely monitored. With demonstration that a new improved design could be developed, it would be applied in the new 25MW production line.

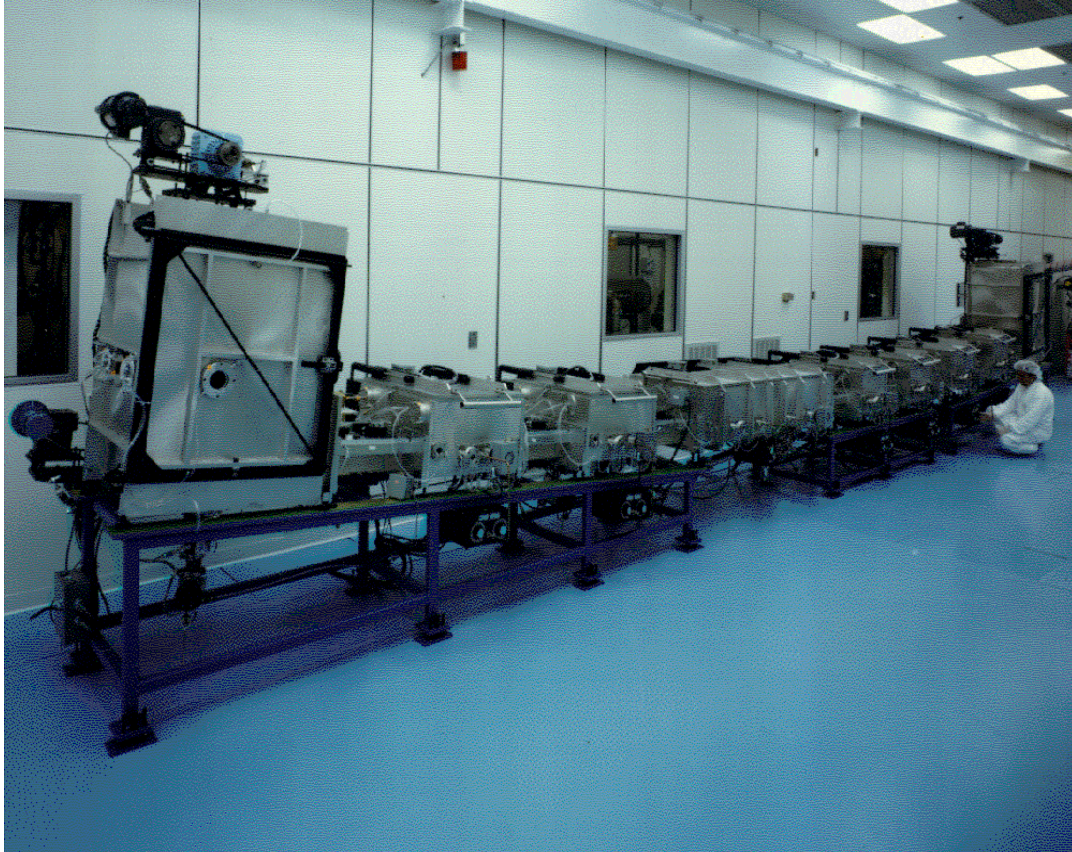

Fig. IV-2. Double-junction roll-to-roll plasma-CVD processor, previously used as United Solar's production machine. This machine was used as an experimental machine for much of the work proposed in Tasks 8 and 11.

The pilot roll-to-roll PECVD processor was previously used as a solar cell production machine when United Solar's production plant had a capacity of 2 MW. It is capable of making nipnip tandem solar cell structures on a 14" web.

Also to gain some understanding of the deposition processes, a segment of computer simulations of the plasma kinetics and chemistry was completed. The results of these studies will be useful in considering future hardware designs.

Experimental

The research studies were divided into five sections:

1) Static testing of new cathode hardware
2) Roll-to-roll testing of new cathode hardware
3) New cathode hardware testing in the 5MW line
4) New cathode hardware testing for the 25MW line
5) Modeling of the a-Si:H deposition

The static tests were completed in Phases I and II, the roll-to-roll testing done in Phases II and III and the modeling carried out in Phase I. Two new styles of cathode hardware (1st and 2nd generation hardware) and cathode hardware which was nominally the same as that used in the 5MW line were tested in the static mode. The new designs incorporated several ideas that were devised during the 5MW machine optimization program, during which a great deal of knowledge was obtained. Further studies of the 5MW cathode design in this program has also proved beneficial towards the development of this new hardware. Incorporation of several improvements should lead to better control of the gas flow, temperature distribution and film uniformity across the cathode and deposition area.

The initial static tests of the cathodes were completed using a single test deposition chamber (see Figure IV-3) in which two different styles of cathodes were simultaneously compared in the same environment. During this first year, we designed, built and compared one new cathode design with a cathode that mimics the design used in 5MW production machine. In the same system pump-down, single layer films to test deposition uniformity and/or i-layers for nip solar cells to test i-layer quality were made from both types of cathodes. In the second year, the second cathode was tested along side the cathode which was nominally the same as those used in the 5MW line.

Typically, the same deposition conditions were used for both deposits including the same rf power density. For the single layer deposits on bare stainless steel substrates, film thickness across the deposition area was measured using standard optical techniques. The 13.56 MHz Plasma Enhanced Chemical Vapor Deposition (PECVD) technique was used to deposit all of the materials.

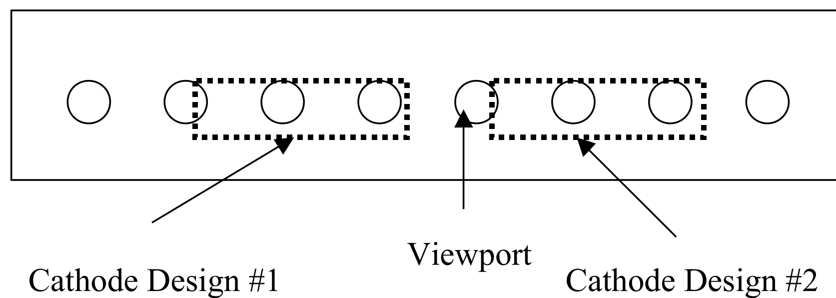

Fig. IV-3. Single chamber system used for cathode development.

To fabricate 0.25 cm^2 a-Si:H single-junction test cells, the cathode hardware to be tested was only used to prepare the i-layer materials. Preparation of both the intrinsic layer and the doped layers in a single chamber system is not desirable because of the cross contamination effects which hinder electron and hole collection in the cell. Therefore to make the cells for this study using the single chamber system, we made the n- and p-layers by the PECVD method in a separate, proven load lock R&D system. This system has prepared high efficiency triple-junction devices in the past and is presently used to make high efficiency single junction cells. The steps used to prepare each of the devices were as follows:

1) deposit an a-Si:H:P n-layer using the load lock system,
2) quickly transport the n-layer coated substrates to the single chamber system attempting to minimize air exposure,
3) deposit i-layers using the two different cathode designs,
4) quickly transport the n/i coated substrates from the single chamber system to the load lock system again attempting to minimize air exposure,
5) deposit an a-Si:H:B p-layer using the load lock system,
6) deposit ITO/Al contacts using standard evaporation techniques.

Such a device is depicted in Figure IV-4. For these studies, the cells were made without current enhancing Ag/ZnO backreflectors to minimize the complexity of the cells.

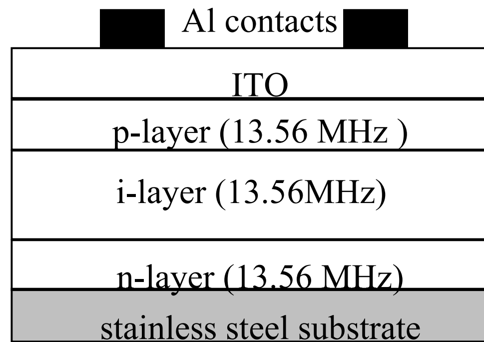

Fig. IV-4. a-Si:H single-junction cell structure.

In the pilot machine, all three semiconductor layers (n-, i- and p-layers) were deposited in the roll-to-roll process. Again, the layers were deposited on bare stainless steel substrates. ITO contacts were deposited using a dc sputtering technique and a 1 sq. ft. R&D machine while Al contacts were evaporated onto the ITO using a small scale reactor. Two new cathodes were tested along side the 5MW style cathode.

To characterize the devices, current vs. voltage (IV) measurements were made to obtain standard solar cell device parameters (short circuit current (J_{sc}), Fill Factor (FF), Open Circuit Voltage (V_{oc}), etc.). Also, quantum efficiency measurements were also used to obtain integrated currents and determine collection losses in cell. After initial cell measurements, the devices were subjected to light soaking periods. We first light soaked the samples for 10 and 30 hrs. under AM1.5 light at 50 °C, after each of these periods the cell properties were measured. To measure the stable efficiencies, one must light soak them for 600 hrs. But to get preliminary data on how the deposition parameters are affecting the amount of degradation, we made these limited light exposure measurements to optimize the deposition conditions for minimum degradation and optimum stable cell efficiencies. After initial screen testing, we selected certain cells for long term light exposures to obtain accurate values for the stable efficiencies.

Results

Static tests in the Single R&D Chamber

Testing Similarity to Cathodes Used in Production (5MW Style Cathode)

Initially, several depositions were completed to verify that the 5MW style cathode in the single R&D cathode testing chamber behaved similar to the cathodes in the 5MW production machine. In particular, we were testing to see if the non-uniform deposits across the length of the cathode would be obtained at the production level deposition rates. Figure IV-5 compares deposition rate profiles across the length of the cathode obtained using different deposition conditions and the 5MW style cathode. These profiles were taken near the center of the deposit and the cathode as is shown in Figure IV-6. In Figure IV-5, we compare profiles taken at different applied power levels that led to different deposition rates while all other deposition parameters were nominally fixed. The average deposition rates in Å/s for each profile is listed in the figure legend in brackets. As is the case for the production line cathodes, as the power level is increased, the film thickness, and thus the deposition rate, near the gas inlet becomes much larger than the thicknesses obtained near the pump out port. This variation in deposition rate across the cathode length is partially due to a gas depletion effect but can not be the only cause due to the fact that there is not a drop in deposition rate near the pump out side of the cathode as the power is increased. This trend of poorer uniformity with increased power was the same effect observed during the optimization of the 5MW production line.

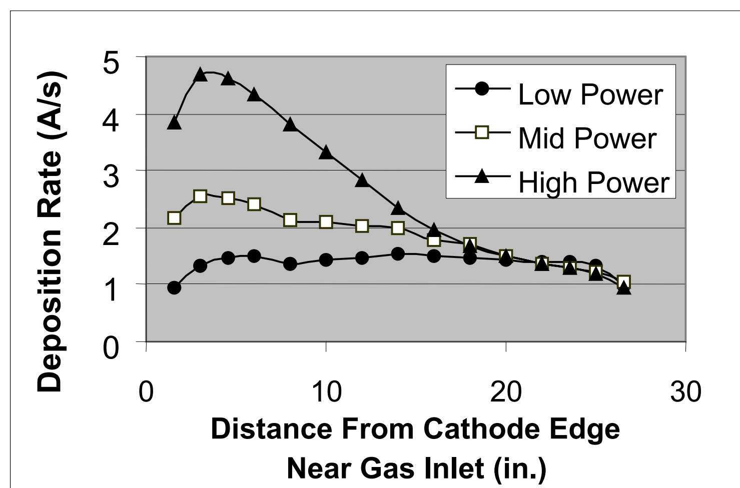

Fig. IV-5. Thickness profiles for films made at different applied rf powers.

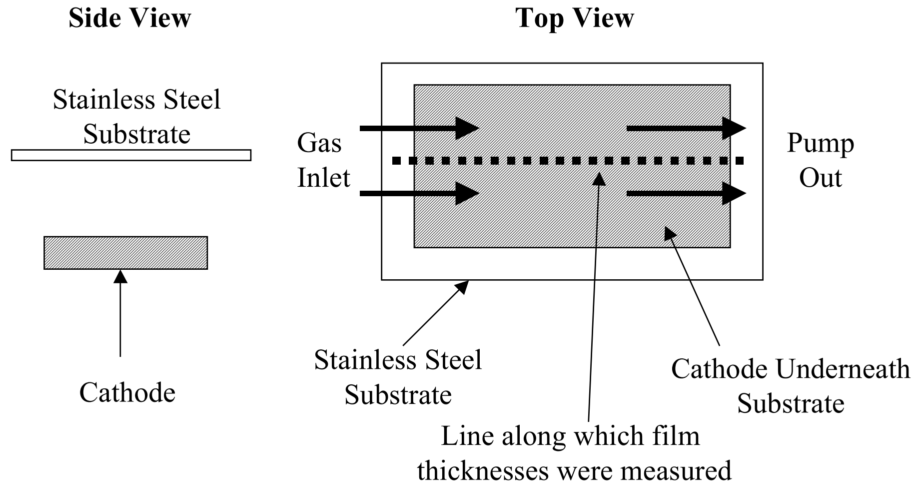

Fig. IV-6. Orientation of film thickness measurements.

In these studies, it became obvious that the uniformity of the deposit across the cathode length was primarily dictated by the applied power level as it was for the cathodes in the production line. Figure IV-7 displays the degree of uniformity across the length of the cathode as a function of deposition rate. As a figure of merit for the film uniformity, the y axis in this figure denotes the difference between the maximum and minimum deposition rates obtained across the length across the cathode divided the average deposition rate for the deposit. The differences in applied power are denoted by the different icons. As can be seen from the figure, at each fixed power level, the degree of uniformity remains relatively unchanged while other deposition parameters including the hydrogen flow, the active gas flow (silane), and the substrate temperature were altered changing the deposition rate. In contrast, the uniformity becomes poorer with increased power.

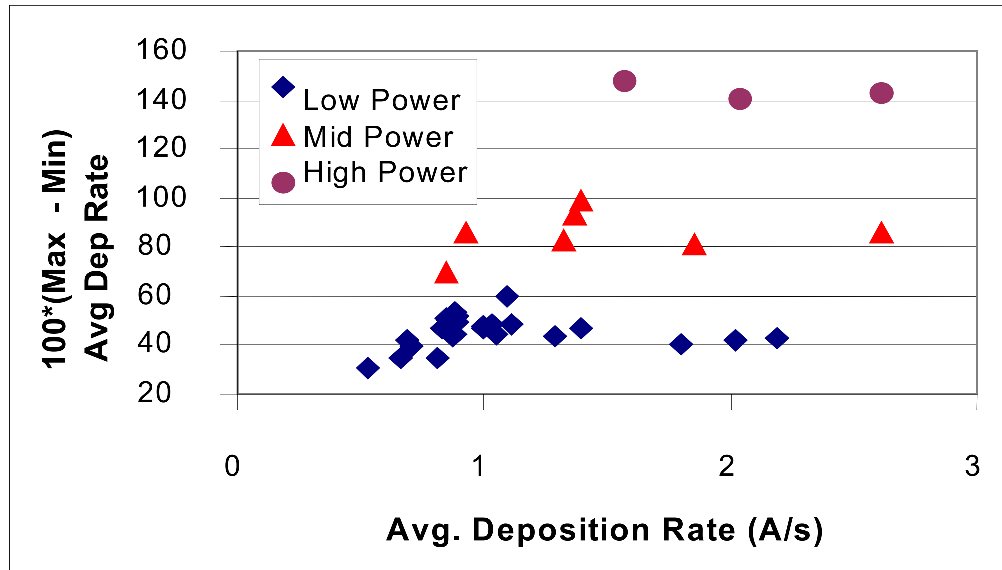

Fig. IV-7. Variation of deposition uniformity over length of cathode as a function of deposition rate.

From the data in Figure IV-7, one can observe that fairly uniform deposits and relatively high deposition rates (greater than 2 Å/s) can be obtained at low power levels (80-120W). However to achieve these rates, low hydrogen dilution levels and high silane flows had to be used which led to polysilicon powder formation on the cathode leading to poor cell performance. This is shown in Table IV-2 where data for a-Si:H cells whose i-layers were made at the same rates but different applied powers are compared. The cell whose i-layer was made using the low power and less hydrogen dilution has significantly poorer FF and solar cell efficiency (P_{max}). Thus the poor cell performance eliminates the possibility of using the low power/low dilution conditions to obtain good deposition uniformity.

Table IV-2. Data for a-Si:H cells made at different applied powers but similar i-layer deposition rates.

Power (W)	i-layer Dep. Rate (Å/s)	V_{oc} (V)	J_{sc} (mA/cm^2)	FF	R_s (Ωcm^2)	P_{max} (mW/cm^2)
120	1.80	0.949	10.93	0.577	16.7	5.99
180	1.85	0.928	10.61	0.659	9.9	6.49

From the these results, it was clear us that in terms of deposition uniformity across the length of the cathode, this cathode behaves similarly to the cathodes in production in that at increased deposition rates, the deposits are either non-uniform or of poor quality.

Attempts to Improve Uniformity Using 5 MW Style Cathode

In an attempt to better understand the causes for the non-uniform deposits at high rates, slight alterations to the 5MW cathode design were studied. In one case, we altered the pumping manifold to see if the pumping geometry would strongly affect the deposition uniformity. In particular, it was thought that the uniformity across the width of the substrate (cathode) could be improved through a slight alteration of the gas flow pattern. After four alterations to the pumping manifold, no significant change in the uniformity was observed.

In terms of the uniformity across the width, it was also discovered in these studies that excess hydrogen gas from a source outside the cathode hardware and gas manifold, such as from our proprietary gate gates, does significantly affect the deposition uniformity. This is demonstrated by the data shown in Figure IV-8 where the deposition rate profiles across the width of the cathode is shown for different outside gas flows. Comparing the profile when hydrogen gas flowed with the profile when no outside gas flowed, there is a significant drop off in the deposition rate and thus the film thickness at the edge of the web when hydrogen gas flowed. The thinner films lead to lower efficiencies for the subcells on the edges of the film and for the 12" wide modules. However, by adding a small amount of silane to the outside hydrogen gas flow, one can once again obtain the desired uniformity across the web as is shown in the figure.

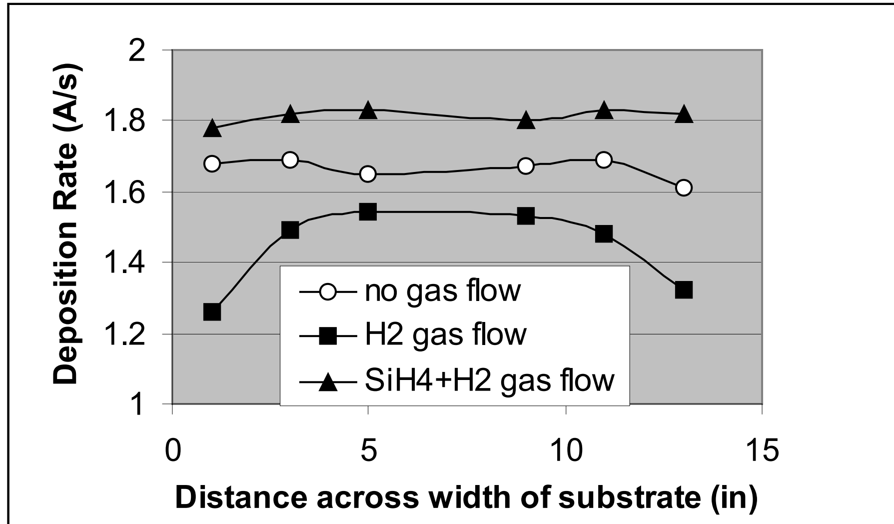

Fig. IV-8. Uniformity across width of web (cathode) from deposits made using different gas flows from outside cathode and gas manifold hardware.

Use of pulsed rf plasmas was also tested as a method to improve the deposition uniformity across the length of the cathode. It was thought that by using short, high decomposition rate pulses, one would minimize radical interaction that may be a chief cause for the non-uniform deposits at high rates. Several experiments were completed using different duty cycles, pulse widths, and no-pulse power levels. In each case, more uniform deposits but lower deposition rates were obtained when the pulsed plasma was used instead of the continuous constant power conditions. Also, powder formed on the cathode each time a pulsed plasma was used leading to lower cell efficiencies. The source of this powder is not yet understood. Alteration of the gas flows and applied powers to match the deposition rates obtained using the continuous power conditions led to increased powder formation. Thus, use of pulsed power is not the answer to obtaining uniform deposits and we have still yet to find a method to obtain uniform deposits across the length of the cathode using the 5MW production hardware.

Static Testing of 1st Generation New Cathode Design in the Single Chamber

The 1st generation new cathode design was thoroughly tested in the single chamber cathode testing system along with the 5MW style cathode. For each system pump down, separate deposits were made using both cathodes under similar gas flow conditions, substrate and cathode temperatures, power densities and chamber pressures. This new cathode has several features which mimic those for cathodes used in R&D which produce cells of high efficiencies. In particular, this new cathode differs from the 5MW style cathode in terms of gas flow pattern and electrical potentials obtained during deposition, including the substrate self bias.

A number of deposits were made using both types of cathodes with the following deposition conditions varied; the substrate temperature, the cathode temperature, the applied rf power, and the silane and hydrogen gas flows. For each deposit, a large substrate was used for characterization of the deposition uniformity while 2”x2” n-layer coated substrates were also included for cell preparation and judgment of the i-layer quality.

It was found that with this new design, one could obtain uniform deposits (±8%) over the entire cathode area at a wide range of deposition rates (1-5 Å/s) using a number of different deposition conditions. Figure IV-9 displays uniformity profiles across the center of the cathode hardware for typical low rate and high rate deposition conditions. One should note that the new cathode is roughly half as long as the 5MW cathode design. However, our engineers and scientists have determined prior to the construction of this cathode that because of the cathode’s unique design, expansion of the cathode to twice it’s present size will not cause a significant alteration of the deposition profile. The ability to obtain good uniformity over this relatively wide range of deposition rates is likely associated with the different gas distribution system from the 5MW cathode design. This is a significant improvement over the production style cathode.

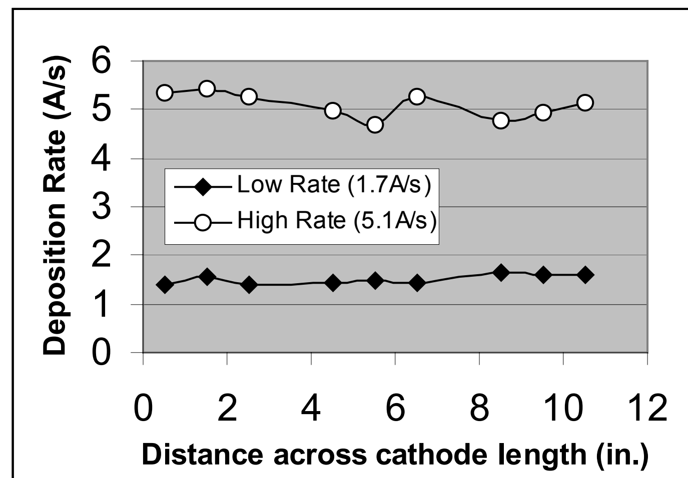

Fig. IV-9. Deposition rate profiles across new cathode at different deposition rates.

In terms of i-layer quality, a number of cells were made as can be seen from the data shown in Figures IV-10 and IV-11. In the figures, the fill factor (FF) and maximum power (P_{max}), or cell efficiency, are plotted as a function of short circuit current. Both the fill factor and the cell efficiency depend strongly on the i-layer thickness. For these a-Si:H cells, the short circuit current depends almost linearly with film thickness in the range of J_{sc} studied. Thus, the figures roughly contain the trends of FF and P_{max} with i-layer thickness. To compare cells in this case i-layer quality, one should compare cells with the same i-layer quality and thus the same J_{sc} value. Of course during optimization of the deposition conditions, most of the cells were not made under the optimal conditions (the solid circles in the figures). For both types of cathodes, it was determined that i-layers made with high hydrogen dilution of the plasma and a substrate

temperature of 225 ºC had, on average, the best cell properties. In the figures, the data for these cells are denoted by open triangles and open circles for the new and 5MW style cathodes, respectively. Under these conditions, the cells made using the new cathode had on average significantly poorer performance than the cells made using the standard 5MW cathode due to lower FF. This can be seen more clearly from the data shown in Table IV-3 where values for cells with similar i-layer thicknesses made under the optimal conditions are compared. The disparity in cell performance becomes even larger as the deposition rate is increased.

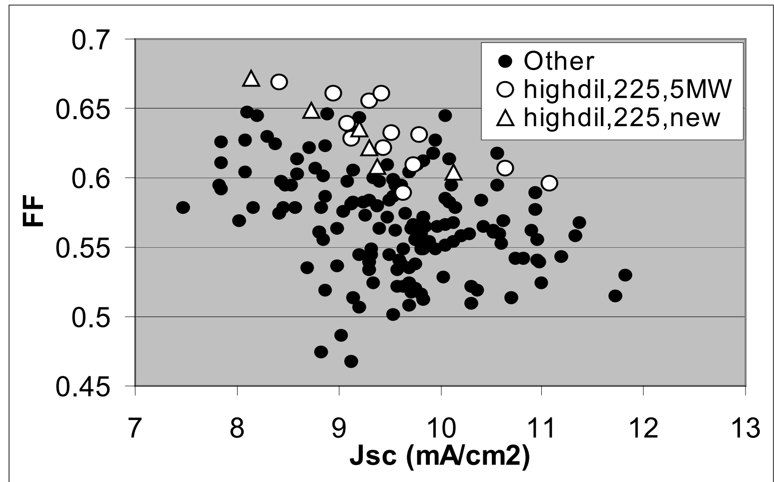

Fig. IV-10. Plot of fill factor versus short circuit current for cells made using the new and 5 MW style cathodes.

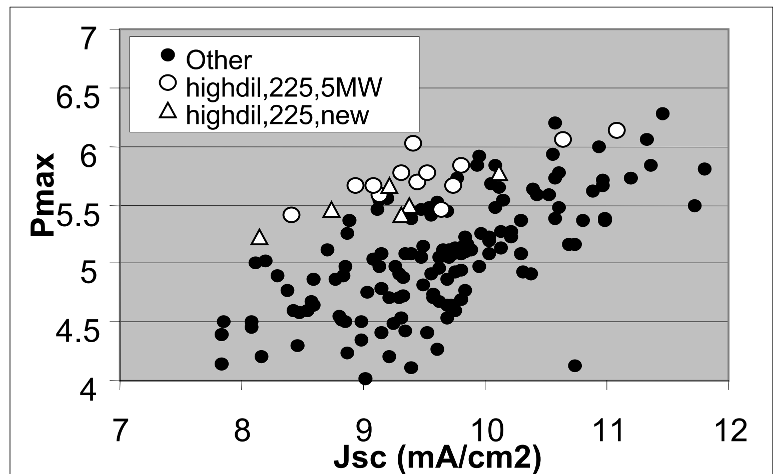

Fig. IV-11. Plot of efficiency versus short circuit current for cells made using the new and 5 MW style cathodes.

Table IV-3. Data for a-Si:H Cells Made Using the New and the 5 MW Style Cathodes.

Cathode Design	i-layer thickness (Å)	Deposition Rate (Å/s)	V_{oc} (V)	J_{sc} (mA/cm^2)	FF	R_s (Ωcm^2)	**P_{max} (mW/cm^2)**
New	1800	1.0	0.956	10.05	0.585	21	**5.62**
5MW	1730	0.96	0.943	10.08	0.614	20.5	**5.84**
New	2250	1.9	0.944	10.53	0.561	14.8	**5.58**
5MW	2100	1.8	0.949	10.57	0.618	11.8	**6.20**

There are several possible reasons for these poorer properties for the cells made using the new cathode design. As mentioned before, both the gas flow pattern and the electrical potentials related to the plasma are different in this new design. While the flow pattern and the potentials set up by the plasma can affect the i-layer quality, previous experience with different deposition reactors suggests that in this case, the different gas flow pattern in not likely the cause. Instead, we believe the electrical configuration is a more likely suspect. It was also observed that powder formation occurred more easily in this cathode configuration than with the 5MW style. Build-up of this porous powder material can lead to absorption of water vapor during venting and air exposure of the deposition system. This water vapor can later lead to oxygen incorporation in the i-layers and poor cell performance. This increased powder formation could be a result of the gas flow pattern or the electrical configuration. If this is the case, this may be a signal that the plasma associated with the new design contains more complicated Si based radicals which lead to the formation of polysilicon chains. However, we believe that it is for the most part related to complicated design which leads to the exposure of colder surfaces to depositing species.

The experience gained during the study of this first new cathode design led to the engineering of a second configuration. This design has a similar gas flow pattern to the first new design and thus we expect the deposition uniformity will be as equally good. Electrically and geometrically, this second design is more similar to the 5MW design and, thus, the cell properties and the i-layer quality should be improved over the first new design.

Static Testing of 2nd Generation New Cathode Design in the Single Chamber

With the second generation hardware, we altered the cathode design in order to achieve the desired electrical properties for the plasma. Figure IV-12 shows that, like the first generation hardware, we are able to obtain uniform deposition over a large section of the cathode area. In the figure, the deposition rate at various positions above the cathode is plotted across the cathode length. The deposition rate varies little over the length of the cathode even at relatively high deposition rates of 3.9 Å/s where the rate varies by ±6% (see figure).

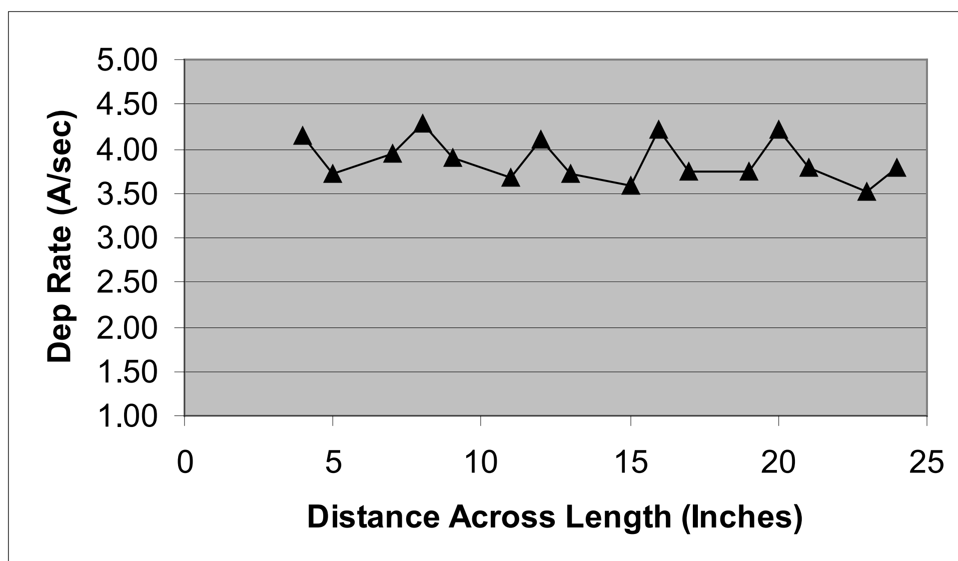

Fig. IV-12. Deposition rate vs. position along the cathode in the 2nd generation system.

Using this cathode hardware and the single chamber system for a-Si:H i-layer depositions, nip cell have been fabricated. In Table IV-4, data for these cells is compared with data for cells made using the 1st generation hardware and the single chamber system to prepare the i-layers. Cells with similar i-layer thicknesses (near 1500Å) and i-layer deposition rates are compared. One can see that the performance of this 2nd generation hardware is superior to that for the 1st generation hardware demonstrating a significant improvement. The cell efficiency (P_{max}) is higher due to a better fill factor (FF). These results encouraged us to test this new hardware design in the pilot roll-to-roll machine at United Solar where there would be no air break between doped and i-layer depositions.

Table IV-4. Comparison of performance of cells produced in the 1st and 2nd generation cathode hardware.

Cathode	V_{oc} (V)	J_{sc} (mA/cm^2)	FF	R_s (ohm cm^2)	P_{max} (mW/cm^2)
1st generation	**0.950**	**9.02**	**0.660**	**13.7**	**5.66**
2nd generation	**0.947**	**9.00**	**0.696**	**9.5**	**5.93**

Tests in Pilot Roll-To Roll Machine

Static Tests in the Pilot Roll-to-Roll Machine

In this Phases II and III of the program, the 2nd and 3rd generations of cathode hardware were installed in the pilot roll-to-roll machine. As mentioned previously, the film uniformity for the 2nd generation hardware was tested in a static mode using the single chamber system. In contrast, no such tests were made of the 3rd generation hardware prior to installation into the roll-to-roll processor. From the experience gained from the hardware testing already completed, it was felt that the probability of success with this

3rd generation hardware was high and that testing in the moving web system should be expedited.

Figure IV-13 displays two deposition rate profiles for a-Si:H films across the cathode length for the 3rd generation hardware. This data was obtained with the web in a static mode using the pilot roll-to-roll machine. Again, the deposition rate calculated from the film thicknesses over different position of the cathode is shown in the figure. The top profile is for an a-Si:H film prepared at an average rate of 2.9 Å/s while the second is for an a-SiGe:H film made at 4.3 Å/s. At the rates of 2.9 and 4.3 Å/s, these values are respectively 1.5 and 2.2 larger than the rate used in production. From this data, one can see that with the 3rd generation hardware, the goal of ± 5% thickness uniformity across 80% of the cathode areas has been achieved at deposition rates that are 1.5 and 2 times larger than those used in production. It is particularly important that this goal was achievable for the a-SiGe:H alloy.

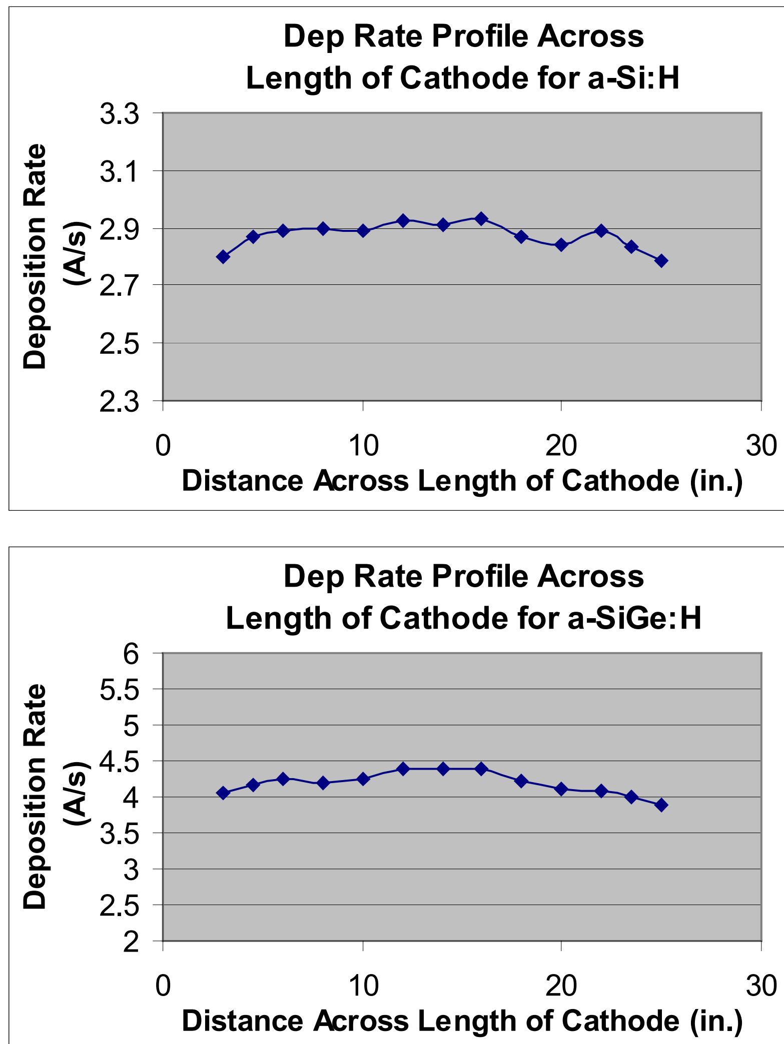

Fig. IV-13. Deposition rate vs. position along the cathode in the 3rd generation system.

Dynamic Tests in the Pilot Roll-to-Roll Machine

a-Si:H

In Table IV-5, data for 0.25 cm^2 a-Si:H cells made using the 2nd and 3rd generation hardwares in the pilot line are compared with data for a-Si:H cells made using the 5MW production line. All the cells were made without current enhancing back reflector layers and the ITO/Al contacts were made using small R&D evaporators. The i-layer thicknesses for the cells listed in the table are similar (near 1200 Å) as were the i-layer deposition rates (2Å/s). The doped-layers were made in the same roll-to-roll pilot deposition line used to make the i-layers. Thus, for each cathode hardware, the nip semiconductor stack was made in a true roll-to-roll manner. From the data in the table, it is clear that the cell made using the third generation hardware outperforms those made using the 2nd generation hardware. Also, the performance of these cells is superior to that for cells made using the standard 5 MW cathode hardware. In fact, by the end of Phase II of the program (8/00), the cell efficiencies obtained using the 3rd generation hardware were 4% higher than those made using the 5 MW cathode hardware with an excellent fill factor of 0.75. Thus with this third generation hardware, we were able to achieve the Phase II goal of a 3% increase in cell performance and a ± 5% thickness uniformity across 80% of the cathode area. Also, the 4% improvement was made without a full optimization of all the conditions used to make the i-layer. With further optimization of all the layer conditions in Phase III of the program, we were able to obtain cells with similar i-layer thickness that had higher currents and efficiencies (5.98 mW/cm^2) that were 6.8% higher than the efficiencies obtained using the 5MW style cathode, as is shown by the data listed in Table IV-5. Thus with this third generation hardware, we were able to achieve the Phase III goal of a 6% increase in cell performance and a ± 5% thickness uniformity across 80% of the cathode area.

Table IV-5. Comparison of performance of cells produced in the 2nd and 3rd generation hardware to cells produced in the 5 MW style hardware.

Cathode	V_{oc} (V)	J_{sc} (mA/cm^2)	FF	R_s (ohm cm^2)	P_{max} (mW/cm^2)
2nd generation	**0.947**	**7.2**	**0.727**	**9.7**	**4.96**
3rd generation (8/00)	**0.980**	**7.86**	**0.753**	**8.1**	**5.80**
3rd generation (8/01)	**0.975**	**8.30**	**0.739**	**8.2**	**5.98**
5MW	**0.968**	**7.90**	**0.724**	**8.1**	**5.60**

To test the ability to make high quality cells over a significant length of web, we have completed a 100m long run in which the deposition conditions were nominally fixed. For every 5M, a sample was taken and 0.25 cm^2 solar cells fabricated using the sample. The data for the cells is shown in Table IV-6. The following average cell parameters were obtained: V_{oc}=0.974V, J_{sc}=7.20 mA/cm^2, FF=0.746, P_{max} = 5.23 mW/cm^2. The efficiencies and J_{sc} values are lower than those quoted in Table IV-5 due to the fact that a higher deposition rate was used and thinner i-layers were obtained. The standard deviations for the values for each of the parameters are less than 3% of their average values; V_{oc}=0.008V (0.8%), J_{sc}=0.21 mA/cm^2 (2.9%), FF=0.005 (0.7%), P_{max} = 0.14 mW/cm^2 (2.7%). Thus, the good performance of the cells made using the 3rd generation hardware is reproducible over a 100M length of web. Because of the superior performance obtained using this 3rd generation cathode hardware, it will be implemented in United Solar's 25MW plant presently under construction. With this new hardware and other improvements to the manufacturing process, we believe products with higher performance will be made using the new production line.

Table IV-6. Data for cells made during 100m long deposition run in the pilot roll-to-roll machine using ~3 Å/s i-layer deposition rate.

	Cell Properties						
Meter Mark	Voc	Jsc	FF	Rs	Pmax	thick	Rate
10	0.964	7.75	0.739	9.2	5.53	1015	3.0
15	0.955	7.4	0.738	10	5.22	1104	3.3
20	0.963	7.29	0.755	8.9	5.3	1043	3.1
25	0.981	7.08	0.737	10.1	5.12	1008	3.0
30	0.98	7.07	0.743	10.1	5.15	1095	3.3
35	0.98	7.17	0.741	9.8	5.2	1069	3.2
40	0.968	7.18	0.752	9.1	5.23	1113	3.3
45	0.98	7.03	0.749	9.6	5.16	1073	3.2
50	0.979	6.96	0.742	9.3	5.06	1008	3.0
55	0.973	6.88	0.747	10.4	5	1086	3.2
60	0.983	7.35	0.747	9.1	5.39	1086	3.2
65	0.978	6.93	0.75	9.5	5.09	1082	3.2
70	0.976	7.43	0.747	8	5.41	1077	3.2
75	0.978	7.36	0.753	8.4	5.42	1199	3.6
80	0.972	7.24	0.751	8.3	5.28	1137	3.4
85	0.982	7.1	0.747	9.7	5.21	1082	3.2
90	0.97	7.08	0.744	9.2	5.11	1031	3.1
95	0.961	7.27	0.743	9.8	5.19	1019	3.0

a-SiGe:H

After having established the benefit of using the 3rd generation hardware for a-Si:H cell fabrication, a number of a-SiGe:H single junction cells were made using this new cathode hardware. In particular, one of our main interests was to determine if with this new hardware, good devices could be made using inexpensive silane (SiH_4) gas rather than disilane (Si_2H_6). The first studies were done using conditions close to those used for middle cell fabrication. Listed in Table IV-7 are IV data measured after 600 hrs. of light soaking for a-SiGe:H cells prepared using the different gas mixtures. As a reminder, all of these cells were prepared in the pilot roll-to-roll machine using the 3rd

generation hardware. The cells have similar i-layer thicknesses, were made without current enhancing back reflectors and the i-layers were prepared at deposition rates near 2.5 Å/s. Also the efficiencies are lower than those obtained in R&D systems partly due to the fact that the i-layers do not have graded Ge profiles. Since a-SiGe:H component cells in the high performance triple-junction structures are used to collect light from the green-red portion of the solar spectrum, the IV data shown in the table were obtained using AM1.5 light filtered using a 530 nm long pass filter to eliminate light absorbed by the top a-Si:H cell in the a-Si:H/a-SiGe:H/a-SiGe:H structure.

In the table, the red-light powers (P_{max}) listed are proportional to the cell efficiencies. Bolded in the table are the light soaked P_{max} values and the amount of degradation from the initial values. One can see that presently there is very little difference in the light soaked P_{max} values for cells made using the SiH_4 or Si_2H_6 silicon source gas. Only one of the SiH_4 cells seems to have degraded more than the other cells (25% compared with 18-21%), however this is likely related to a slightly thicker i-layer.

Table IV-7. Data for 0.25cm^2 Cells Made Using 3rd Generation Cathode and Different Gas Mixtures.

Gas Mixture	Light Soak. Condition	V_{oc} (V)	J_{sc} (mA/cm^2)	FF	R_s (ohm cm^2)	P_{max} (mW/cm^2)	% of Degrad.
$SiH_4 + GeH_4$ Cell #1	Initial	0.762	8.74	0.620	9.6	4.12	-
	Light Soaked	0.729	8.07	0.525	15.5	3.09	25
$SiH_4 + GeH_4$ Cell #2	Initial	0.746	8.60	0.618	9.7	3.96	-
	Light Soaked	0.717	8.08	0.537	14.7	3.11	21.5
$Si_2H_6 + GeH_4$ Cell #3	Initial	0.721	8.80	0.609	9.4	3.86	-
	Light Soaked	0.695	8.26	0.545	13.3	3.13	18.9
$Si_2H_6 + GeH_4$ Cell #4	Initial	0.775	8.14	0.639	9.7	4.03	-
	Light Soaked	0.735	7.76	0.552	13.9	3.15	21.8

We have also prepared a number of cells having i-layers with higher Ge contents, conditions closer to what is used for the bottom component cell of an a-Si:H/a-SiGe:H/a-SiGe:H triple-junction device. In particular, a series of a-SiGe:H alloy cells with red-light V_{oc} values near 0.60 and i-layer thicknesses near 1000-1200 Å. Listed in Table IV-8 are IV data for some of the low bandgap a-SiGe:H cells prepared using different gas mixtures. The cells have similar i-layer thicknesses, were made without current enhancing back reflectors and have i-layers prepared at deposition rates near 1.5 Å/s. Again the efficiencies are lower than those obtained in R&D systems partly due to the fact that the i-layers do not have graded Ge profiles or a-Si:H buffer layers. Also the IV

data shown in the table were obtained using AM1.5 light filtered using a 530 nm long pass filter to eliminate light absorbed by the top a-Si:H cell in the a-Si:H/a-SiGe:H/a-SiGe:H structure.

Focusing on the data in the table, while there are slight differences in the currents and V_{oc} values for the different cells (likely due to small differences in the i-layer bandgap), the P_{max} values for the cells made using the different gas mixtures are within experimental error demonstrating that with this new cathode hardware, SiH_4 can also be used to make high quality bottom cells.

Table IV-8. Data for Cells Made Using 3rd Generation Cathode and Different Gas Mixtures.

Gas Mixture	Light Soak. Condition	V_{oc} (V)	J_{sc} (mA/cm^2)	FF	R_s (ohm cm^2)	P_{max} (mW/cm^2)
$SiH_4 + GeH_4$ Cell #1	Initial	0.618	7.35	0.668	8.7	3.04
$SiH_4 + GeH_4$ Cell #2	Initial	0.587	8.14	0.640	8.7	3.06
$Si_2H_6 + GeH_4$ Cell #3	Initial	0.626	7.50	0.662	8.9	3.11
$Si_2H_6 + GeH_4$ Cell #4	Initial	0.603	7.78	0.643	9.0	3.01

Light soaking studies of the low bandgap a-SiGe:H cells were also made. Figure IV-14 shows the P_{max} values obtained by filtering the light with a 530 nm cutoff filter after light soaking the samples for 1000 hrs. as a function of i-layer thickness. In the figure, we compare data for cells made with SiH_4 to the data for devices made with Si_2H_6. Focusing on cells with similar i-layer thickness, the difference in P_{max} values between cells made with the two different gas mixtures are within experimental error. Thus, not only are the cells made with the two different gases have similar initial cell efficiencies, they also have similar stable P_{max} values.

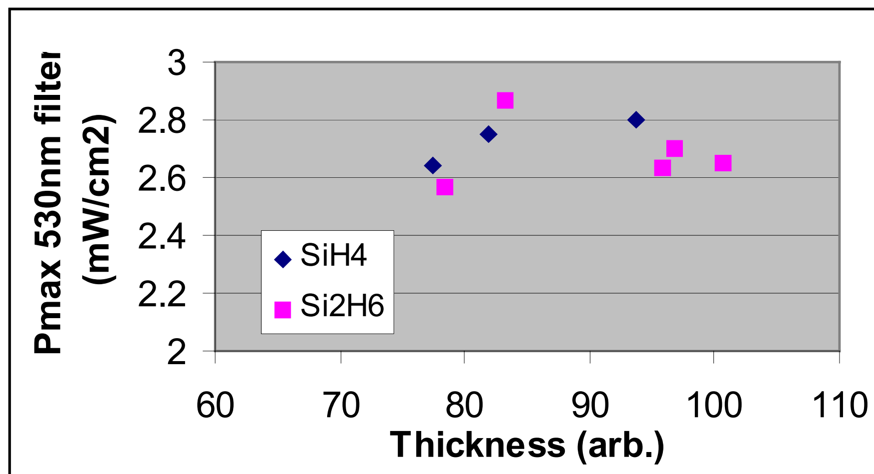

Fig. IV-14. Light-soaked P_{max} values for a-SiGe:H cells with red-light V_{oc} near 0.6V as a function of I-layer thickness.

We have also studied the effect of lowering the total gas flow to determine if lower gas flows can be used to minimize production costs. Listed in Table IV-9 are IV data for some of the low bandgap a-SiGe:H cells prepared using different total gas flows. Again, there is data for some cells made using SiH_4 and also data for cells made using Si_2H_6. The total flow was altered by a factor of three from the standard flows. One can see from the data in the table that all of the cells have red P_{max} near 3.3-3.4 mW/cm^2 with the slight differences in the exact values within experimental error. Thus with the 3rd generation hardware allows for the use of lower flows without a decrease in cell performance.

Table IV-9. Data for Cells Made Using 3rd Generation Cathode and Different Gas Flows.

Gas Mixture	Total Gas Flow	V_{oc} (V)	J_{sc} (mA/cm^2)	FF	R_s (ohm cm^2)	P_{max} (mW/cm^2)
$SiH_4 + GeH_4$	Standard	0.632	8.26	0.643	9.2	3.35
$SiH_4 + GeH_4$	1/3 x Standard	0.640	8.28	0.648	8.6	3.44
$Si_2H_6 + GeH_4$	Standard	0.621	8.73	0.620	8.8	3.31
$Si_2H_6 + GeH_4$	1/3 x Standard	0.616	8.80	0.621	8.9	3.37

A series of a-SiGe:H alloy cells were also prepared on Al/ZnO back reflector. The back reflector was made using United Solar's 5MW plant equipment. With the use of the back reflector, higher currents are obtained and any slight differences in the cell performance are magnified. Listed in Table IV-10 are IV data for some of the low bandgap a-SiGe:H cells prepared with back reflectors using the two different gas mixtures. The cells made using the SiH_4 gas have slightly higher performance (P_{max}) than the cells made using the more costly Si_2H_6 gas. However, the difference is not very large.

Table IV-10. Data for Cells With Back Reflectors Made Using 3rd Generation Cathode.

Gas Mixture	V_{oc} (V)	J_{sc} (mA/cm^2)	FF	R_s (ohm cm^2)	P_{max} (mW/cm^2)
$SiH_4 + GeH_4$	0.612	6.42	0.610	12	2.40
$SiH_4 + GeH_4$	0.598	6.47	0.641	10.7	2.48
$Si_2H_6 + GeH_4$	0.598	6.46	0.615	11.4	2.38
$Si_2H_6 + GeH_4$	0.553	6.97	0.612	10.8	2.36

It is obvious from these studies that the 3rd generation cathode hardware can be used to make good a-Si:H and a-SiGe:H cells uniformly over large cathode areas and with SiH_4 as the silicon source gas.

Dynamic Tests of 3rd Generation Hardware in the 5MW Line

While the tests previously mentioned demonstrate the ability to make good, uniform cells with the 3rd generation hardware, they did not prove the long-term use of the cathode in a production environment. With this fact in mind, a 3rd generation style of cathode was built and installed into the 5MW production line. As of 9/01, the hardware has been used in a chamber for a-Si:H deposits for over 9 months. During this period, we have completed a number of "static burns" where the web in the production machine was not moving while a timed deposit was made with the 3rd generation hardware. The thickness across the burn area was measured from which deposition rates were calculated. In Figure IV-15, the deposition rate across the length of deposits obtained at different times are compared. In the figure, all of the burns were made under nominally the same deposition conditions except for the use of the different cathode hardwares. One can see that the profile made using the 3rd generation hardware after three months of usage (4/30/01) is very similar to that obtained just after installation (2/01) with only a slight increase in the average deposition rate from 3.7 to 3.9 Å/s (see values quoted in legend), an increase very close to the experimental error. Thus, the reproducibility of the deposits made with this new cathode hardware are good and the potential for long term usage of this new hardware is high. Also from the figure, one can see the flatter deposition profiles obtained with this new cathode over the previously used 5MW hardware where the deposition rates vary from roughly 2 to 5 Å/s. It is also important to note that the average deposition rates are similar demonstrating that the gas utilization is similar for both cathodes. We will continue to monitor the cell performance and uniformity beyond the length of this program.

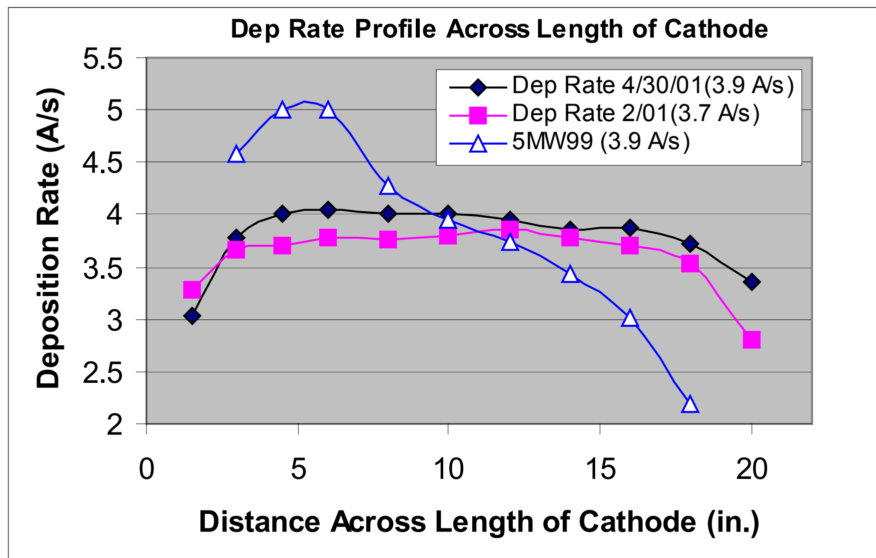

Fig. IV-15. Deposition rate profiles across cathode length for 3rd generation hardware installed in 5MW production machine.

Testing of 3rd Generation Cathode for 25MW Line

Having met all of the deliverables and milestones for this portion of the program, we have developed new cathode hardware which will be implemented in United Solar's new 25MW line. In this line, the cathode hardware has been designed to simultaneously deposit on six 14" wide webs, in contrast to the TA2 and 5MW lines where the cathode hardware was designed to deposit on only one web at a time. While the general concept of the cathode hardware for the 25MW line will follow that of the 3rd generation hardware developed in this program, the exact hardware has been designed to be significantly larger. In any scale-up of machinery, some small details must be tested in order to assure one the ability to achieve the expected results (in our case, a uniform stable plasma and deposit which leads to high cell efficiencies). Thus, we are planning to build a test chamber that is nominally the same as those used in the actual 25MW line. This chamber will be assembled at ECD's plant 2 and plasmas tested and deposits made in the following months. If any difficulties in obtaining the desired deposits are encountered, corrections to the hardware will be made and tested using this chamber. The corrections will then be applied to the production line chambers. In longer term studies, the chamber will also be used to complete studies of the plasmas chemistries generated by the mock production cathode and the information used to further improve the cathode hardware. During the writing of this manuscript, the test chamber was being constructed.

Modeling for Amorphous Silicon Deposition

Introduction

In the first year of this program the major accomplishment was to convert a Boltzmann code, previously developed for simulating diamond deposition, chlorine etching, and oxygen ashing in plasma reactors, to a code appropriate for modeling the plasma assisted deposition of amorphous silicon. An important component of this involved determining which neutral and ion gas species are needed to accurately simulate the gas chemistry. In addition, a crude model, appropriate for a one-point code, was incorporated to model diffusion to the walls and silicon deposition. The code was then debugged and run using conditions appropriate to a specific reactor run and the predictions of the code were compared to data. Comparisons with the thickness of the deposition at the center of the substrate showed good agreement. As a one-point code this simulation is incapable of showing either the effects of sheaths, and hence ions, at the walls or the effects of non-uniformity in the electric field, which can lead to non-uniformity in the deposition. To begin to address these issues we also adapted a 1D RF code to this problem and this code has been tested. Now that the Boltzmann code has been validated against data it will be run for a variety of electric field parametric values to generate a table of electron energy distributions and neutral densities appropriate to each value of the local electric field. These tabular values will be inserted in the RF code to generate predictions of sheath structure and ion dynamics. When this code is validated a 2D version will be constructed to more accurately account for neutral

diffusion effects. These tools will provide a reliable means of simulating the major physical effects in the reactor.

Simulation Strategy

Simulating an RF system involves an analysis of local and global phenomena. In the pressure regime appropriate for the ECD reactor, these phenomena de-couple. On the global level we can write continuity equations for electron, ion, and neutral species particles and momentum. These equations treat each species as a fluid and do not solve for the velocity space distribution functions of the species. The continuity and momentum equations for each species would be an exact description of the system if we knew the pressure tensor. This however involves solving an unending chain of higher order moment equations. Fortunately, for the case at hand we are able to make simple and accurate assumptions as to the form of the pressure tensor for each species in terms of the species density.

The continuity equation for the electron and ion momenta requires a knowledge of the electric field distribution, which for this frequency range can be derived from the electrostatic potential. The potential is obtained by solving Poisson's equation given the electron and ion densities. Thus far all of the quantities required are global quantities, which involve solving equations on the scale of the reactor. However, the solution of the various continuity equations depends on local processes as well. Some of these involve neutral kinetics: neutral species A and B interact to form neutral species C and D. Others involve electron mediated processes: an electron impacts molecule A and produces molecules B and C, or an electron impacts species A and knocks off an electron producing an electron- ion pair.

While the neutral-neutral interactions can be obtained from kinetic rate information, calculating the electron rates for electron-neutral processes involves solving for the electron distribution function. The solution depends on the value of the electric field during the entire history of the particle. In low pressure systems this requires a global solution since electrons at one point may have been heated by electric fields at another spatial point at and earlier time. At the higher pressure of the ECD reactor, electrons move only a short distance in space during a typical heating time due to the short mean free path. Therefore the electron energy distribution function depends only on the local value of the RF electric field: an enormous simplification. This permits us to solve for the electron rates as a function of the local electric field at each point in space and then to use these rates in the various continuity equations. These continuity equations then advance the electron and ion densities, which produce a new global electric field that can then be used to recalculate the electron rates. Thus the simulation strategy is now complete. We discuss below further details of the solution method for the electron distribution function and describe how this local analysis can be used to approximate the entire reactor.

Solution of the electron energy distribution function - As described above the short mean free path permits a local solution of the electron energy distribution function. It also produces to lowest order an isotropic velocity distribution function with a higher order distortion in the direction of the electric field. This is the physical basis behind the "two term expansion'' model of the Boltzmann equation, which is used to obtain the isotropic portion of the electron energy distribution function. The numerical solution to this model is referred to below as the Boltzmann code. However, the numerical solution of even this highly simplified model Boltzmann equation is time consuming and it is computationally tedious to solve this equation at every spatial point in the simulation. We therefore use the Boltzmann equation to fit the electron rates to an analytic function of the local electric field and then use this analytic function in the global solution for the fields.

One-Point Simulations

Although the Boltzmann code calculates the electron distribution function at a single point in space we can use it to investigate the chemistry of the entire reactor by simplifying the global continuity equations. In this model we write equations for the time dependence of globally averaged number densities of electrons, ions and neutrals. The local production and loss terms for each species are calculated as in a full global model, but the spatial loss rates such as convection or diffusion to the reactor walls are included parametrically as decay times for each specie. The electron-neutral rates however require a knowledge of the local electric field, which we do not know since we are only solving a one point problem. We obtain an estimate of the local electric field by requiring that the local power deposition have a particular value. At any moment we know the average electron density and we can compute the energy loss rate by electrons to neutrals for a given electric field. We adjust the local electric field to give the desired local power deposition. This approximation assumes that most of the RF power deposited is lost by electron-neutral inelastic collisions rather than into accelerating ions. In order to obtain a better estimate of this energy a 1D or 2D global solution is required to estimate the average RF sheath. This will be done in the coming weeks.

RF-Global Simulation

The field distribution within the reactor is the result of the applied potentials to the various metal surfaces within the reactor and the charged particle space charge densities. These charged particle densities in turn are affected by the electric fields. Specifically, electrons move rapidly in such a way as to screen out the electric field within the core of the plasma. Thus a combined solution of the electron and ion continuity equations together with Poisson's equation is required. There is a wide discrepancy in the time scales for the various processes, however. Electrons respond to an applied electric field on the plasma time scale, the fastest time scale in the process, typically much faster than an RF period. Ions however respond on a much slower time scale, typically comparable to the RF frequency. They move through the core of the plasma on a time scale given by the inverse of the ion sound speed divided

by the reactor plate separation. This time scale is typically several RF periods. The ion dynamics in the RF sheath can be complex since the ion sheath crossing time can either be fast or slow compared to the RF frequency. For applications in which the ion distribution function striking the powered electrode is crucial, this needs to be resolved accurately. For our purposes we can approximate the ions as falling through an RF averaged potential.

The solution of the electron dynamics can be approached at various levels of the approximation. In the RF code being used for this project the primitive electron momentum equation is solved. It is also possible to use a drift-diffusion approximation in which the inertial term in the electron momentum equation is neglected. Each solution method has its advantages and disadvantages.

It is useful at this point to review some of the main physical processes in an RF plasma since they help to set in context the one-point Boltzmann calculations that have been done thus far. If the ion mass is sufficiently heavy, ions that are created in the plasma core fall towards the powered and grounded electrodes. This outward motion to the walls is sped up by an electrostatic field that hinders electrons from escaping at the much faster rate that would be determined by their diffusion to the walls in the absence of electric fields. The ion and electron loss rates must be very closely matched or a large charge imbalance will occur in the calculation leading to large electric fields that inhibit the escape of the faster species. Thus within the plasma core there is a potential structure set up by the requirement of equilibrating electron and ion losses. This potential structure, which is concave downward would exist even if there is no RF voltage applied to the electrodes.

In an RF plasma one of the electrodes is driven sinusoidally. As this electrode goes negative it pushes electrons back into the plasma core producing an RF sheath. These electrons move through the core of the plasma and are deposited in the sheaths at the grounded surfaces reducing the width of these sheaths and hence their potential height. The movement of the electrons from the driven electrode sheath through the plasma core to the ground sheath is driven by an electric field that is superimposed on the ambipolar field structure, and which is hindered by collisions between the electrons and neutrals. This combination of an electric field that pushes electrons and collisions with neutrals, which randomize the directed velocity given to the electrons by the field, is what produces electron heating. It is in fact this electric field which will be used in the Boltzmann equation and which will return the electron rates and the average electron energy.

In the pressure regime of interest this is the primary heating mechanism for electrons. At lower pressures where the electron mean free path is larger than the plate separation, the interactions between the electrons and the moving sheaths must be taken into account. This is not yet a solved problem and we are fortunately able to neglect heating due to the sheath movement in this pressure regime.

In the RF code that will be used for this project, the primitive electron momentum balance equation is advanced in time. The short time step requirement that this introduces is relaxed by using an implicit solution for the fields. The RF code will generate the local electric field at every spatial point and also the electron currents. The electron currents will then be used to deduce the residual electric field; this is then used to calculate the electron rates using analytic fits to solutions of the Boltzmann code.

The Boltzmann Code

The primary purpose of the Boltzmann code is to calculate the electron energy distribution function for different spatial locations in the reactor, associated with different values of the electric field strength. The distribution will be determined by the electric field strength and the electron cross sections of the dominant gas species. The input gas species are hydrogen (H_2) and silane (SiH_4). The electron energy distribution determines the rate of all electron processes including ionization, dissociation, vibrational heating, etc. To calculate the rates requires knowledge of these basic cross sections. Once the rates are established and applied, chemical radicals and ions are generated and neutral and ion chemistry ensues, usually coming to steady state equilibrium in times of the order of milliseconds to tens of milliseconds. The species also diffuse to the walls and substrate. In particular, in the reactor it is the radical SiH_3 that diffuses to the substrate and is deposited, leading to the amorphous silicon deposition.

A. *Chemistry Model* – The chemical species consist of neutrals, positive ions, negative ions, and electrons. We use a fairly large set, among which there are many that will exhibit very small concentrations. It might be thought that these could be disposed of to simplify the chemistry. This is not always the case, however. A species may have a small concentration resulting from a high production rate balanced by a high loss rate. The loss rate may be producing a more stable specie that could not be formed without the precursor specie. In other cases, in retrospect, some perhaps could be omitted. The model species are as follows:

Neutrals –	H_2, SiH_4, H, SiH_3, Si_2H_6, SiH_2, SiH, Si, Si_2H_5, Si_2H_4, Si_2H_3, Si_2H_2, Si_2H, Si_2, Si_3H_5, and Si_3H_8. Also, integrated are the first and second vibrational levels of hydrogen, H_2(v=1) and H_2(v=2).
Positive Ions -	H^+, H_2^+, H_3^+, SiH_3^+, SiH_2^+, SiH^+, $Si_2H_7^+$, $Si_2H_5^+$, $Si_2H_4^+$, $Si_2H_3^+$, $Si_2H_2^+$, Si_2H^+, $Si_3H_7^+$, $Si_3H_6^+$, $Si_3H_5^+$, and $Si_3H_4^+$.
Negative Ions -	H^-, SiH_3^-, $Si_2H_5^-$, and $Si_3H_7^-$.
Electrons -	e^-.

As we have stated, electron cross sections are needed to calculate the electron distribution function and the electron rates. The code carries 37 cross sections for this purpose, including those for H_2, SiH_4, H, SiH_3, and Si_2H_6. Figures IV-16 through IV-22 exhibit a selection of these cross sections.

B. *Boltzmann Simulation* – As outlined above, we are performing a one-point calculation. This requires us to approximate the diffusion of species to the wall and the effect at the wall, whether reflection or sticking. Fortunately, there is a fairly complete experimental measurement set for the sticking coefficients of the various radicals. Incorporating these coefficients generates a gradient in each specie density approaching the wall, which is used to estimate the diffusion rate through hydrogen of that specie to the wall. This is then used in the code to decrease (or increase) each specie density appropriately to approximately account for diffusion effects.

In addition, if we need to run the chemistry for perhaps as long as a few hundredths of a second to each equilibrium we need to determine if a molecule of hydrogen or silane will remain within the plasma long enough for the radicals to reach equilibrium. Therefore, we calculate the residence time of molecules in the reactor. Figure IV-23 is a schematic of the reactor we are modeling. The reactor parameters are:

pressure = 1 Torr,
gas temperature, T_g, = 250 C = 523 K,
gas flow rate, F, is 1050 sccm of H_2 and 50 sccm of SiH_4, which implies a total of 1100 sccm.

From the figure, the cross sectional area for the flow is 17.16 in. x 1.5 in., which in centimeters gives an area, A, of 166.1 cm^2. Then the flow velocity, u, in cm/s is

$$u = (0.046)F(\text{sccm})T_g/(A(\text{cm}^2)/p(\text{Torr})$$

The constant 0.046 = 760/273/60 is needed to reconcile the units. Putting in the numbers gives a velocity of 159.3 cm/s. Thus if y is the length of the reactor (17.16 in.), the residence time, R, is

$$R = y/u = 0.27 \text{ s.}$$

Therefore, the molecules will be in the plasma long enough for the chemistry to come to steady state equilibrium.

The conditions for the simulation include a power source of 85 watts. For this one-point calculation we assume the plasma is uniformly distributed, so we divide by the volume to get the power per unit volume at any point in the reactor. We take the H_2 fraction to be 95.45% and the SiH_4 to be 4.55%, which gives initial densities of $H_2 = 1.76\times10^{16}$ cm^{-3} and $SiH_4 = 8.40\times10^{14}$ cm^{-3}.

Simulation Results – The simulation was run initially to 0.01 s. Upon plotting the results it was unclear if the critical radical, SiH_3, had reached equilibrium. Therefore, we reran the code, this time to 0.03 s, and replotted SiH_3. Thus, all the plots we show are out to 0.01 s except the one that includes the SiH_3, which is plotted to 0.03 s. We show, first, plots of the electron distribution function as a function of energy at different times after

plasma turn-on, then plots of the neutral species, positive ions, negative ions, and electrons. Finally, we calculate, based on these results, the depth of the amorphous silicon deposition.

A. *Electron Energy Distribution Function* – Despite the fact that silane is present at less than 5% of the gas concentration, it does impact the distribution function. This is because the thresholds for ionization, dissociation, and vibrational excitation all are lower in silane than they are in hydrogen. Because the electron number density tends to fall off exponentially with increasing energy, the lower thresholds for the electron impact processes for silane overcomes to some degree the effect of the low fractional concentration of the silane. To illustrate the evolution of the electron energy distribution function we show in Figures IV-24-27. the distribution function respectively very soon after turn-on ($1.75x10^{-8}$s), at near 1 μs after turn-on, at approximately 0.1 ms, and finally at the end of the run, ~ 0.01 s. At the earliest time (Fig. IV-24) the electron density is still low (~10^5 cm^{-3}) and the available energy is shared fairly evenly among the electrons. Thus, we have a flat energy profile with a very high average electron energy, ~29 ev. This high energy rapidly ionizes the gas further and by a microsecond (Fig. IV-25) the electron number density has increased above 10^8 cm^{-3} and the average electron energy has dropped to about 4 ev. By about a tenth of a millisecond (Fig. IV-26) the electron density has risen to ~10^9 cm^{-3} and the average energy is 2.3 ev. These values are nearly the equilibrium values that we see in Fig. IV-27; electron number density ~ $1.8x10^9$ cm^{-3} and average energy = 2.15 ev.

B. *Neutral Specie Evolution* – The major neutral species are shown in plots Figs. IV-28 through IV-32. The critical radical, for our purposes is SiH_3 and in plot 28. it is shown as it evolves out to 0.03 s, where it has essentially reached steady state equilibrium. Its concentration is a few percent of the silane concentration. Other major species critical to the chemical evolution are atomic hydrogen, H, and disilane (Si_2H_6). In plot 29., we show the first two vibrational states of hydrogen. H_2(v=1), in particular, builds up to a density higher than that of any of the radicals and does have an impact on the chemistry. Several radicals are produced in appreciable quantities, such as Si_2H_5 (30) and Si_3H_5 (32).

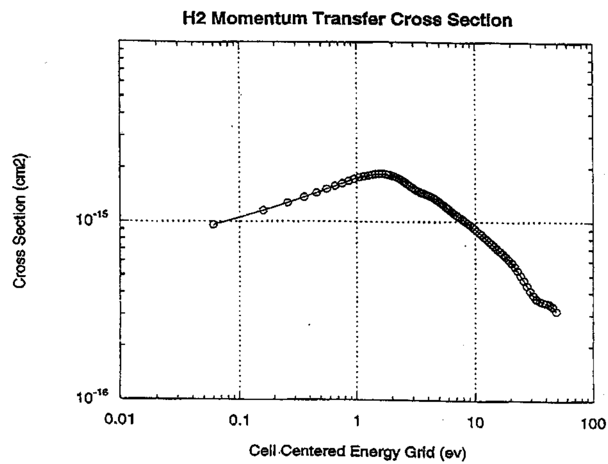

Fig. IV-16. Electron Impact Cross Sections (cm^2): H_2 momentum transfer.

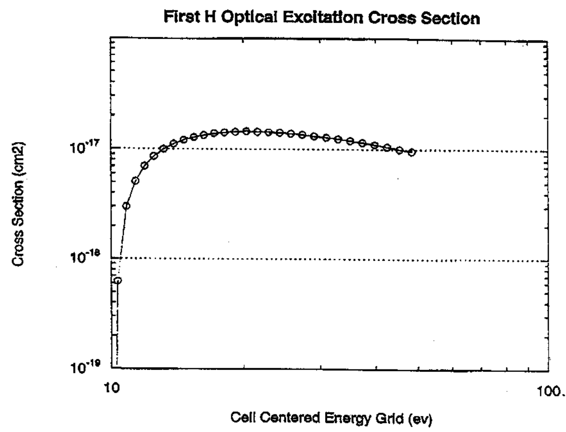

Fig. IV-17. Electron Impact Cross Sections (cm^2): Lowest threshold H optical excitation.

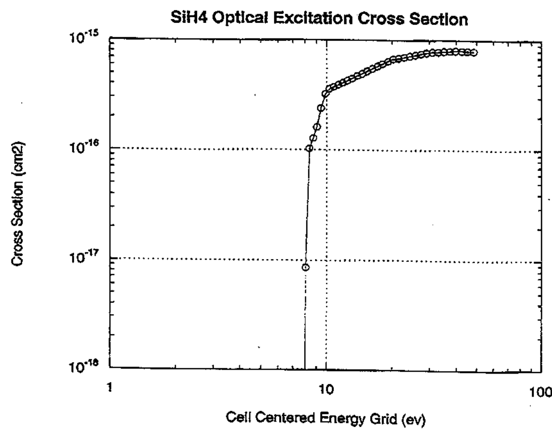

Fig. IV-18. Electron Impact Cross Sections (cm^2): SiH_4 optical excitation.

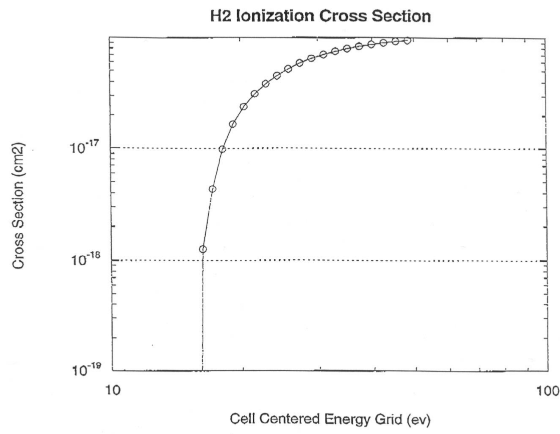

Fig. IV-19. Electron Impact Cross Sections (cm^2): H_2 Ionization.

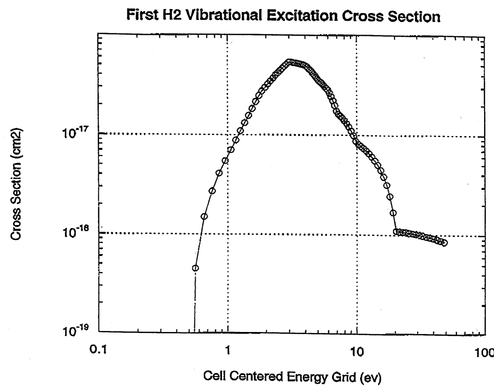

Fig. IV-20. Electron Impact Cross Sections (cm^2): Lowest threshold H_2 vibrational excitation.

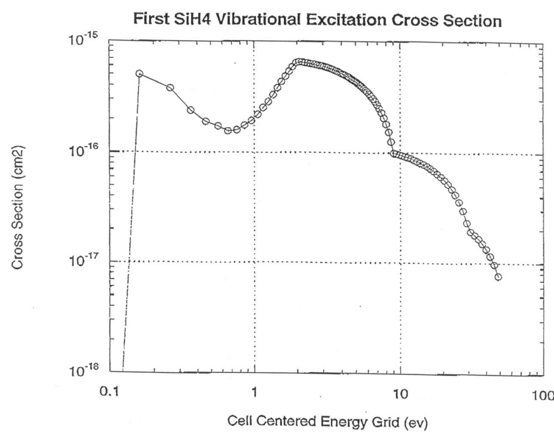

Fig. IV-21. Electron Impact Cross Sections (cm^2): Lowest threshold SiH_4 vibrational excitation.

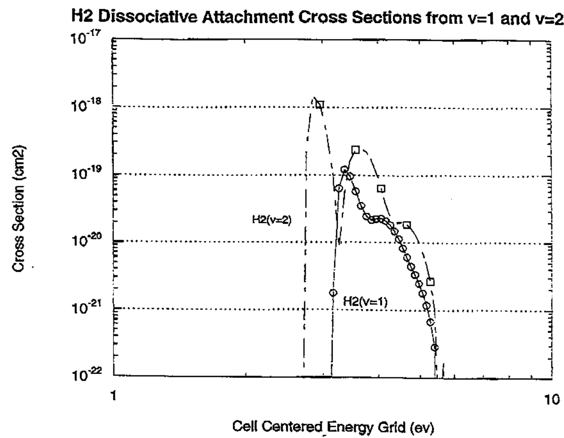

Fig. IV-22. Electron Impact Cross Sections (cm^2) Dissociative attachment from the v=1 and v=2 vibrational states of H_2.

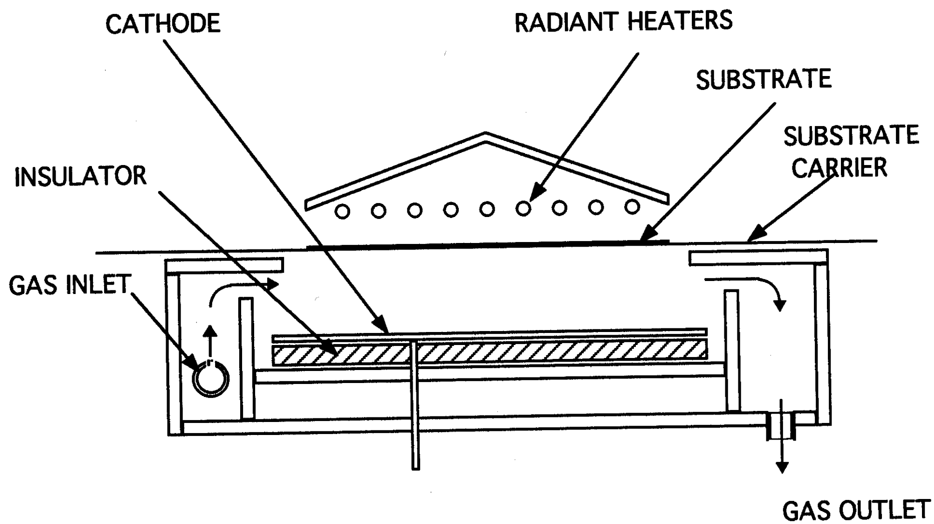

Fig. IV-23. Modeled RF Reactor Subchamber Design.

C. *Positive Ion Evolution* – Figures IV-33 through IV-35 show the generation of the positive ions. Initially, H_2^+, H_3^+, SiH_3^+, and SiH_2^+ are the major positive ions as a direct result of ionization of H_2 and SiH_4 but there is a rapid evolution toward the heavier ions, including $Si_2H_7^+$, $Si_3H_7^+$, $Si_3H_6^+$, and $Si_3H_5^+$. These dominate by a millisecond or earlier.

D. *Negative Ion Evolution* – Figure IV-36 shows the negative ion evolution. As with the positive ions we start with SiH_3^-, a result of dissociative attachment of an electron reacting with silane, as the dominant ion. Again there is the conversion to heavier ions and by 0.01 s $Si_3H_7^-$ dominates.

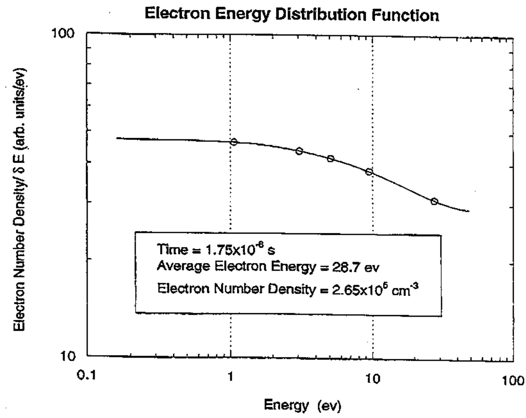

Fig. IV-24. Electron Energy Distribution functions at various times after turn-on: 1.75x10^{-8}s.

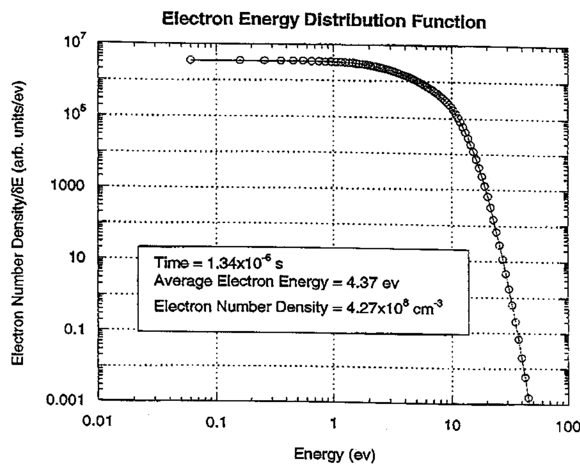

Fig. IV-25. Electron energy distribution functions at various times after turn-on: 1.34x10^{-6}s.

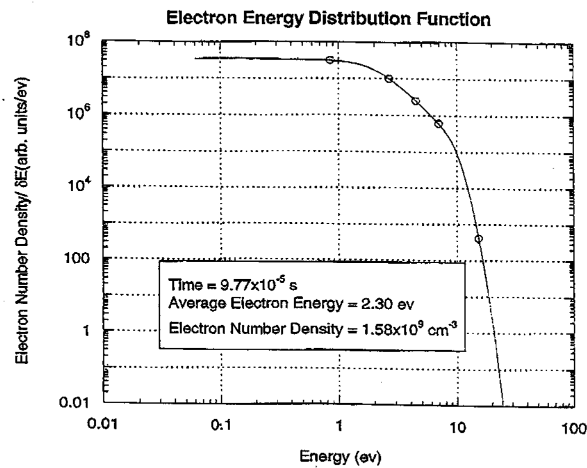

Fig. IV-26. Electron energy distribution functions at various times after turn-on: 9.77x10^{-6}s.

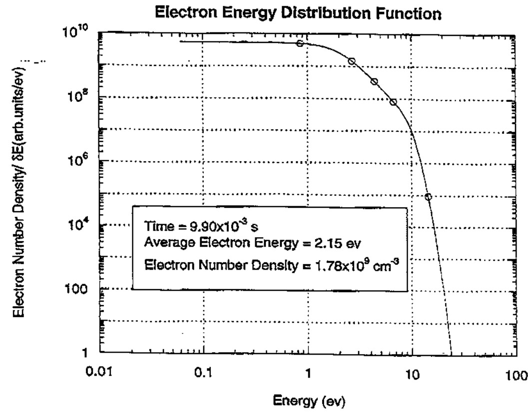

Fig. IV-27. Electron energy distribution functions at various times after turn-on: 9.90×10^{-3}s.

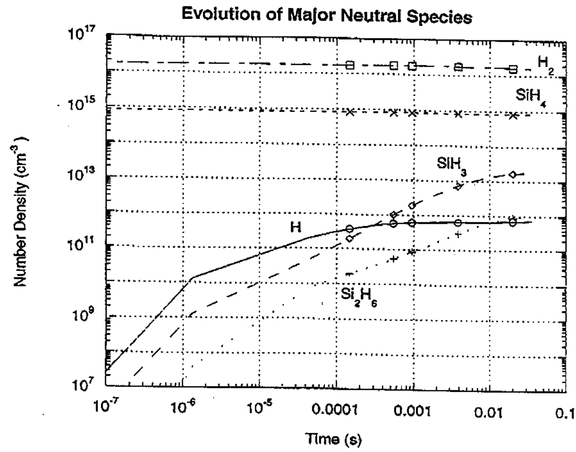

Fig. IV-28. Evolution of Neutral Species (cm^{-3}): H_2, SiH_4, H, SiH_3, SiH_6

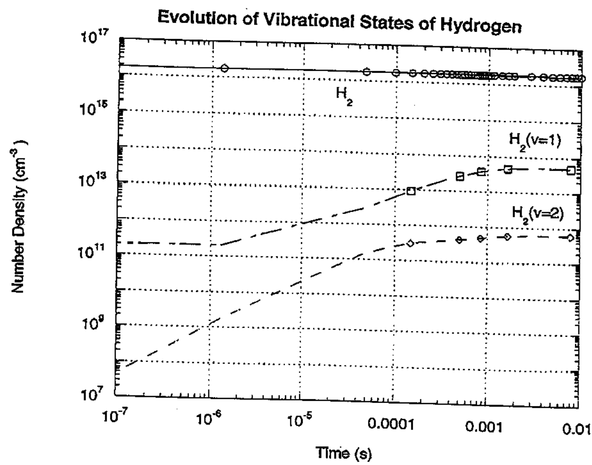

Fig. IV-29. Evolution of Neutral Species (cm^{-3}): H_2, $H_2(v=1)$, $H_2(v=2)$

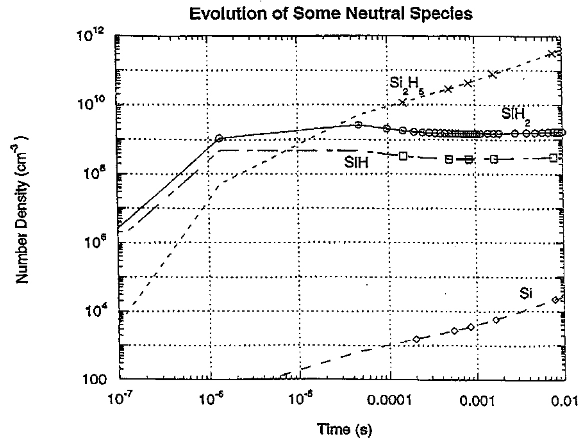

Fig. IV-30. Evolution of Neutral Species (cm^{-3}): Si_2H_5, SiH_2, SiH, Si

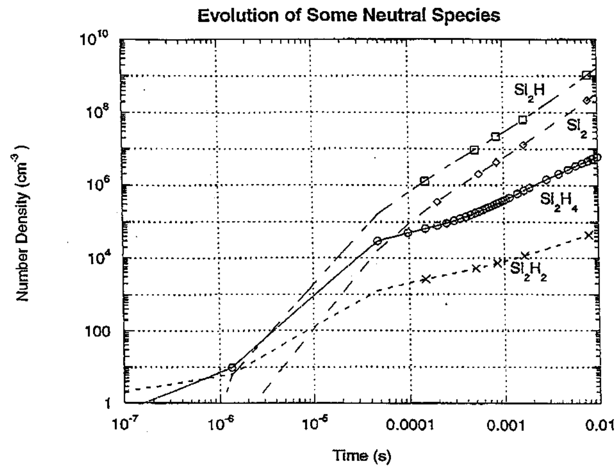

Fig. IV-31. Evolution of Neutral Species (cm^{-3}): Si_2H_4, Si_2H_2, Si_2H, Si_2

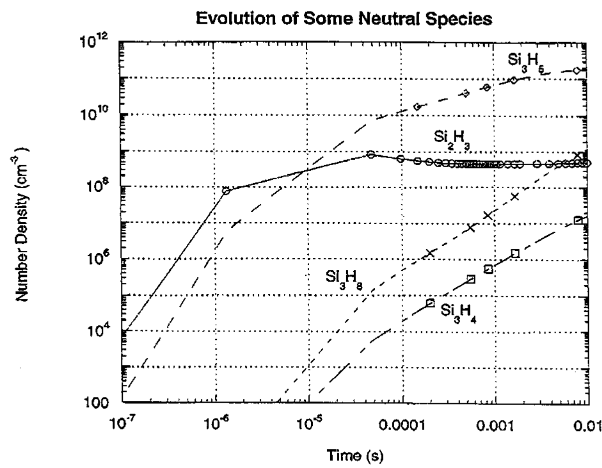

Fig. IV-32. Evolution of Neutral Species (cm^{-3}): Si_2H_3, Si_3H_8, Si_3H_5, Si_3H_4.

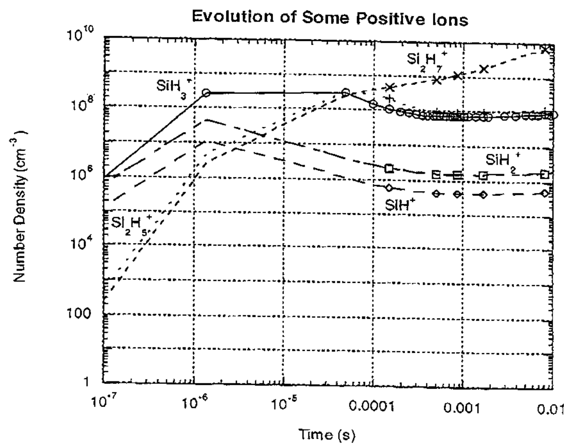

Fig. IV-33. Evolution of Positive Ions (cm^3): SiH_3^+, SiH_2^+, SiH^+, $Si_2H_0^+$, $Si_2H_5^+$.

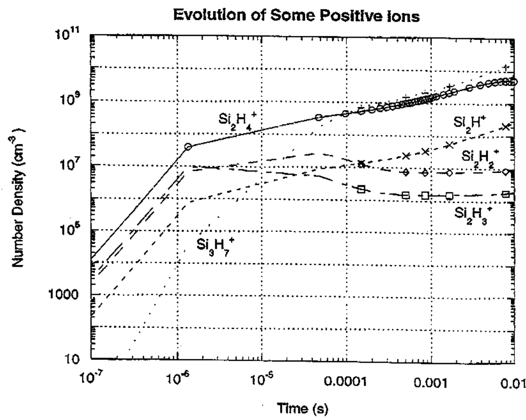

Fig. IV-34. Evolution of Positive Ions (cm-3): $Si_2H_4^+$, $Si_2H_3^+$, $Si_2H_2^+$, Si_2H^+, $Si_3H_7^+$.

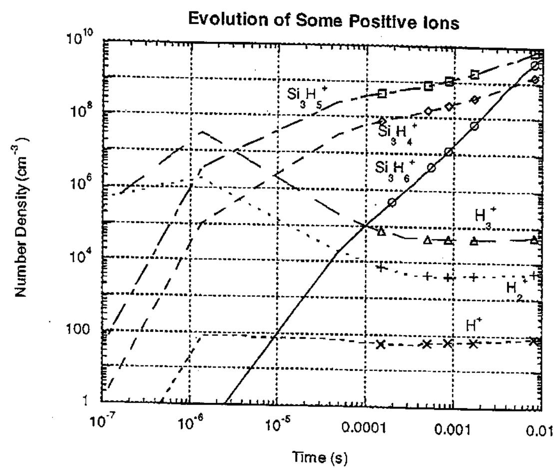

Fig. IV-35. Evolution of Positive Ions (cm^{-3}): c. $Si_3H_6^+$, $Si_3H_5^+$, Si_3H_4, H_3^+, H_2^+, H^+.

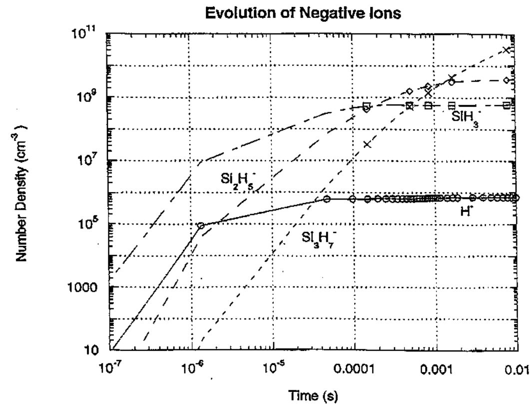

Fig. IV-36. Evolution of Negative Ions (cm^{-3}): H^{+}, SiH_3^{+}, $Si_2H_5^{+}$, $Si_3H_7^{+}$.

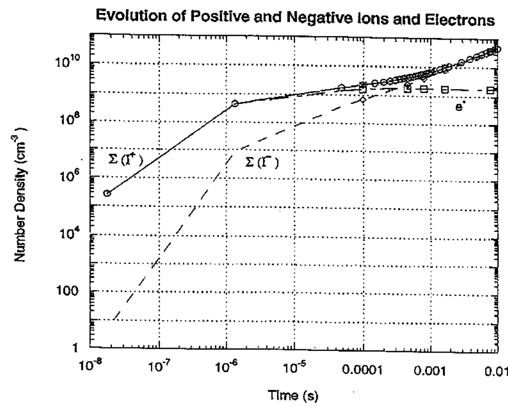

Fig. IV-37. Evolution of Positive and Negative Ions and Electrons (cm^{-3}): total positive ions, total negative ions, electrons.

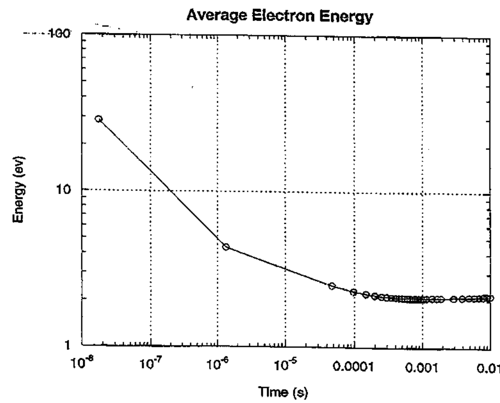

Fig. IV-38. Evolution of Average Electron Energy (ev).

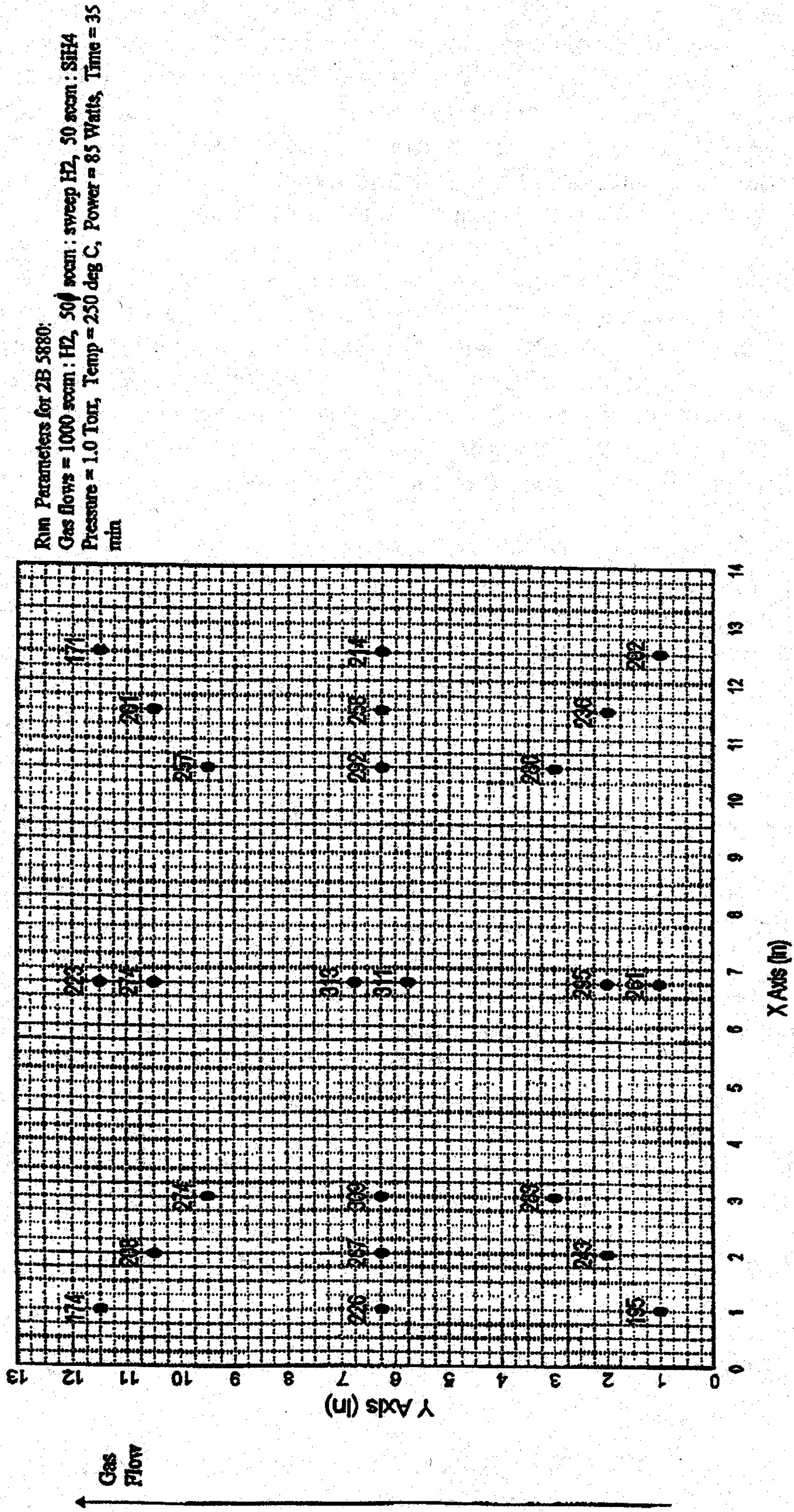

Fig IV-39. Measured Thickness of Amorphous Silicon Deposition (nm) in Reactor.

C. *Electron Density and Energy* – Figure IV-37 shows the evolution of the positive and negative ions and the electrons. Initially the electron density and positive ion density are equal to one another. As early as a few microseconds the electron density has come close to its equilibrium value ~ 10^9 cm^{-3}. The positive ions continue to increase and charge is conserved by the increase in the negative ions. Figure IV-38 shows a plot of the variation in the average electron energy with time. It reaches its equilibrium value, ~ 2 ev, by a few tenths of a millisecond.

D. *Amorphous Silicon Deposition* – The bottom line of the above simulation is comparison with measured data for the thickness of the deposition of amorphous silicon. To calculate this we need to know the density of amorphous silicon. According to the Handbook of Chemistry and Physics the value is 2.35 g/cm^3. Since silicon has an atomic weight of 28, the number of $moles/cm^3$ of amorphous silicon is 2.35/28 = 0.084 and the number of $molecules/cm^3$ is N_m = $0.084 \times 6.02 \times 10^{23}$ = 5.05×10^{22}, where we have used Avogadro's Number (=6.02×10^{23}).

To calculate the number of molecules of amorphous silicon on the substrate we need to know the flux of SiH_3 reaching the surface and we need to multiply that by the sticking coefficient. The measured sticking coefficient for SiH_3 in the published research data is 0.28. Because we are limited to a one-point calculation, we will assume that all of the gas originates from one point in the center of the reactor and that it diffuses from there to the substrate. To get the flux we need to calculate the diffusion velocity of SiH_3 through H_2. This is given by $V_d(SiH_3)$:

$$V_d(SiH_3) = (\nabla[SiH_3]/[SiH_3]) \times D(SiH_3,H_2) \times (\text{total gas density}/(15.5[SiH_3] + [H_2]))$$

In the first factor in the above expression, the gradient of SiH_3 between the center of the reactor and the substrate is calculated based on the assumption that, since at the substrate 28% of the molecules stick, there is just 72% of the SiH_3 density there as there is at the center. This gives for the first factor in the above expression, $0.28/\Delta x$, where Δx is the distance between the center of the reactor and the substrate (1.9 cm). The second factor, D, is the diffusion coefficient for SiH_3 diffusing through H_2. This is given approximately by $0.09(T_g)^{3/2}/p$, where T_g is the gas temperature in degrees Kelvin and p is the pressure in Torr. We take the gas temperature to be 523 K and the pressure to be 1 Torr. The last factor accounts for the need for overall mass balance in the diffusion process. From the simulation results we take the total gas density to be 1.8×10^{16} cm^{-3}, the density of SiH_3 as 1.9×10^{13} cm^{-3}, and the hydrogen density as 1.7×10^{16} cm^{-3}. When all the numbers are put in we find the diffusion velocity for SiH_3 to be 165 cm/s.

The number of molecules, N, sticking to the surface per square centimeter per second then is:

$$N = 0.28 \times V_d(SiH_3) \times [SiH_3] = 8.8 \times 10^{14} \text{ molecules/cm}^2/\text{s}$$

The thickness of the deposition of amorphous silicon, δ, is then:

$$\delta = N \times \Delta t / N_m = 8.8\times10^{14} \times 2.1\times10^{3} / 5.05\times10^{22} = 3.7\times10^{-5} \text{ cm}$$

The factor Δt is the run time, which was 35 minutes or 2.1×10^{3} s. The measured thickness of the deposition at the center of the substrate is 3.1 nanometers = 3.1×10^{-5} cm (see Figure IV-39). The discrepancy between measured value and simulation is 19%. Keeping in mind the crudeness of the simulation, based on a one-point model in which the SiH_3 is assumed to originate at one location at the center of the reactor and the neglect of ion effects, the agreement is remarkably good.

V. PINCH VALVE DEVELOPMENT

Summary

In this program we proposed designing, fabricating and testing a new “pinch valve” technology that would allow the production crews the ability to change rolls of substrate in the take-up and pay-off chambers without need to cool down, vent, pump down, and re-heat all the process chambers. We estimated that the turnaround time for the a-Si production machine could be reduced by about 6%. Since the a-Si machine is the rate-limiting machine, the resulting increase in throughput for this machine would directly lead to a corresponding throughput increase for the entire production plant.

This portion of the PVMat Program has been extremely successful – the milestone for testing this device in United Solar’s 5 MW production machine, scheduled for early in the Phase III portion of the program, was achieved at the end of Phase II. In the Phase III portion of the program we continued testing the pinch valves – a number of improvements were identified and carried out; this involved removing and re-installing the pinch valves a number of times. After the pinch valve mechanism was optimized, the United Solar production team began a program of making changes to the interlock, pumping, and sequence of operations necessary to implement this device into machine operations.

The pinch valves were put into standard operations in May 2001. During the period May – July, its use was gradually phased in: the pinch valves were used in about ¼ of the turn-arounds in July; in the first half of August, the pinch valves were used for every turn around. The United Solar production team has also spend time and effort modifying and qualifying further changes in the operational procedures to further decrease the turn around time to best leverage the advantages of the pinch valves. While we predicted a 6% increase in production throughput, our post-diction data now show that the production throughput may have been increased by as much as 10%.

We also expect additional less quantifiable benefits resulting from the pinch valves:

- The reduced thermal cycling of components should lead to more reliable operation and fewer component failures;
- The reduced exposure of the deposition portion of the machine to atmosphere should reduce contamination.

These devices were also used as models to develop new pinch valves for the new United Solar 25 MW production equipment being fabricated by ECD, and scheduled to begin operation in early 2001.

Overview

We developed and installed a sealing mechanism in the pay-off and take-up chambers of United Solars roll-to-roll a-Si vacuum deposition production machine that makes a reliable vacuum seal around the 5 mil (127 μm) thick stainless steel substrate. This pinch valve allows production coil changes to be made while the process chambers remained under vacuum. We estimated that as much as two hours might be saved at turn around between production runs with the use of this device; in addition, the process

chambers would not be exposed to atmosphere resulting in lower contamination levels. By allowing the deposition chamber to remain under vacuum during the coil change intervals, the system could then be held at or near the processing temperatures in an inert gas atmosphere, consequently eliminating the need for a cool down and heat up cycle. Also the procedure for removing reaction by-products, (blast backs) during the coil change interval could be carried out concurrently.

The first step in the development process required the fabrication of a prototype design with half the valve slot width of the final design. The prototype was then held in a bench vice, with a helium mass spectrometer attached for leak checking the device. A sample of the 5 mil production substrate was placed in the sealing slot and the pinch valve was actuated for several hundred cycles. The results demonstrated that the prototype was able to make a reliable vacuum seal around the substrate, with helium leak through rates between 2×10^{-10} and 2×10^{-8} sccm. This was convincing proof of the design concept, so scale up design work was carried out.

Once the final design and fabrication of the pinch valves were completed, the same bench testing procedures were carried out on these devices as described above. The valves preformed as well as the prototype and they where then installed in the pay-off and take-up chambers in the summer of 2000. The pinch valves where tested in the production system by venting only the pay-off and the take-up chambers and checking the valve leak through with the helium mass spectrometer. The result was the pinch valve on the pay-out chamber sealed around the substrate with no detectable leak; a leak in the 10^{-8} sccm range was detected at the take-up side valve – a level two orders of magnitude below the tolerable level. Consequently, both valves preformed to specification.

A description of the valve design and its principles of operation follows. The seal design incorporates the use of a special gasket material that is affixed to sealing surfaces (one static [above], and one dynamic [below]). The dynamic surface is actuated by a cam mechanism and is suspended from this mechanism with die springs that can be adjusted to increase or decrease the seal face pressure as required to make a reliable seal. The static seal surface incorporates a special seal that the web passes through; the seal allows for a vacuum seal to be made all way around the slot.

The pinch valve uses material and methods of construction acceptable to ultra-high purity vacuum practice. All the moving parts utilize needle bearings with a very high load bearing capability. We expect that the device should have a projected life in excess of the processor itself.

Commissioning the Pinch Valves

Pinch valves are installed on the 5 MW a-Si deposition machine in the summer of 2000, and some limited testing was carried out. In the fall of 2000, we have also purchased and installed additional pressure monitors to accommodate safety interlock systems when the pinch valves are used. New quality procedures were written for pinch valve operation and were approved for use depending upon the conclusion of successful testing.

The United Solar production team then wrote, testing and debugged the software modifications to the 5 MW control system to use the pinch valves in operation. This work was completed by the end of the year and we expected to have the pinch valves in routine operation by the spring of 2001.

In February 2001, final tests to put the new pinch valve system into operation were carried out. Two problems were observed:

1. A mechanical failure led to the valve not releasing the web when actuated, and consequently causing a web "crash" in the production equipment.
2. We also detected small vacuum leaks from the web pinch valve.

The pinch valves were subsequently removed and examined. Upon removing the pinch valves, we found a pinched O-Ring; the vacuum problems were a result of this pinched O-Ring, rather than a fundamental problem with the web pinch valve design. The design for the 25 MW pinch valves were redesigned to eliminate the possibility of the mechanical failure, and the 5 MW system was also redesigned and re-worked. The re-design work included the following:

- Magnetic rollers were attached to the valves to prevent the web from making contact with the bottom seal gaskets. This contact can cause damage to the gaskets and the deposited films.
- Die springs were added to assist in opening the valves, this was done to prevent sticking at the valve seats when opening them.
- The carriage for the moving (bottom) seal element, was reinforced with welded gussets to control unwanted deflection.
- There is a locking detent on the valve actuating cam. The depth of this detent, made the opening and closing of the valve more difficult than necessary, so the depth dimension was reduced.

In March 2001, the pinch valve had been successfully re-worked to solve the "sticking" problem.

In April 2001 the pinch valves were re-installed in the 5 MW production equipment and successfully tested.

In May 2001, the pinch valves were put into routine operation on the production a-Si machine. The operations group shortly set new records for the "turn-around" times using the pinch valve.

In the period June - July 2001 the United Solar production team worked on optimizing the operations procedures to take advantage of this new technology. For instance, whereas certain tasks were previously performed in series without impacting the turn-around time, they now must be performed in parallel to take full advantage of the pinch-valves. The production and QA/QC teams also studied and determined that another operation, a 50 minute "pre-burn", could be eliminated during a pinch valve turn-around.

Conclusion

The impact of the new pinch valve technology developed in this program is even greater than anticipated and can be clearly seen in the operations data. Its use has been phased in over the last two months. Although the data from operations is still sketchy, and the new operations procedures are still being optimized, the data indicate that the turn-around time has been reduced by about 2 hours, corresponding to about an 8% throughput increase for the a-Si machine, the rate limiting machine, as shown in Fig. V-1.

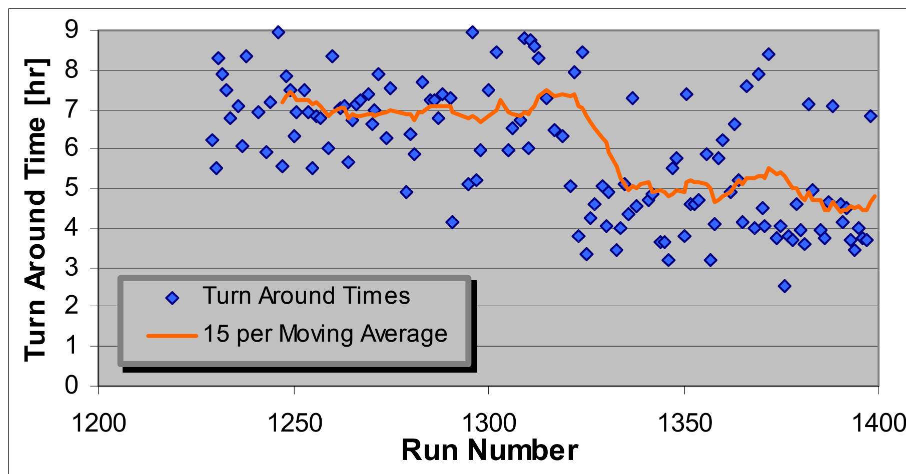

Fig. V-1. Amorphous silicon machine turn around time. The Pinch Valves were put into routine operation at about Run 1315.

The new pinch-valve technology is now a fully qualified part of standard operations, and has completed its transition from an operations headache to a success having a positive impact on manufacturing.

As mentioned previously, we also expect other, more difficult to quantify, benefits:

- The pinch valves will reduce the amount of thermal cycling in components. This may lead to lower component failure rates;
- The machine is not exposed to atmosphere at turn-arounds; this may reduce contamination and increase the average PV conversion efficiency.

The pinch gate valves have been through a rigorous testing in the 5MW a-Si machine. These valves are now used during all of the coil change operations, and are demonstrating reliability in a production environment. With the confidence gained by this testing, United Solar has commissioned ECD to install a second generation of these devices in the 25MW a-Si machine.

REPORT DOCUMENTATION PAGE	Form Approved OMB NO. 0704-0188

Public reporting burden for this collection of information is estimated to average 1 hour per response, including the time for reviewing instructions, searching existing data sources, gathering and maintaining the data needed, and completing and reviewing the collection of information. Send comments regarding this burden estimate or any other aspect of this collection of information, including suggestions for reducing this burden, to Washington Headquarters Services, Directorate for Information Operations and Reports, 1215 Jefferson Davis Highway, Suite 1204, Arlington, VA 22202-4302, and to the Office of Management and Budget, Paperwork Reduction Project (0704-0188), Washington, DC 20503.

1. AGENCY USE ONLY (Leave blank)	2. REPORT DATE April 2002	3. REPORT TYPE AND DATES COVERED Final Subcontract Report 28 June 1998 – 5 October 2001

4. TITLE AND SUBTITLE Efficiency and Throughput Advances in Continuous Roll-to-Roll a-Si Alloy PV Manufacturing Technology, Final Subcontract Report, 28 June 1998 – 5 October 2001 6. AUTHOR(S) Tim Ellison	5. FUNDING NUMBERS CF: ZAX-8-17647-09 PVP26101
7. PERFORMING ORGANIZATION NAME(S) AND ADDRESS(ES) Energy Conversion Devices, Inc. 1675 W. Maple Rd. Troy, Michigan 48084	8. PERFORMING ORGANIZATION REPORT NUMBER
9. SPONSORING/MONITORING AGENCY NAME(S) AND ADDRESS(ES) National Renewable Energy Laboratory 1617 Cole Blvd. Golden, CO 80401-3393	10.SPONSORING/MONITORING AGENCY REPORT NUMBER NREL/SR-520-31723

11.SUPPLEMENTARY NOTES

NREL Technical Monitor: Rick Mitchell

12a. DISTRIBUTION/AVAILABILITY STATEMENT National Technical Information Service U.S. Department of Commerce 5285 Port Royal Road Springfield, VA 22161	12b. DISTRIBUTION CODE

13.ABSTRACT *(Maximum 200 words)* This report describes a roll-to-roll triple-junction amorphous silicon alloy PV manufacturing technology developed and commercialized by Energy Conversion Devices (ECD) and United Solar Systems. This low material cost, roll-to-roll production technology has the economies of scale needed to meet the cost goals necessary for widespread use of PV. ECD has developed and built six generations of a-Si production equipment, including the present 5 MW United Solar manufacturing plant in Troy, Michigan. ECD is now designing and building a new 25-MW facility, also in Michigan. United Solar holds the world's record for amorphous silicon PV conversion efficiency, and manufactures and markets a wide range of PV products, including flexible portable modules, power modules, and innovative building-integrated PV (BIPV) shingle and metal-roofing modules that take advantage of this lightweight, rugged, and flexible PV technology. All of United Solar's power and BIPV products are approved by Underwriters Laboratories and carry a 10-year warranty. In this PVMaT 5A subcontract, ECD and United Solar are addressing issues to reduce the cost and improve the manufacturing technology for the ECD/United Solar PV module manufacturing process. ECD and United Solar identified five technology development areas that would reduce the module manufacturing cost in the present 5-MW production facility, and also be applicable to future larger-scale manufacturing facilities.

14.SUBJECT TERMS: PV; substrate heating; temperature monitoring systems; in-line sensors; ZnO reactive sputtering; pinch valve; backreflector scatterometer; amorphous silicon deposition; PV capacitive diagnostic	15.NUMBER OF PAGES 16.PRICE CODE

17.SECURITY CLASSIFICATION OF REPORT Unclassified	18.SECURITY CLASSIFICATION OF THIS PAGE Unclassified	19.SECURITY CLASSIFICATION OF ABSTRACT Unclassified	20.LIMITATION OF ABSTRACT UL

NSN 7540-01-280-5500

Standard Form 298 (Rev. 2-89)
Prescribed by ANSI Std. Z39-18
298-102